ТЕХНІКА ТА ЕНЕРГЕТИКА

Засновник:
Національний університет біоресурсів і природокористування України

Рік заснування: 2010

Рекомендовано до друку та поширення
через мережу Інтернет Вченою радою
Національного університету біоресурсів і природокористування України
(протокол № 10 від 26 квітня 2023 р.)

Свідоцтво про державну реєстрацію
друкованого засобу масової інформації
серії КВ № 25126-15066 ПР від 17 лютого 2022

Журнал входить до переліку наукових фахових видань України
Категорія «Б». Галузь наук – Технічні.
Спеціальність: 131 – «Прикладна механіка», 133 – «Галузеве машинобудування»,
141 – «Електроенергетика, електротехніка та електромеханіка»,
151 – «Автоматизація та комп'ютерно-інтегровані технології»
(Наказ Міністерства освіти і науки України від від 17 березня 2020 року № 409)

Журнал представлено у міжнародних наукометричних базах даних, репозитаріях та пошукових системах: Index Copernicus International,
Google Scholar, Фахові видання України,
Національна бібліотека України імені В. І. Вернадського,
BASE, Academic Resource Index ResearchBib

Адреса редакції:
Національний університет біоресурсів і природокористування України
03041, вул. Героїв Оборони, 15, м. Київ, Україна
E-mail: info@technicalscience.com.ua
www: https://technicalscience.com.ua/uk

MACHINERY & ENERGETICS

Founders:
National University of Life and Environmental Sciences of Ukraine

Year of foundation: 2010

Recommended for printing and distribution
via the Internet by the Academic Council
of National University of Life and Environmental Sciences of Ukraine
(Minutes 10 of April 26, 2023)

Certificate of state registration
of the print media
Series KV No. 25126-15066 PR of February 17, 2022

The journal is included in the list of Professional Scientific Publications of Ukraine
Category "B". Branch of sciences – Technical.
Specialty: 131 – "Applied Mechanics", 133 – "Branch Mechanical Engineering",
141 – "Electric Power Industry, Electrical Engineering and Electromechanics",
151 – "Automation and Computer-Integrated Technologies"
(Order of the Ministry of Education and Science of Ukraine of March 17, 2020, No. 409)

The journal is presented international scientometric databases, repositories and scientific systems: Index Copernicus International,
Google Scholar, Professional publications of Ukraine,
Vernadsky National Library of Ukraine, BASE,
Academic Resource Index ResearchBib

Editors office address:
National University of Life and Environmental Sciences of Ukraine
03041, 15 Heroiv Oborony, Kyiv, Ukraine
E-mail: info@technicalscience.com.ua
www: https://technicalscience.com.ua/en

Редакційна колегія

Міжнародні члени редколегії:

Editorial Board

International Members of the Editorial Board:

ЗМІСТ

CONTENTS

Machinery & Energetics
Vol. 14, No. 2. 2023

Journal homepage:
https://technicalscience.com.ua/en

UDC 621.313.33:621.318.122
DOI: 10.31548/machinery/2.2023.09

Krzysztof Mudryk
Professor
University of Agriculture in Krakow
30-149, 21 Adam Mitskevich Ave., Krakow, Poland
https://orcid.org/0000-0002-6212-6958

Taras Hutsol
Professor
University of Agriculture in Krakow
30-149, 21 Adam Mitskevich Ave., Krakow, Poland
https://orcid.org/0000-0002-9086-3672

Nikolay Zablodskiy*
Doctor of Technical Sciences, Professor
National University of Life and Environmental Sciences of Ukraine
03041, 15 Heroiv Oborony, Kyiv, Ukraine
https://orcid.org/0000-0001-8889-8158

Dmytro Sorokin
PhD in Technical Sciences, Associate Professor
National University of Life and Environmental Sciences of Ukraine
03041, 15 Heroiv Oborony, Kyiv, Ukraine
https://orcid.org/0000-0002-1762-9724

Serhii Usenko
PhD in Technical Sciences, Associate Professor
National University of Life and Environmental Sciences of Ukraine
03041, 15 Heroiv Oborony, Kyiv, Ukraine
https://orcid.org/0000-0001-7225-9589

A study of electrothermomechanical converter for technological purposes with nonlinear changes in the loading and cooling medium

Abstract. Heavy temperature processes with high-temperature loads require optimisation of technological processes, ensuring high reliability and combining rotating parts of electric machines with actuators to achieve greater efficiency of electromechanical converters. The research aims to provide a theoretical justification and experimental confirmation of the effect of higher harmonics in the air gap under nonlinear changes in the temperature of the medium. The research is based on the basic principles of electrodynamics, heat and mass transfer, mathematical modelling by the finite element method, and experimental verification of multi-physical parameters. Based on the analysis of the differential equation for determining the increase in the surface temperature of a ferromagnetic rotor under conditions of nonlinear temperature changes in the environment surrounding the electromechanical converter, the regularities of the formation of the free and forced components of the instantaneous temperature values of the massive rotor are established. Depending

Article's History: Received: 18/01/2023; Revised: 22/03/2023; Accepted: 26/04/2023.

Suggested Citation:
Mudryk, K., Hutsol, T., Zablodskiy, N., Sorokin, D., & Usenko, S. (2023). A study of electrothermomechanical converter for technological purposes with nonlinear changes in the loading and cooling medium. *Machinery & Energetics,* 14(2), 9-22. doi: 10.31548/machinery/2.2023.09.

*Corresponding author

on the mode of interaction between the load-cooling medium and the electromechanical part of the screw units, kinematic diagrams of single-mass and two-mass systems with variable or constant moments of inertia and stiffness were formed. According to the size of the electromagnetic system of the experimental sample, a mathematical model for studying thermal and electromagnetic processes was built. The regularities of the spatial distribution of the temperature of the screw electromechanical unit are determined. The spectra of higher harmonics of voltage and current in the frequency range from 0 to 50 kHz have been experimentally determined, which confirms the presence of the effect of generating higher harmonics when the temperature of the medium surrounding the rotor screw changes. The detected harmonic spectrum affects both the formation of the dynamics of the rotating system and additional thermal power while increasing the overall efficiency of the screw electromechanical converter. The practical value of the obtained results lies in the possibility of predicting the optimal indicators of interrelated electromagnetic and heat exchange processes in screw electromechanical converters for technological purposes

Keywords: higher harmonics spectrum; ferromagnetic hollow rotor; biomass; temperature field; electromagnetic field; design; and technological scheme

INTRODUCTION

Applications of electromechanical transducers exist for which, in addition to the concept of efficiency, reliable operation in a process environment with high temperature, pressure and humidity or a limited volume is also a significant parameter. To predict losses, A. Laidoudi *et al.* (2020) proposed an analytical model that is combined with a thermal model to predict the temperature in different parts of the machine, its impact on the parameters that are important for the performance of an electric machine (EM) at high temperatures.

The issue of finding alternative solutions to replace organic insulating materials that cannot withstand hot operating conditions is relevant. In the studies of M. Lefik *et al.* (2019), H. Elmadah *et al.* (2019), E.N. Juszczak *et al.* (2020) performed a comparative analysis of the laminated and solid rotor of a synchronous machine operating at high temperatures using windings made of inorganic materials. The study also presents the application of three-dimensional combined electromagnetic and thermal analysis of new machine designs designed for elevated temperatures.

A wide range of technological processes with heavy temperature loads exists that requires the direct connection of rotating EM parts with actuators. M.M. Mazlan *et al.* (2019), and F. Campuzano *et al.* (2019) proved the effectiveness of using a screw converter, which is attractive due to its versatility in processing various types of materials, regardless of the pace of the technological process. The influence of hydrolysis parameters on the mixing torque was investigated for single- and twin-screw electromechanical converters by P. Singha & K. Muthukumarappan (2016) and C. Feng *et al.* (2019). In these studies, regression models were developed to establish the correlation between system parameters and time-varying parameters. The results showed that increasing the processing temperature beyond the recommended levels led to a decrease in the viscosity of the raw material, the pressure in the processing medium, and the specific mechanical energy. In addition, M. Mushtruk *et al.* (2020) investigated the issue of high energy consumption associated with machining in an electromechanical screw converter. In the study, mathematical modelling was carried out and the power and energy parameters of the technical system were determined.

V. Gritsyuk *et al.* (2022) noted that 3D printing technologies for large-scale structures allow architects and builders to significantly expand the boundaries of building design and increase the efficiency of their construction. Mobile robotic platforms for 3D printing are increasingly being introduced in the construction industry, as well as in the production of road surfaces, which helps to solve the problem of limited working space. The typical design of the extruder unit of a robotic platform for 3D printing large-scale structures can be improved by combining an electric motor, a screw extruder, and a heater in one housing. The proposed screw electro-thermomechanical converter uses an external screw rotor that simultaneously performs the functions of an induction motor rotor, heating element, actuator, and protective casing. For converters operating under harsh conditions, the use of field calculation methods is relevant.

As such, along with solving the problem of ensuring the reliability of electromechanical converters in harsh environments, a scientific demand for improving the energy efficiency of their use through structural, functional, and thermal integration with the technological environment is present.

The research aims to theoretically substantiate and experimentally confirm the effect of the appearance of higher harmonics in the air gap under nonlinear changes in the temperature of the medium surrounding the electromechanical converter in screw technological systems.

MATERIALS AND METHODS

The research was carried out at the Department of Electrical Engineering, Electromechanics and Electrical Technologies of the National University of Life and Environmental Sciences of Ukraine in 2020-2022. The study considered two modifications of an electromechanical converter for technological purposes, in which the processed raw material acts as a loading and cooling medium: in a twin-screw electromechanical hydrolyser; use of an electric screw unit for grinding and pyrolysis of plant waste biomass. In this

case, the actuator (auger) is combined with the outer rotor of the electromechanical converter. The electromechanical converter was presented as a six-pole (Fig. 1) with an electrical circuit characterised by voltage U and frequency f, a mechanical circuit defined by torque M and mechanical rotational speed n, and a thermal circuit characterised by heat quantity Q and temperature T.

The design and technological scheme of a twin-screw electromechanical hydrolyser for the production of feed protein meal is shown in Figure 2.

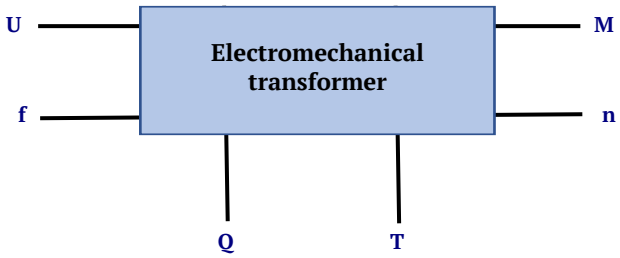

Figure 1. Hexagon-pole electromechanical converter
Source: compiled by the authors

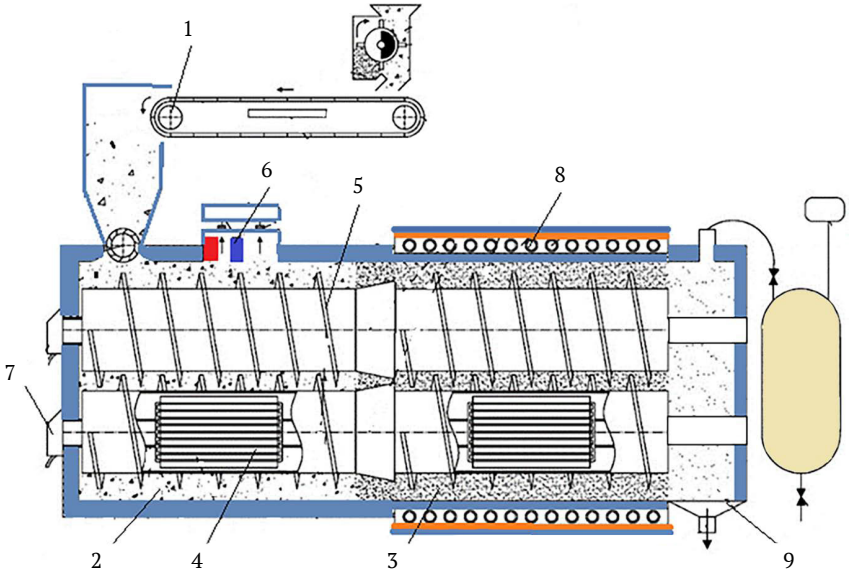

Figure 2. Design and technological scheme of a twin-screw electromechanical hydrolyser
Note: 1 – loading device with magnetic and electrodynamic separators; 2, 3 – sealing and reaction working zones; 4 – cylindrical inductors of a rotating magnetic field; 5 – rotor screw; 6 – magnetic deaeration chamber for raw materials; 7 – power supply cable connection boxes; 8 – induction heating device with thermal insulation and electromagnetic shield; 9 – vacuum-pulse product unloading device
Source: compiled by the authors based on (Patent of Ukraine No. 125774, 2022)

The feather and fluff raw material with an initial moisture content of 60-80 % was supplied to the feeding device of the screw unit, where it was exposed to electromagnetic fields to remove metal particles and the water-air component was removed from the raw material to the level of residual moisture (35-45 %) using a belt vacuum filter. In the first working area of the screws, a raw material seal (plugs) was created by reducing the flow section of the screw unit and providing a pressure of 1 MPa to 20 MPa. Along with the compaction, the feedstock was heated to a temperature of 60°C, exposed to a gradient magnetic field with a frequency of 1-50 Hz and an induction of 0.025T, and magnetic deaeration was performed. The raw material was then fed into the reaction working area of the screws, where it was loosened by the reduced diameter part of the screw turns, mixed and crushed at a temperature of 180-260°C to obtain a crushed mass. At the same time, a gradient magnetic field with a frequency of 1-50 Hz and an induction of 0.065 T was applied in this area of the installation and four-sided heat energy was supplied to the layer of down and feather raw materials. In the vacuum-pulse device, a vacuum effect was applied every 10-60 s to obtain a product with a moisture content of 8-12%. The design and technological scheme are shown in Figure 3.

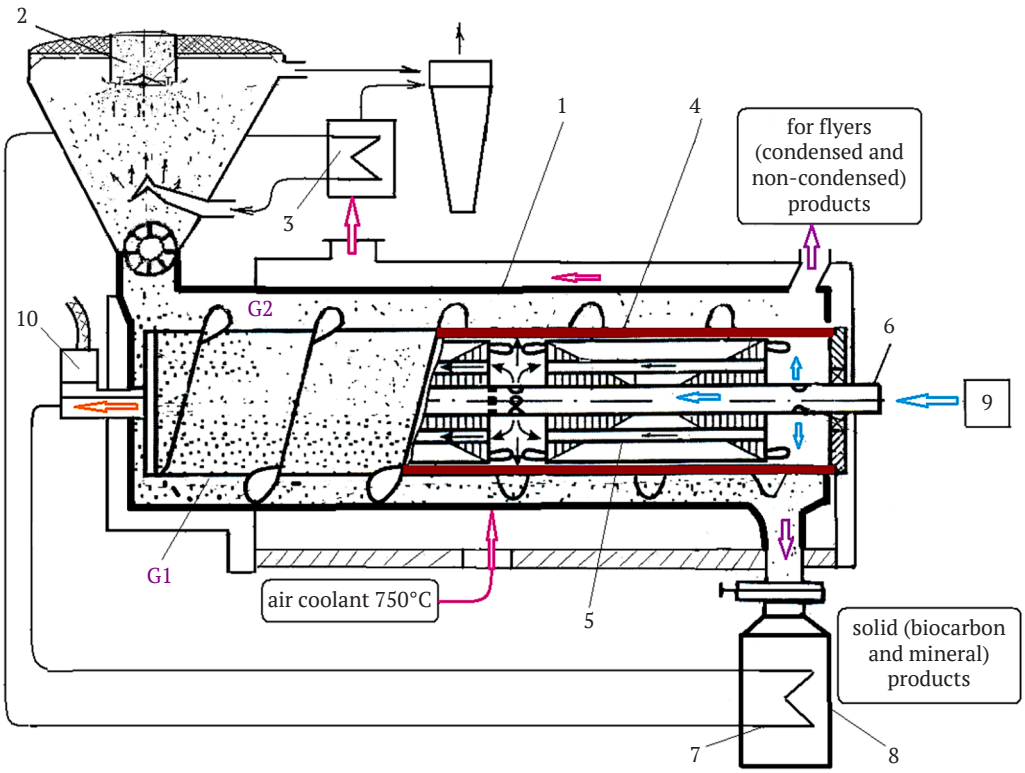

Figure 3. Design and technological scheme of the plant biomass pyrolysis unit
Note: 1 – pyrolysis chamber; 2 – hopper with loading devices; 3 – heat recovery system; 4 – rotor screw; 5 – cylindrical inductors of a rotating magnetic field; 6 – fixed hollow shaft; 7 – heat exchanger; 8 – solid product unloading chamber; 9 – air supply system; 10 – power supply cable connection box
Source: compiled by the authors based on (Zablodskiy *et al.*, 2020)

The process gas with an excess air ratio of less than one was burned in the process furnace to produce a high-temperature (750°C) gas coolant, which was supplied for external heating of the pyrolysis chamber1. The finely fractionated biomass was supplied in portions through a lid with a magnetic closure to the hopper of loading device 2, where it was pre-dried and heated (Zablodskiy *et al.*, 2020). Using the feeder, the biomass was fed into the screw-type sealed pyrolysis chamber 1, where the biomass layer was heated on the one hand through the chamber walls by the coolant generated during the combustion of fuel in the process furnace, and on the other hand by conductive heat transfer and radiation from the surface of the outer massive rotor 4 of the electromechanical converter connected to a three-phase power supply network.

In both modifications under consideration, the mechanical energy of rotation of the rotor-auger was created by the interaction of a rotating magnetic field and eddy currents in the ferromagnetic array of the rotor-auger. The working load-cooling medium was in direct contact with the rotor-auger. Depending on the loading mode, the kinematic diagram of the mechanical part of the screw units can be presented in the following forms:

- single-mass system at idle (Fig. 4a);
- two-mass system operating with variable stiffness C_{12} and variable moment of inertia J_2 of the viscous mass in the mode of gradual filling of the screw (Fig. 4b);
- two-mass system with constants C_{12} and J_2 in the basic mode of operation (Fig. 4c);
- two-mass system with constants C_{12} and J_2 in the screw release mode (Fig. 4d);

The stiffness coefficient C_{12} contains two components related to the ratio of elastic bond load and rotational and translational deformation.

During rotation, the areas of the outer surface of the screw rotor periodically fall into different temperature zones above and below the shaft axis (Fig. 3). A similar picture is observed in the working areas of a twin-screw electromechanical hydrolyser (Fig. 2) in the layers of raw materials located between the screw rotors and the walls of the sealing and reaction working areas, as well as between the screw surfaces. Since the rotor rotation frequency is almost constant at a certain screw capacity, it is possible to observe the process of periodic changes in the temperature of the medium washing the outer surface of the ferromagnetic rotor.

In the first approximation, it was assumed that the temperature increase of the medium ΔT_{en} varied periodically (sinusoidally) in time. The differential equation for determining the temperature increase of the surface of a ferromagnetic rotor will be as follows:

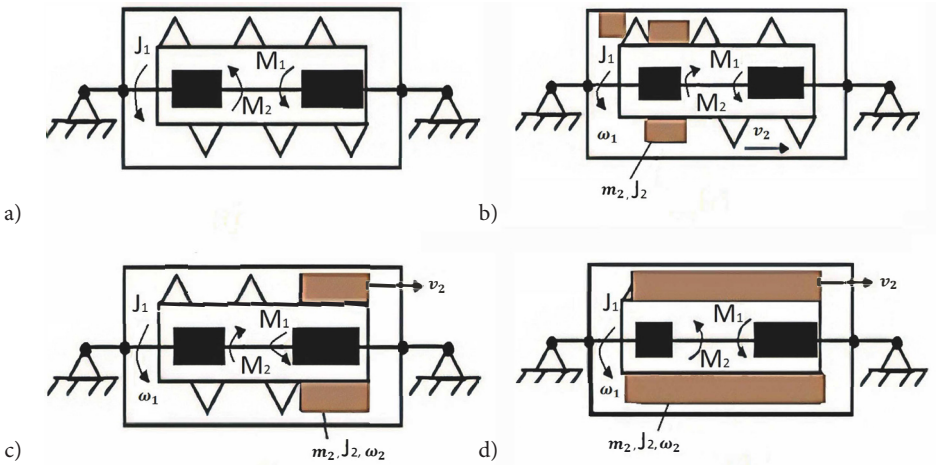

Figure 4. Kinematic diagrams of screw units

Note: J_1 – a moment of rotor screw inertia; J_2 – a moment of viscous mass inertia; M_1, M_2 – rotation under motion and braking modules; υ_2 – viscous mass velocity; m_2 – the weight of the substance loaded into the screw; ω_1 ,ω_2 – angular velocity of the rotor screw and viscous mass, respectively

Source: compiled by the authors

$$R_r \frac{d(\Delta T_r)}{dt} + \Delta T_r = \Delta T_{en.m}\, sin(\omega_r t), \quad (1)$$

where R_r – thermal time constant of the rotor design zone; $\Delta T_{en.m}$ – environment temperature amplitude increase; ΔT_r– rotor temperature increase; ω_r – cyclic frequency of change in the temperature of the medium, equal to the angular frequency of rotation of the rotor.

Thermal time of ferromagnetic rotor:

$$R_r = \frac{m_r c_r}{2 \cdot G_{TCR}}, \quad (2)$$

where , m_r, c_r – respectively mass and specific heat capacity of the rotor material; G_{TCR} – rotor heat conductivity.

Heat conductivity G_{TCR} is calculated for a homogeneous cylindrical wall with heat sources and heat dissipation through the outer wall (Subramanian, 2014):

$$G_{TCR} = \frac{4\pi\lambda \cdot l_r}{\frac{2r_2^2}{r_2^2 - r_1^2} \ell n \frac{r_2}{r_1}}, \quad (3)$$

where l_r – rotor length; r_1, r_2 – inner and outer radii of the cylindrical rotor, respectively; λ – rotor material heat conductivity coefficient.

Formula (3) is valid provided that the depth of penetration of the electromagnetic wave into the rotor Δ_{ew} in the operating sliding mode is approximately equal to the rotor wall thickness $(r_2 - r_1)$.

When $(r_2 - r_1) > \Delta_{ew}$ an exponential heat release function must be included in the calculations $q_{uo} te^{-\beta X/(r_2 - r_1)}$, where q_{vo} – specific heat emission in a thin layer at $x_o \approx R_1$; β – coefficient of uneven loss distribution.

A more accurate result for calculating thermal conductivity G_{TCR} can be obtained by considering the helical blades (fins) of the rotor, which significantly intensify heat transfer between the rotor's inner surface and the environment. In this case, the following calculation formula can be used:

$$G_{TCR} = \frac{2\pi \cdot r_2 \cdot l_r}{\frac{1}{\alpha_1} + \frac{r_2 - r_1}{\lambda} + \frac{1}{\alpha_2[1 + A_{os}(k_{os} - 1)]}}, \quad (4)$$

where α_1 – the heat transfer coefficient on the un-finned surface of the rotor wall; α_2 – is the heat transfer coefficient from the finned rotor surface. The equality of heat transfer coefficients with smooth α_s surface and rib surface α_r; A_{os} – rib efficiency coefficient; k_{os} – the coefficient of finning of the rotor surface, equal to the ratio of the total area of the finned surface to the area of the smooth rotor surface.

Rib efficiency coefficients at height h_r and thickness δ_r, manufactured from material with heat conductivity λ_r:

$$A_{os} = \varepsilon_к \frac{thB}{B}, \quad (5)$$

where $B = h_r[2\alpha_r / \lambda_r \delta_r]^{0,5}$.

The value of the correction factor ε_k is a function of the ratio of the excess temperatures at the end and base of the fin and the ratio of the outer radii of the fin (blade) and the smooth rotor.

The solution to equation (1) is obtained as two components.

Forced component $\Delta T'_r$ can be given as:

$$\Delta T'_r = \Delta T_{en.m} e^{j\omega_r t}. \quad (6)$$

Using the symbolic method of operations with complex numbers, the differential equation (1) can be represented as:

$$R_r \cdot \frac{d(\Delta T_{rm} e^{j\omega_r t})}{dt} + \Delta T_{r.m} e^{j\omega_{rr} t} = \Delta T_{en.m} e^{j\omega_r t}, \quad (7)$$

where ΔT_{rm} – amplitude value of the rotor temperature increase.

Having found the derivative in (7), the amplitude value of the temperature increase of the massive rotor was determined.

$$\Delta T_{rm} = \frac{\Delta T_{en.m}}{1+j\omega_r R_r}. \quad (8)$$

Then, the phase angle φ_r between increases ΔT_r and ΔT_{en} was found:

$$\varphi_r = arctg(-\omega_r R_r), \quad (9)$$

where symbol "–" shows the increase ΔT_r lacking on the increase phase ΔT_{en}.

As a result, the stationary solution of the differential equation (1) concerning the forced component can be represented as follows:

$$\Delta T_r' = \frac{\Delta T_{en.m}}{\sqrt{1+\omega_r^2 R_r^2}} sin(\omega_r t - \varphi_r). \quad (10)$$

To find the free component of the right, the part of equation (1) was set to zero:

$$R_r \cdot \frac{d(\Delta T_r)}{dt} + \Delta T_r = 0. \quad (11)$$

An equation was made:

$$R_r \cdot Z + 1 = 0, \quad (12)$$

where $Z = \frac{d(\Delta T_r)}{dt}$.

Value $Z = -1/R_p$. Then the partial solution was represented as an exponent:

$$\Delta T_r'' = Ae^{-t/R_r}, \quad (13)$$

where A – coefficient, derived from initial conditions.

Thus, considering (10) and (13), the full solution of equation (1) is as follows:

$$\Delta T_r = \frac{\Delta T_{en.m}}{\sqrt{1+\omega_r^2 R_r^2}} sin(\omega_r t - \varphi_r) + Ae^{-t/R_r}. \quad (14)$$

Under initial circumstances, thus $t = 0$, ΔT_r, based on (14), an expression was obtained to determine the coefficient A:

$$A = \frac{\Delta T_{en.m}}{\sqrt{1+\omega_r^2 R_r^2}} sin\,\varphi_r. \quad (15)$$

Expression for immediate values ΔT_r temperature of the massive rotor at a sinusoidal change in the medium temperature in time ΔT_{en} can be presented as follows:

$$\Delta T_r = \frac{\Delta T_{en.m}}{\sqrt{1+\omega_r^2 R_r^2}} \left[sin(\omega_r t - \varphi_r) + e^{-t/R_r} \cdot sin\,\varphi_r\right]. \quad (16)$$

The harmonic composition of current and voltage was determined on an experimental model of an electric screw unit for grinding and pyrolysis of plant waste biomass. Figure 5 shows the electric auger's operating chamber, and Figure 6 shows the wiring diagram for the measuring instruments.

The following measuring instruments were used during the empirical research: Hantek 6254BC four-channel digital USB oscilloscope (manufactured in China); Tenmars TM-191 Magnetic Field Meter (manufactured in Taiwan), designed to measure ultra-low frequency electromagnetic fields from 30 Hz to 300 Hz; Tenmars TM-190 Multi-Field EMF Meter (Taiwan) – a device for measuring high-frequency electromagnetic fields in the frequency range from 50 MHz to 3.5 GHz and low-frequency electric and magnetic fields in the frequency range of 50-60 Hz; infrared, optical pyrometer BENETECH GM533A (China), measuring range – 50-530°C, visibility index 12: 1, thermal radiation coefficient 0.1-1, spectrum 5-14 microns.

Figure 5. Operation chamber of the electric auger unit for shredding and pyrolysis of plant waste biomass (upper part of the housing removed)

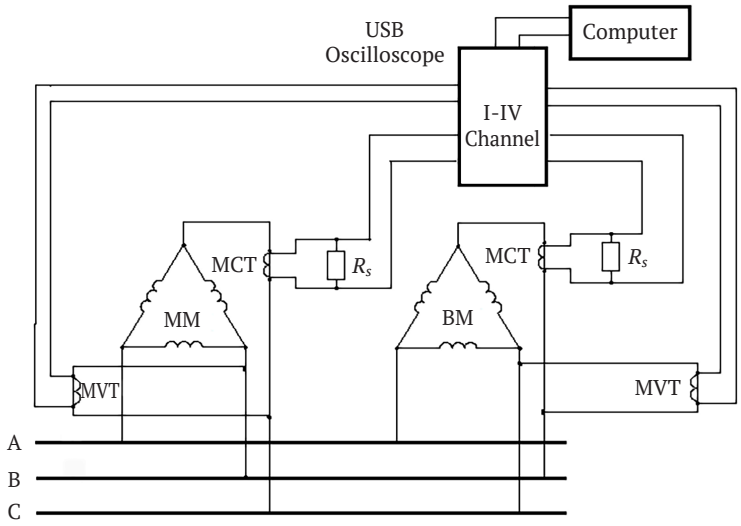

Figure 6. Wiring diagram for measuring devices
Note: MM, BM – stator windings of the motor and brake modules, respectively; MVT, MCT – voltage and current measuring transformers; R_s – shunt; A, B, C – electricity network phases
Source: compiled by the authors

To understand in detail the complete picture of the temperature and magnetic fields in the screw electromechanical hydrolyser and the unit for pyrolysis of biomass from plant waste, mathematical modelling (MM) was carried out using the finite element method in the Comsol Multiphysics software environment. The electromagnetic field was analysed based on Maxwell's system of equations. To determine the current density induced in the rotor, the following expression can be used, which follows from the first equation of Maxwell's system of equations:

$$J_z = rot_z H = \frac{1}{\mu}\left(\frac{\partial B_y}{\partial x} - \frac{\partial B_x}{\partial y}\right). \quad (17)$$

The differential equation of the thermal field in partial derivatives concerning temperature T is as follows:

$$\Delta T - c\rho\frac{\partial T}{\partial t} = -Q, \quad (18)$$

where λ, c, ρ – respectively thermal conductivity, heat capacity and density of the material; Q – specific heat loss.

At each point of the rotor, the specific losses are calculated using the following expression:

$$Q = J_z^2/\gamma(T), \quad (19)$$

where the electrical conductivity of the rotor iron at each point depends on the temperature T.

In Cartesian coordinates for a two-dimensional field picture, equation (18) is rewritten as follows:

$$\lambda\frac{\partial^2 T}{\partial x^2} + \lambda\frac{\partial^2 T}{\partial y^2} - c\rho\frac{\partial T}{\partial t} = Q. \quad (20)$$

The interrelation of the equations of the electromagnetic and thermal fields is manifested in the mutual influence of temperature, electrical conductivity, eddy current density, and specific heat losses, which is reflected in expressions (17-19). Boundary and initial conditions are set for equation (20). The choice of boundary conditions is determined by the peculiarities of the operating modes. The most favourable conditions for the process of generating higher harmonics were chosen for the study – the mode of gradual filling of the screw, and for comparison – the mode of a single-mass system at idle stroke. In this case, when constructing the MM, we assume that the main heat transfer from the rotor to its upper part is carried out by convective heat exchange between the heated surface and the airflow (area G_2, Fig. 3) Such heat transfer occurs following the Newton-Richman law, and a boundary condition of the third kind is set at the corresponding boundary:

$$\left.\frac{\partial T}{\partial n}\right|_{G_1,G_2} = -\frac{\alpha}{\lambda}(T - T_0), \quad (21)$$

where α – heat dissipation coefficient; T_0 – coolant air temp.

The boundary condition (21) is also set on the inner surface of the fixed hollow shaft and the surfaces of the axial ventilation channels made in the stator core. The heat transfer on the lower part of the rotor surface (area G_1, Fig. 3) in contact with the transported bulk material has a complex physical nature. From the physical point of view, the most adequate assumption is that the joule losses generated in the lower half of the rotor are transferred to the bulk material in the form of heat flow through the surface G_1. This assumption is met by a boundary condition of the second kind, which sets the average value of the heat flux at the boundary of the computational domain:

$$q|_{G_1'} = \frac{1}{R_{2н}}\int_{S'} Q\, ds = \frac{1}{R_{2н}}\int_{S'}[J_z^2/(\gamma)T]\, ds, \quad (22)$$

where $R_{2н}$ – external rotor radius; S' – integration region. Condition (22) also determines the relationship between the electromagnetic and thermal tasks.

RESULTS AND DISCUSSION

The graphical representation of dependencies (10), (13), and (16) is shown in Figure 7.

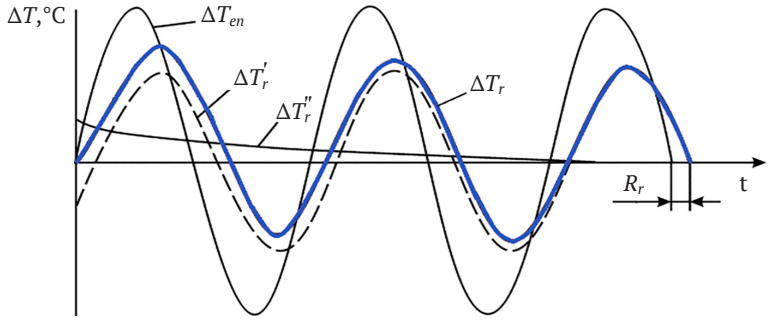

Figure 7. Changes in the rotor temperature of an electromechanical screw converter over time with sinusoidal fluctuations in the medium temperature

Note: R_r – thermal time constant of the rotor design zone; ΔT_r – rotor temp increase; $\Delta T'_r$ – forced rotor temperature increase component; $\Delta T''_r$ – free (aperiodic) component of the rotor temperature increase; ΔT_{en} – increase in ambient temperature

Source: compiled by the authors

As can be seen from the relation (16) and Figure 7, a transient process is observed in the initial time, followed by a sinusoidal change in the rotor temperature, which, in turn, causes pulsations in the specific active resistance ρ and magnetic permeability μ of the rotor material. The influence of temperature on the nature of electromagnetic processes is illustrated by the example of the penetration of an electromagnetic field wave into a massive conductive body. The law of penetration of the induced current deep into the rotor under a harmonically varying magnetic field in time can be approximately expressed by the following expression:

$$J(y) = J_m e^{-ky}, \tag{23}$$

where $k = \sqrt{\omega\mu/2\rho}$; ω – angular frequency of field change; μ – magnetic permeability; ρ – resistivity.

The inverse value $\Delta = 1/k$ is termed the conditional depth of alternating current penetration into the rotor and is equal to the distance from the conductor surface at which the current value decreases by a factor of e. The rotor resistivity is linearly dependent on temperature according to the known law:

$$\rho = \rho_0[1 + \alpha(T - T_0)], \tag{24}$$

where ρ_0 – resistivity at temperature T_0.

The dependence of the magnetic permeability of steel on temperature is more complex and is determined by empirical dependencies. In this study, the structural carbon steels were found to have the following values μ in the strong field range ($H = 2 \cdot 10^{-3}...12 \cdot 10^{-3}$ A/m) have slight fluctuations when heated to temperature 400°C, but then begin to decrease with increasing temperature, reaching unity at the Curie point temperature, which coincides with the data. All other conditions being equal, as the rotor temperature T increases, the depth of penetration of its currents also increases:

$$\Delta = \sqrt{2\rho_0[1 + \alpha(T - T_0)]/\omega\mu}. \tag{25}$$

There is a limited amount of data in the published literature on the effect of temperature and pressure on the magnetic properties of steel, for example, in the case of submersible motors used in oil wells or deep-sea oil-filled motors (Zou *et al.*, 2012; Zhang *et al.*, 2016). It is difficult to determine the magnetic properties of electrical steel sheets in an environment where temperature and pressure are coupled using known data and hysteresis models. Therefore, to improve the accuracy of EM design calculations, it is necessary to know the magnetic properties of steel under the same conditions. Such an analysis was carried out by L. Xiao *et al.* (2019) who found that the relative permeability at low flux densities increases with increasing temperature and decreases at higher flux densities. At the same time, when the compressive stress exceeds 50 MPa, the effect of compressive stress on the relative permeability and iron loss decreases. The relative permeability and iron loss of electrical steel sheets were experimentally determined at conditions from 30°C to 200°C and from 0.1 MPa to 140 MPa. The study by A. Boehm & I. Hahn (2014) and A. Yao *et al.* (2018) measures the magnetic properties of steel and other soft magnetic, electrically conductive materials at high temperatures up to the Curie temperature and above. The measurements show that the saturation polarisation decreases slightly up to 500°C and then drops to zero at temperatures above 700°C. The peculiarity of the considered methods and results of research on electromechanical transducers is the stationary temperature conditions of the surrounding cooling medium. However, for a wide class of multifunctional electromechanical converters for technological purposes, studies with nonlinear changes in the load-cooling medium become relevant.

Transient processes that occur when the rotor temperature fluctuates with changes in ambient temperatures

are accompanied by the appearance of harmonics of currents and rotor magnetomotive force. Figure 8 shows the temperature distribution in the cross-section of an electric screw unit for grinding and pyrolysis of plant waste biomass at a rotor speed of 10 rpm in the mode of gradual filling of the screw, provided that the lower part of the rotor (area G_1, Fig. 3) is immersed in a bulk material. In this zone, endothermic reactions and intensive heat transfer from the rotor to the raw material occur. The upper part of the rotor (area G_2, Fig. 3) is in contact with air, the thermal conductivity of which at temperatures above 250°C is 0.025 W/m·K, which is an order of magnitude less than the thermal conductivity of the raw material being processed. From the presented results, it follows that the temperature difference between the lower and upper parts of the rotor can reach 60-80°C. The stator winding temperature does not reach the maximum permissible values for electrical insulation.

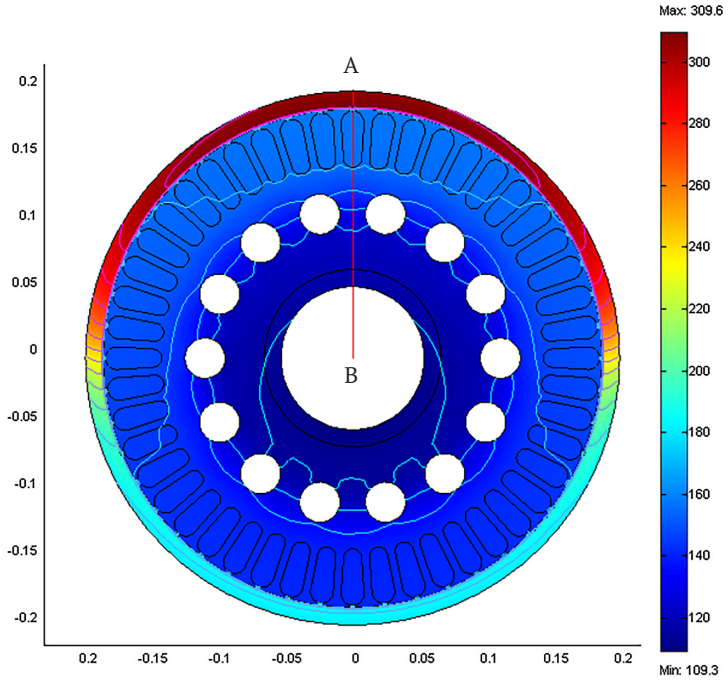

Figure 8. Temperature distribution in the cross-section of an electric screw unit at a rotor speed of 10 rpm in the mode of gradual filling of the screw

Source: compiled by the authors

In the operating zones of the twin-screw electromechanical hydrolyser (Fig. 9), which are located between the rotors, a significant (up to 60) difference in the temperature of the rotors is observed compared to the zones located between the screw and the wall of the reaction chamber.

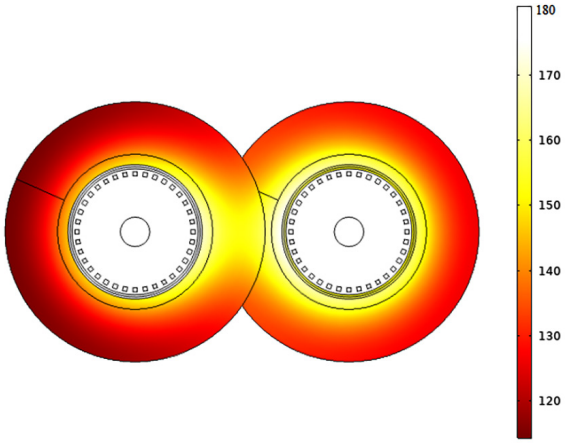

Figure 9. Heating of electromagnetic parts of a twin-screw electromechanical hydrolyser

Source: compiled by the authors

The literature compares different cooling methods, their volumetric flow rates and other machine parameters concerning continuous power for EM designs with both internal and external rotors. M. Vukotić *et al.* (2023) conducted an analysis using experimental testing and computational fluid dynamics modelling to derive a generalised analytical equation for the stator winding calculation related to blade geometry and rotor speed. As the machine size increases, winding cooling becomes less efficient for heat sources in the centre of the machine, while the heat transfer in the cooling jacket increases. R. Lehmann *et al.* (2022) proved that sensitivity studies of other machine parameters, such as the maximum allowable magnet temperature or the coolant inlet temperature (oil or water), improve the understanding of how to increase continuous EM power when rotor temperature limits performance. A. Tovar-Barranco *et al.* (2020) proposed a methodology for obtaining convection heat transfer coefficients for synchronous motor windings using concentrated parameters. However, these publications do not consider models for increasing the efficiency of an electric machine by thermal integration and the use of the dissipative component of energy for the implementation of technological processes in which EM is involved.

Analysing the current spectrograms obtained experimentally (Fig. 10-12), it can be noted that the higher harmonics in the frequency range (0 ... 500 Hz) are less pronounced than in the voltage spectrograms, but still more pronounced at frequencies of 101 Hz, 105 Hz, 145 Hz, 245 Hz, and 375 Hz. In the range from 0 to 50 kHz, the current spectrograms show harmonics of the following frequencies: 1 kHz; 7 kHz; 15 kHz; 17 kHz; 28.5 kHz; 33 kHz; 35 kHz; 43 kHz.

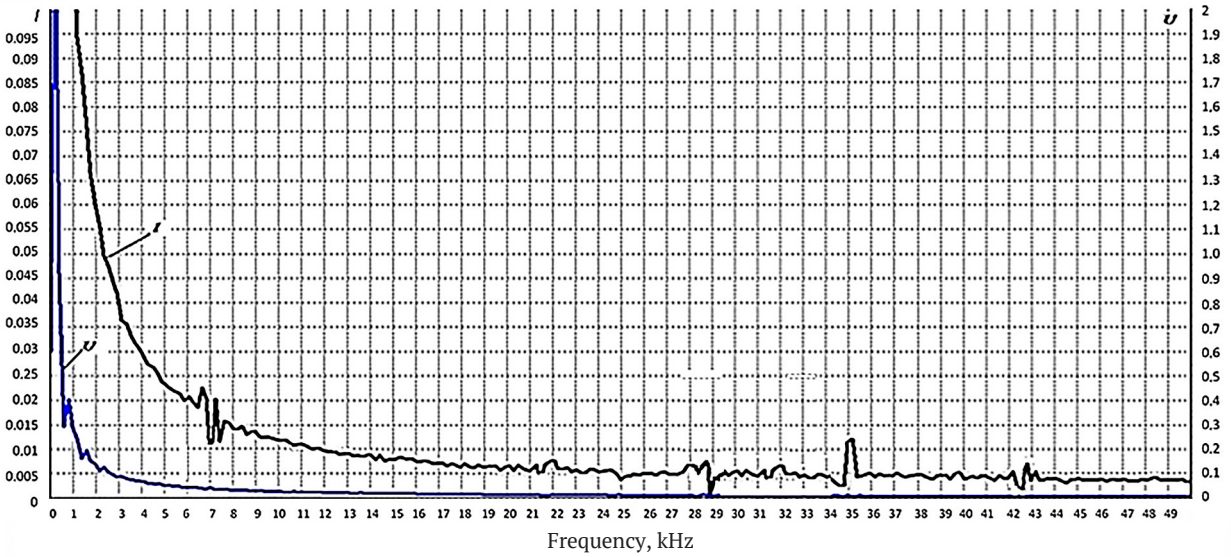

Figure 10. Harmonic composition of current and voltage in the range of up to 50 kHz in the idle mode of the screw
Source: compiled by the authors

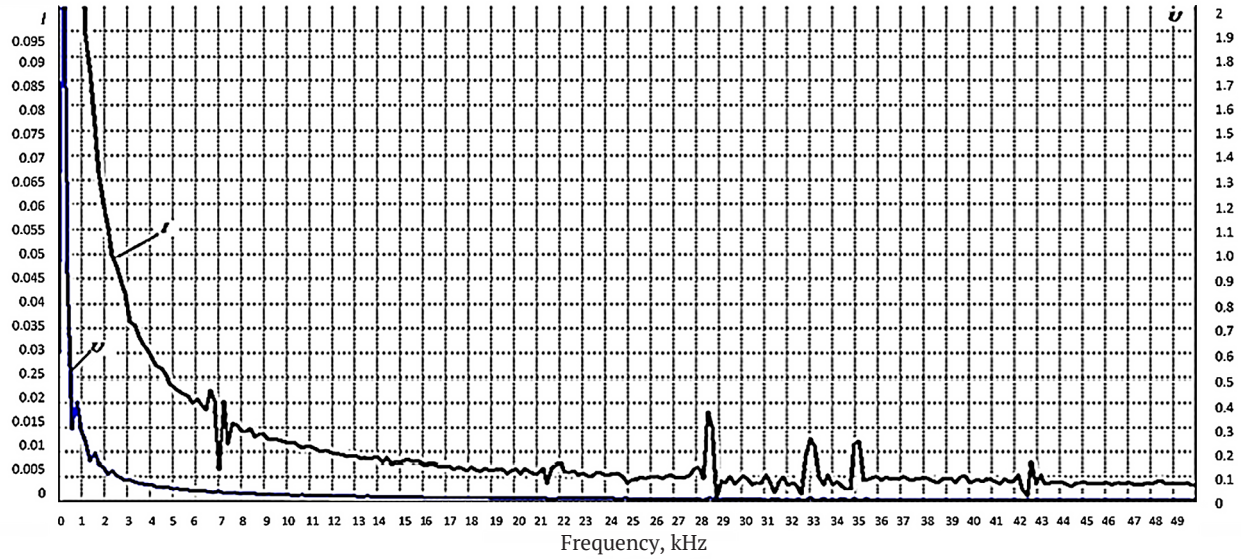

Figure 11. Harmonic current and voltage composition in the range of up to 50 kHz for gradual screw-filling mode
Source: compiled by the authors

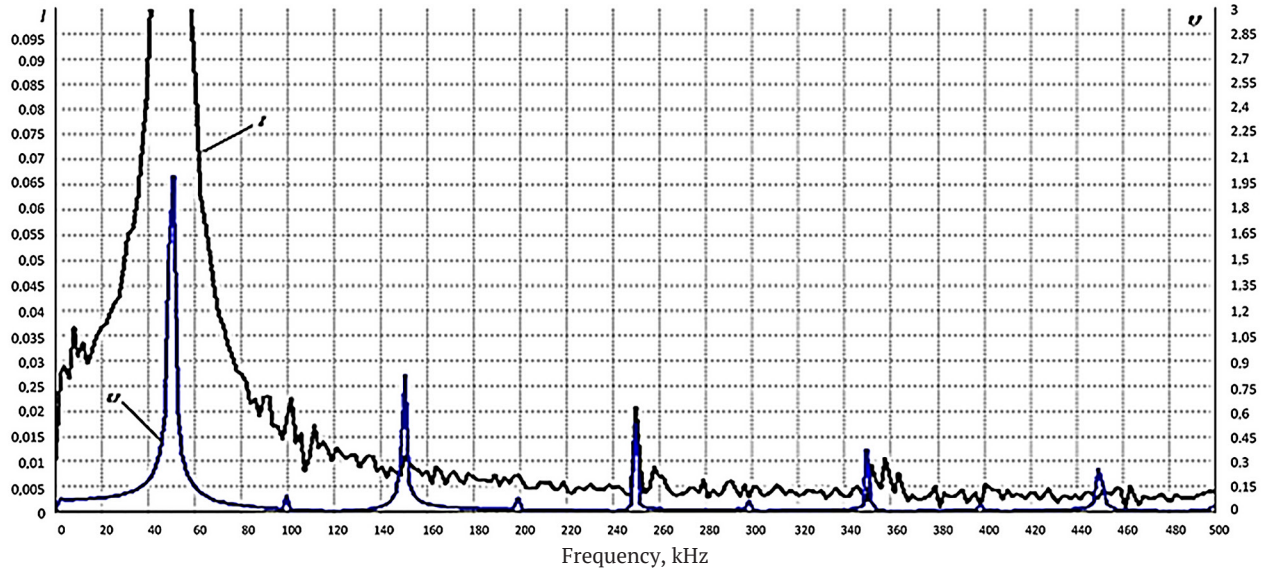

Figure 12. Harmonic current and voltage composition in the range of up to 500 Hz for gradual screw-filling mode
Source: compiled by the authors

In the case of nonlinear temperature changes in the induction machine environment, higher time-dependent harmonics arise, and the magnetic field shape becomes deformed. The highest values of higher harmonic amplitudes occur during thermal shocks. S. Bjelić *et al.* (2011) experimentally registered the appearance of such harmonics, but no theoretical justification for this phenomenon was proposed. A. Funke *et al.* (2018) found the inefficiency of the screw converter in the initial mixing area, which leads to uneven heat transfer under suboptimal conditions. J. Muñoz Tabora *et al.* (2020) conducted a comparative analysis of the effect of harmonic voltages on the performance and temperature rise of IE2, IE3, and IE4 electric motors. The results show that under ideal operating conditions, the permanent magnet motor of class IE4 has better consumption and temperature performance but has nonlinear characteristics. In the presence of voltage harmonics, this scenario completely changes according to the harmonic content. To analyse the effect of harmonics on the motor temperature rise, a statistical analysis using Spearman correlation matrices is presented.

Comparing the current spectrograms in Figure 10 and Figure 11, it is possible to note the difference in amplitudes and the presence of certain harmonics for the idle screw mode and the gradual screw-filling mode. This is especially evident at frequencies of 7 kHz, 28.5 kHz, 33 kHz, and 35 kHz, which confirms the effect of generating higher harmonics when the temperature of the medium surrounding the rotor screw changes. The main factor that influenced the generation of higher harmonics of these frequencies should be considered the presence of a free (aperiodic) component of changes in the temperature of the rotor of the screw electromechanical converter over time with sinusoidal fluctuations in the temperature of the medium.

The modifications of electromechanical converters for technological purposes proposed in this study provide regulation of heat and mass transfer due to the two-way supply of thermal energy to raw materials and the ability to directly influence the technological process through the parameters and characteristics of the electromagnetic system. At the same time, a mathematical model (algorithm) can be introduced to determine the state of the induction machine, as well as a modelling procedure for measuring certain values in MATLAB, which is presented in N. Marković *et al.* (2017). The measurement process in the system is gradually developing and improving as a combination of information and results of previous modelling steps with new elements, for example, when the stator windings of the motor and braking modules of the electromechanical converter are powered by a frequency converter, respectively.

In terms of the physics of thermomagnetic processes, the results of the electric screw machine research are comparable to those of thermomagnetic motors (Hey *et al.*, 2022). A thermomagnetic motor uses a change in the magnetic resistance of a thermomagnetic material to generate a force or torque, in which there is a temperature fluctuation as it rotates. The rate of temperature change in the thermomagnetic material can be estimated from the thermal time constant of the first-order system, similar to Equation (1). Based on the known physical properties and heat transfer parameters, the time constant is also several seconds. According to the research of J. Hey *et al.* (2022), in a thermomagnetic motor, in which temperature fluctuations occur as the rotor rotates at a speed of 11 rpm, fluctuations in force or torque are observed with a frequency of 0.75 Hz. In our studies of the electric screw unit at a rotor speed in the range of 10…45 rpm in the mode of gradual filling of the screw in the harmonic composition of currents (Fig. 12), we also observe frequencies of 0.17…0.75 Hz. However, unlike in the study of J. Hey *et al.* (2022), the appearance of a spectrum of low-frequency

and high-frequency harmonics in an electric screw unit is mainly due not to changes in the magnetic permeability of the magnetic material, but to changes in the rotor resistivity and the depth of current penetration with fluctuations in the rotor temperature.

D. Solomon (1988) suggested a conceptual model of a thermomagnetic generator, stating that the efficiency of a thermomagnetic generator can be increased if the magnetic field is also cyclically changing, as well as the properties of the material to which it is applied. This is the scenario implemented in our electric screw unit in the low-frequency harmonic region.

Among the existing publications, there are many studies devoted to the study of thermal processes occurring in screw converter devices. F. Campuzano *et al.* (2019) studied the effects of heat transfer on the processed material. The heat transfer effect in a twin-screw converter was found to be better than in a single-screw converter. This effect is confirmed in these studies, as well as by Zablodskiy *et al.*, 2022. F. Qi & M.M. Wright (2020) performed mathematical modelling of the processes of hydrodynamics, heat transfer, and chemical reactions of particles in a twin-screw converter. The proposed F. Qi & M.M. Wright's (2020) models in combination with the models of electromagnetic and thermal processes of this work can be considered as a direction for further research, provided that the heat of reaction parameter is carefully calibrated to improve the kinetic model.

An important result of this study is the theoretical and practical confirmation of the existence of an additional spectrum of harmonics arising from sinusoidal fluctuations in the temperature of the load-cooling medium. Based on the possibilities of implementing structural, functional, and thermal integration in the proposed modifications of screw electromechanical converters for technological purposes, the identified spectrum of harmonics participates in the formation of both the dynamics of the rotating system and additional thermal power. This contributes to an increase in the overall efficiency of the screw electromechanical converter.

CONCLUSIONS

The creation of electromechanical converters for technological purposes is based on the idea of combining one electromechanical device simultaneously heating, transporting, magneto-oscillating, mixing functions, integrating thermal energy, and directing the latter to the raw material processing zone. The peculiarity of the considered modifications of the electromechanical converter for technological purposes is that the processed raw material acts as a loading and cooling medium.

The effect of the appearance of the spectrum of higher harmonics in the air gap under nonlinear changes in the temperature of the medium is theoretically substantiated for applications in a twin-screw electromechanical hydrolyser and an electric screw unit for grinding and pyrolysis of biomass of plant waste.

A mathematical model of interconnected electromagnetic and thermal processes is proposed due to the mutual influence of temperature, electrical conductivity, eddy current density, and specific heat losses. Based on the results of numerical modelling, the temperature distribution in the cross-section of the electric screw unit at a rotor speed of 10 rpm in the mode of gradual filling of the screw and the level of heating of the electromagnetic parts of the twin-screw electromechanical hydrolyser were determined.

The appearance of a spectrum of higher harmonics in the range from zero to 50 kHz in an electric screw unit for grinding and pyrolysis of biomass of plant waste has been experimentally recorded. The presence of higher harmonics contributes to an increase in the share of useful thermal energy.

Further research can be devoted to the development of designs and control systems for industrial models of high-temperature screw electromechanical units.

ACKNOWLEDGEMENTS

This work was supported by the Ministry of Education and Science of Ukraine (№0123U102165).

CONFLICT OF INTEREST

The authors declare no conflict of interest.

REFERENCES

[1] Bjelić, S., Marković, N., & Jakšić, U. (2011). The simplified procedure for calculation of the influence of thermal losses on decrease of technical endurance of electric equipment. In *Conference on Industrial Energy and Environmental Protection IEEP'11* (p. 28). Belgrade, Serbia.

[2] Boehm, A., & Hahn, I. (2014) Measurement of magnetic properties of steel at high temperatures. In *40th annual conference of the IEEE industrial electronics society* (pp. 715-721). doi: 10.1109/IECON.2014.7048579.

[3] Campuzano, F., Brown, C.R., & Martínez, J.D. (2019). Auger reactors for pyrolysis of biomass and wastes. *Renewable and Sustainable Energy Reviews*, 102, 372-409. doi: 10.1016/j.rser.2018.12.014.

[4] Elmadah, H., Roger, D., & Takorabet, N. (2019). Design of inorganic coils for high temperature electrical machines. *Open Physics*, 17(1), 698-708. doi.org/10.1515/phys-2019-0072.

[5] Feng, C., Li, Z., Wang, Z., Wang, B., & Wang, Z. (2019). Optimizing torque rheometry parameters for assessing the rheological characteristics and extrusion processability of wood plastic composites. *Journal of Thermoplastic Composite Materials*, 32(1):123-140. doi: 10.1177089270571774482 8.

[6] Funke, A., Grandl, R., Ernst, M., & Dahmen, N. (2018). Modelling and improvement of heat transfer coefficient in auger type reactors for fast pyrolysis application. *Chemical Engineering and Processing – Process Intensification*, 130, 67-75. doi: 10.1016/j.cep.2018.05.023.

[7] Gritsyuk, V., Nevliudov, I., Zablodskiy, M., & Subramanian, P. (2022). Estimation of eddy currents and power losses in the rotor of a screw electrothermomechanical converter for additive manufacturing. *Machinery & Energetics*, 13(2), 41-49. doi: 10.31548/machenergy.13(2).2022.41-49.

[8] Hey, J., Tan, J.L., & Tan, Z.H. (2022). An evaluation of thermomagnetic motors for heat energy harvesting. In *2022 IEEE/ASME International Conference on Advanced Intelligent Mechatronics* (pp. 1347-1354). Sapporo, Japan. doi: 10.1109/AIM52237.2022.9863263.

[9] Juszczak, E.N., Roger, D., Komeza, K., Lefik, M., & Napieralski, P. (2020). Architecture choices for high-temperature synchronous machines. *Open Physics*, 18(1), 683-700. doi: 10.1515/phys-2020-0154.

[10] Laidoudi, A., Duchesne, S., Morganti, F., & Velu, G. (2020). High-power density induction machines with increased windings temperature. *Open Physics*, 18(1), 642-651. doi: 10.1515/phys-2020-0131.

[11] Lefik, M., Komeza, K., Napieralska-Juszczak, E., Roger, D., & Napieralski, P.A. (2019). Comparison of the reluctance laminated and solid rotor synchronous machine operating at high temperatures. *COMPEL-The international journal for computation and mathematics in electrical and electronic engineering*, 38(4), 1111-1119. doi: 10.1108/COMPEL-10-2018-0405.

[12] Lehmann, R., Künzler, M., Moullion, M., & Gauterin, F. (2022). Comparison of commonly used cooling concepts for electrical machines in automotive applications. *Machines*, 10(6), article number 442. doi: 10.3390/machines10060442.

[13] Marković, N., Bjelić, S., Živanić, J., & Jakšić, U. (2017). Simulation of the impact of higher harmonics on the transient process of induction machine fed from PWM inverters. *Tehnički Vjesnik*, 24(1), 265-271. doi: 10.17559/TV-20150502231618.

[14] Mazlan, M.M., Talib, R.A., Mail, N.F., Taip, F.S., Chin, N.L., Sulaiman, R., Shukri, R., & Mohd Nor, M.Z. (2019). Effects of extrusion variables on corn-mango peel extrudates properties, torque and moisture loss. *International Journal of Food Properties*, 22, 54-70. doi: 10.1080/10942912.2019.1568458.

[15] Muñoz Tabora, J., de Lima Tostes, M.E., Ortiz de Matos, E., Mota Soares, T., & Bezerra, U.H. (2020). Voltage harmonic impacts on electric motors: A comparison between IE2, IE3 and IE4 induction motor classes. *Energies*, 13(13), article number 3333. doi: 10.3390/en13133333.

[16] Mushtruk, M., Gudzenko, M., Palamarchuk, I., Vasyliv, V., Slobodyanyuk, N., Kuts, A., Nychyk, O., Salavor, O., & Bober, A. (2020). Mathematical modeling of the oil extrusion process with pre-grinding of raw materials in a twin-screw extruder. *Potravinarstvo Slovak Journal of Food Sciences*, 14, 937-944. doi: 10.5219/1436.

[17] Patent of Ukraine No. 125774 (2022, June). Retrieved from https://sis.ukrpatent.org/uk/search/detail/1690697/.

[18] Qi, F., & Wright, M.M. (2020). A DEM modeling of biomass fast pyrolysis in a double auger reactor. *International Journal of Heat and Mass Transfer*, 150(2), article number 119308. doi: 10.1016/j.ijheatmasstransfer.2020.119308.

[19] Singha, P., & Muthukumarappan, K. (2016). Effects of processing conditions on the system parameters during single screw extrusion of blend containing apple pomace. *Journal of Food Process Engineering*, 40(4), article number e12513. doi: 10.1111/jfpe.12513.

[20] Solomon, D. (1988). Improving the performance of a thermomagnetic generator by cycling the magnetic field. *Journal of Applied Physics*, 63(3), 915-921. doi: 10.1063/1.340033.

[21] Subramanian, R.S. (2014). *Conduction in the cylindrical geometry*. Retrieved from https://web2.clarkson.edu/projects/subramanian/ch330/notes/Conduction%20in%20the%20Cylindrical%20Geometry.pdf.

[22] Tovar-Barranco, A., López-de-Heredia, A., Villar, I., & Briz, F. (2020). Modeling of end-space convection heat-transfer for internal and external rotor PMSMs with fractional-slot concentrated windings. *IEEE Transactions on Industrial Electronics*, 68(3), 1928-1937. doi: 10.1109/TIE.2020.2972471.

[23] Vukotić, M., Lutovski, S., Šutar, N., Miljavec, D., & Čorović, S. (2023). Thermal effects in the end-winding region of electrical machines. *Energies*, 16(2), article number 930. doi: 10.3390/en16020930.

[24] Xiao, L., Yu, G., Zou, J., Xu, Y., & Liang, W. (2019). Experimental analysis of magnetic properties of electrical steel sheets under temperature and pressure coupling environment. *Journal of Magnetism and Magnetic Materials*, 475, 282-289 doi: 10.1016/j.jmmm.2018.11.107.

[25] Yao, A., Odawara, S., & Fujisaki, K. (2018). Iron loss and hysteretic properties under PWM inverter excitation at high ambient temperatures. *IEEJ Journal of Industry Applications*, 7(4), 298-304. doi: 10.1541/ieejjia.7.298.

[26] Zablodskiy, M., Zhyltsov, A., Nalyvaiko, V., Trokhaniak, V., Pugalendhi, S., & Subramanian, P. (2020). Biomass pyrolysis using a multifunctional electromechanical converter and a magnetic field. *Scientia Agriculturae Bohemica*, 51(2), 65-73. doi: 10.2478/sab-2020-0009.

[27] Zablodskiy, M.M., Kovalchuk, S.I., Pliuhin, V.E., & Tietieriev, V.O. (2022). Indirect field-oriented control of twin-screw electromechanical hydrolyzer. *Electrical Engineering & Electromechanics*, 1, 3-11. doi: 10.20998/2074-272X.2022.1.01.

[28] Zhang, S.B., Zheng, X.W., Feng, L.J., Wang, Y.F., & Liu, Z.F. (2016). The design and experimental research of cooling structure in deep well submersible motor. *Journal of Discrete Mathematical Sciences and Cryptography*, 19(3), 837-848. doi: 10.1080/09720529.2016.1197571.

[29] Zou, J., Qi, W., Xu, Y., Xu, F., Li, Y., & Li, J. (2012). Design of deep sea oil-filled brushless DC motors considering the high pressure effect. *IEEE Transactions on Magnetics*, 48(11), 4220-4223. doi: 10.1109/TMAG.2012.2204731.

Кшиштоф Мудрик
Професор
Університет сільського господарства в Кракові
30-149, пр. Адама Міцкевича, 21, м. Краків, Польща
https://orcid.org/0000-0002-6212-6958

Тарас Гуцол
Професор
Університет сільського господарства в Кракові
30-149, пр. Адама Міцкевича, 21, м. Краків, Польща
https://orcid.org/0000-0002-9086-3672

Микола Миколайович Заблодський
Доктор технічних наук, професор
Національний університет біоресурсів і природокористування України
03041, вул. Героїв Оборони, 15, м. Київ, Україна
https://orcid.org/0000-0001-8889-8158

Дмитро Сергійович Сорокін
Кандидат технічних наук, доцент
Національний університет біоресурсів і природокористування України
03041, вул. Героїв Оборони, 15, м. Київ, Україна
https://orcid.org/0000-0002-1762-9724

Сергій Миколайович Усенко
Кандидат технічних наук, доцент
Національний університет біоресурсів і природокористування України
03041, вул. Героїв Оборони, 15, м. Київ, Україна
https://orcid.org/0000-0001-7225-9589

Дослідження електротепломеханічного перетворювача технологічного призначення при нелінійних змінах навантажувально-охолоджуючого середовища

Анотація. У сучасному екологічному контексті актуальною стає необхідність оптимізувати технологічні процеси з важкими температурними навантаженнями, забезпечуючи високу надійність і об'єднуючи обертові частини електричних машин з виконавчими механізмами, з метою досягнення більшої ефективності електромеханічних перетворювачів. Метою дослідження було теоретичне обґрунтування та експериментальне підтвердження ефекту появи вищих гармонік в повітряному зазорі при нелінійній зміні температури середовища. Дослідження ґрунтуються на основних положеннях електродинаміки, тепломасообміну, математичного моделювання методом скінченних елементів і експериментальній перевірці мультифізичних параметрів. На основі аналізу диференціального рівняння для визначення приросту температури поверхні феромагнітного ротора в умовах нелінійної зміни температури середовища, що оточує електромеханічний перетворювач, встановлені закономірності формування вільної і вимушеної складової миттєвих значень температури массивного ротора. В залежності від режиму взаємодії навантажувально-охолоджуючого середовища і електромеханічної частини шнекових агрегатів сформовані кінематичні схеми одномасової та двомасових систем зі змінними або постійними моментами інерції та жорсткістю. Згідно розмірів електромагнітної системи експериментального зразка побудована математична модель для досліджень теплових і електромагнітних процесів. Визначено закономірності просторового розподілу температури шнекового електромеханічного агрегата. Експериментально встановлені спектри вищих гармонік напруги та струму в діапазоні частот від 0 до 50 кГц, що підтверджує наявність ефекту генерування вищих гармонік при зміні температури середовища, що оточує ротор-шнек. Виявлений спектр гармонік впливає як на формування динаміки обертової системи, так і додаткової теплової потужності, підвищуючи при цьому загальний коефіцієнт корисної дії шнекового електротепломеханічного перетворювача. Практична цінність отриманих результатів полягає в можливості прогнозування оптимальних показників взаємопов'язаних електромагнітних і теплообмінних процесів в шнекових електромеханічних перетворювачах технологічного призначення

Ключові слова: спектр вищих гармонік; феромагнітний порожнистий ротор; біомаса; температурне поле; електромагнітне поле; конструктивно-технологічна схема

Machinery & Energetics
Vol. 14, No. 2. 2023

Journal homepage:
https://technicalscience.com.ua/en

UDC 621.316.1.05
DOI: 10.31548/machinery/2.2023.23

Viktor Kaplun*
Doctor of Technical Sciences, Professor
National University of Life and Environmental Sciences of Ukraine
03041, 15 Heroiv Oborony, Kyiv, Ukraine
https://orcid.org/0000-0001-7040-9344

Oleksandr Gai
PhD in Technical Sciences, Associate Professor
National University of Life and Environmental Sciences of Ukraine
03041, 15 Heroiv Oborony, Kyiv, Ukraine
https://orcid.org/0000-0001-5460-7260

Petro Stetsyuk
Doctor of Physical and Mathematical Sciences, Senior Researcher
V.M. Glushkov Institute of Cybernetics of the National Academy of Sciences of Ukraine
03187, 40 Academician Glushkov Ave., Kyiv, Ukraine
https://orcid.org/0000-0003-4036-2543

Andrii Ivlichev
Leading Software Engineer
V.M.Glushkov Institute of Cybernetics of the National Academy of Sciences of Ukraine
03187, 40 Academician Glushkov Ave., Kyiv, Ukraine
https://orcid.org/0009-0005-2823-6204

Provision of optimal dispatching scenarios for regional power systems in the face of uncontrollable power shortages

Abstract. As of 2023, substantiation of the criteria for optimal load balancing of territorial energy islands in the face of uncontrolled power shortages due to unpredictable failure (destruction as a result of military bombardment) of the upper (trunk) level energy infrastructure is relevant. The research aims to substantiate approaches to ensuring the controlled operation of regional power systems under conditions of power shortages. The study applied the theory and methods of mathematical analysis of complex multicomponent systems in the form of mixed Boolean linear programming. A Mathematical Programming Language and modelling methods of the NEOS server based on the Gurobi solver were used to describe the modes of operation of power grids. A proportional power distribution method between load nodes of the post-emergency network configuration was used to determine the direction of electricity transit with the least losses. An algorithm and a program for solving the problem of addressing flows and power losses in multi-node regional power systems are proposed. The optimisation problem is formulated in the form of a mixed Boolean linear programming model with the criterion of minimising the power momentum, considering balance constraints and upper limits on the power between supply and load nodes. The developed transport matrix made it possible to find the optimal power distribution for emergency and post-emergency modes according to the criterion of minimum network losses. Algorithms and scenarios for the response of dispatching services were formed, considering the capacity of power grids and determining temporary power supply schemes, the configuration of which will ensure the "survivability" of energy islands. The levels of efficiency of the Boolean linear programming model associated with the connectivity of the cycles of the transport problem and

Article's History: Received: 30/12/2022; Revised: 03/04/2023; Accepted: 26/04/2023.

Suggested Citation:
Kaplun, V., Gai, O., Stetsyuk, P., & Ivlichev, A. (2023). Provision of optimal dispatching scenarios for regional power systems in the face of uncontrollable power shortages. *Machinery & Energetics,* 14(2), 23-33. doi: 10.31548/machinery/2.2023.23.

*Corresponding author

the order of traversal of its vertices for test examples depending on the constraints imposed on the components of the network structure are established. The process of tracking electricity flows will allow for establishing routes connecting specific electricity supply nodes with load nodes and determining their shares in covering the energy island's demand under conditions of power shortage

Keywords: moment minimisation criterion; energy island; transport matrix; Boolean linear programming; load balancing

INTRODUCTION

The basic chain of functioning of the current integrated power system of Ukraine consists of generation facilities, a transmission system (trunk power grids), a distribution system (distribution networks of lower voltage classes) and end consumers. Disruption of this basic pathway of electricity supply in wartime and in the context of the russian aggressor's bombing of the energy infrastructure leads to disruption of existing electricity supply schedules, power shortages due to reduced generation and the impossibility of its transportation through trunk and distribution networks.

Some of the generating capacities are destroyed, shut down or located in the occupied territories. Power plants located near the frontline under artillery fire have a special mode of operation. All this leads to a power shortage and a limited electricity consumption schedule compared to peacetime.

Following A. Izvoshchikova (2022), the amount of damage to the electricity infrastructure reaches 40-50% of power facilities. This indicates an existing systemic problem, which is a shortage of capacity due to damage not only to power plants but also to trunk grids. It is the transmission system that has suffered the most damage. In this situation, the problem of energy supply needs to be addressed at the network level. To a large extent, distribution system operators cannot transport electricity through trunk grids which is the main reason for the power shortage and leads to the introduction of electricity consumption limits in regional grids.

Since the damage is uneven and random, outage plans are formed accordingly. This circumstance greatly complicates the work of distribution system operators' dispatch services. The situations described above require not only a limited allocation of capacities permitted by the upper dispatch level but also changes (in most cases) in the configuration of the distribution network. This, in turn, leads to abnormal grid operation modes and incorrect operation of relay protection and automation.

H. Nosova (2022) noted that the most famous blackouts in history were in the United States (New York, 1977) and Brazil (1999). In recent years, the most famous mass blackouts have occurred in the United States – in California (2019) and Texas (2021).

X. Zhu *et al.* (2020), J. Naughton *et al.* (2021) and S. Bruno *et al.* (2022) devoted their research to the issues of ensuring optimal scenarios for the dispatching of regional power systems, in which they revealed this problem to a certain extent, but without considering the conditions of uncontrollable power shortages. As for the analysis of studies indirectly related to the issue of substantiating approaches to ensuring the resilience of regional power systems under conditions of power shortages, the material of Y. Jiang *et al.* (2018), R. Rai & K. Nagasaka (2018), H. Shang *et al.* (2020) indicates the expediency of a detailed consideration of the formation of algorithms and scenarios for the response of dispatch services, taking into account the capacity of power grids and the definition of temporary power supply schemes, the configuration of which will ensure the "survivability" of energy islands.

J. Xu *et al.* (2020) pointed out that extreme weather events cause power outages in active distribution systems and proposed a multi-stage switching strategy based on dynamic programming (DP), taking into account both islanding and fault reconfiguration and found a trade-off between minimising the overall power deficit and minimising the number of switching operations throughout the duration of the event, However, they did not track the power flows to establish the routes connecting specific power supply nodes to load nodes and determine their share in covering the energy island's demand under power shortage conditions.

V. Hosseinnezhad *et al.* (2018) formed an optimal systematic strategy for restoring the distribution network after emergencies due to serious failures and developed a two-stage solution procedure using graph theory and adjusting the results but did not consider the proportional distribution of power between load nodes of the new (post-emergency) network configuration, which allows determining the direction of electricity transit with the least losses.

Therefore, the issue of ensuring optimal scenarios for the dispatching of regional power systems in the face of uncontrollable power shortages is relevant.

The research aims to develop and substantiate approaches aimed at ensuring the controlled operation of regional power systems in cases of power shortages. For this goal, it was necessary to create algorithms and scenarios for the response of dispatch services that consider the capacity of power grids and determined temporary power supply schemes.

MATERIALS AND METHODS

The theory and methods of mathematical programming are used to provide optimal scenarios. The optimisation problems are formulated in the form of mixed Boolean linear programming problems. The AMPL modelling language was used to describe them. The Gurobi solver (n.d.) with NEOS Server (n.d.) was used to solve the optimisation problems.

The study used the proportional division method. The method is based on the fact that power flows and total losses between nodes are divided equivalently to power moments P_iL_i. The disadvantages of this method are that it ignores the unfair distribution of losses between the nodes of the trunk network and the distribution system, in particular, the imbalance of losses of the base and balancing nodes.

A network consisting of n nodes and m branches was considered. Figure 1 shows a generalised block diagram of the distribution of power flows in a regional power system.

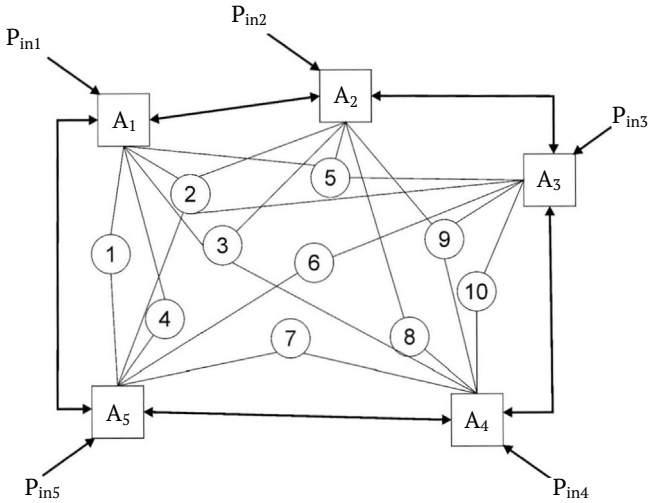

Figure 1. Generalised block diagram of power flows distribution in the energy island network
Source: compiled by the authors

To solve the problem of distributing power flows, it was necessary to record the initial data to be used in the calculation, namely the columnar incident matrices M specify the power of the nodes of set A, the demand of the load nodes of set B and the value of the power transmitted in each branch of the graph, otherwise, the values are zero. In this study, several incident matrices M were considered for five nodes of set A, each of which can be a balancing node and thus form a new (temporary) configuration of the power grid, and ten load nodes of set B. Incident matrices M establish the relationship between nodes and branches of a directed network graph. The notation used is that each element of the M_{is} matrix is located at the intersection of the i-th row (corresponding to the i-th node) and the s-th column (corresponding to the (i-j)th branch).

The optimisation problems (Bila *et al.,* 2022) were solved using the Gurobi solver available on the NEOS server. To describe the models of linear Boolean programming problems (Fourer *et al.,* 2003), we used the modelling language AMPL (A Mathematical Programming Language).

Figure 2 shows a graphical interpretation of the configuration of the possible distribution of power flows in the model power system, described below.

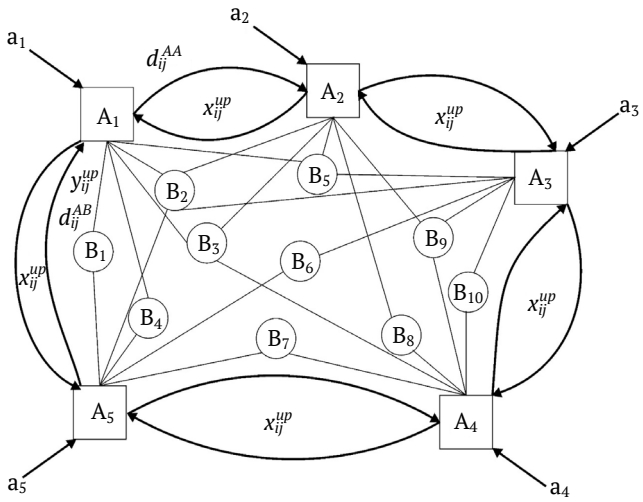

Figure 2. Graphical interpretation of the possible distribution of power flows in a model power system
Source: compiled by the authors

To solve this problem, the power grid is represented as a directed graph, which is a set of nodes and branches connected. Tracing the power transmission paths between the nodes of set A (the backbone network) can be performed in two directions: using the main power supply scheme (forward tracing) and using temporary schemes (backward tracing). Power transfers between the nodes of set A and the load nodes of the energy island (set B) are allowed in any direction, provided that the 1st Kirchhoff law is fulfilled, and the grid capacity is not exceeded.

The initial data and corresponding notation for the mathematical model are:

- a set of nodes of a higher voltage class (supply nodes) A;
- a set of nodes of a lower voltage class (load nodes) B;
- the set of links (branches of edges) of "supply nodes – supply nodes" $E_{AA} \subset A \times A$;
- the set of links (edge) of "supply nodes – load nodes" $E_{AB} \subset A \times B$;
- the level of the capacity limit of "supply nodes" $a_i, \forall i \in A$;
- load nodes' demand $b_i, \forall i \in B, \sum_{ieA} a_i \leqslant \sum_{ieB} b_i$;
- lengths (branches of network) of "supply nodes – supply nodes" $d_{ij}^{AA}, \forall (i,j) \in E_{AA}$;
- lengths (branches of network) of "supply nodes – load nodes" $d_{ij}^{AB}, \forall (i,j) \in E_{AB}$;
- upper limits of flows along the edges of the supply nodes-supply nodes network $x_{ij}^{up}, \forall (i,j) \in E_{AA}$;
- upper limits of flows along the edges of the supply nodes-load nodes network $y_{ij}^{up},, \forall (i,j) \in E_{AB}$;

Instead of an undirected graph, an oriented graph was considered, as shown in Figure 2.

The unknown (variable) flows along the branches for the edges of the supply nodes – supply nodes network are represented as follows:

$$x_{ij}^{+} \geqslant 0, i \in A, j \in A, (i,j) \in E_{AA},$$
$$x_{ij}^{-} \geqslant 0, i \in A, j \in A, (i,j) \in E_{AA},$$

and unknown (variable) flows along the branches for the edges of the supply nodes – load nodes network:

$$y_{ij}^{+} \geqslant 0, i \in A, j \in B, (i,j) \in E_{AB},$$
$$y_{ij}^{-} \geqslant 0, i \in A, j \in B, (i,j) \in E_{AB}.$$

Accordingly, the Boolean variables (1 – open branch, 0 – closed branch) will have the form:

$$X_{ij}^{+} \geqslant 0 \vee 1, i \in A, j \in A, (i,j) \in E_{AA},$$
$$X_{ij}^{-} \geqslant 0 \vee 1, i \in A, j \in A, (i,j) \in E_{AA},$$
$$Y_{ij}^{+} \geqslant 0 \vee 1, i \in A, j \in B, (i,j) \in E_{AB},$$
$$Y_{ij}^{-} \geqslant 0 \vee 1, i \in A, j \in B, (i,j) \in E_{AB}.$$

Reconciliation of the power deficit by adjusting power flows in the energy island to find optimal flow distribution points and aims to determine the conditions for meeting the demand of load nodes while minimising power moments and considering the connection between nodes with zero power (idling):

$$M^* = \min_{x,y,X,Y} \left\{ \sum_{(i,j) \in E_{AA}} d_{ij}^{AA} (x_{ij}^{+} + x_{ij}^{-}) + \sum_{(i,j) \in E_{AB}} d_{ij}^{AB} (y_{ij}^{+} + y_{ij}^{-}) + \sum_{(i,j) \in E_{AA}} \varepsilon (X_{ij}^{+} + X_{ij}^{-}) + \sum_{(i,j) \in E_{AB}} \varepsilon (Y_{ij}^{+} + Y_{ij}^{-}) \right\}. \quad (1)$$

under the following limitations:

- supply nodes must use the entire capacity limit (A-balance);

$$\sum_{j:(i,j) \in E_{AA}} (x_{ij}^{+} - x_{ij}^{-}) - \sum_{j:(j,i) \in E_{AA}} (x_{ji}^{+} - x_{ji}^{-}) + \sum_{j:(i,j) \in E_{AB}} (y_{ij}^{+} - y_{ij}^{-}) = a_i, \forall i \in A, \quad (2)$$

- demand at load nodes may not be fully met (B-imbalance):

$$\sum_{i:(i,j) \in E_{AB}} (y_{ij}^{+} - y_{ij}^{-}) \leq b_i, \forall j \in B. \quad (3)$$

Flows can only be sent along the edge branches E_{AA} in one direction without violating the set limit:

$$x_{ij}^{+} \leq x_{ij}^{up} \times X_{ij}^{+}, i \in A, j \in A, (i,j) \in E_{AA},$$
$$x_{ij}^{-} \leq x_{ij}^{up} \times X_{ij}^{-}, i \in A, j \in A, (i,j) \in E_{AA},$$
$$X_{ij}^{+} + X_{ij}^{-} \leq 1, i \in A, j \in A, (i,j) \in E_{AA}. \quad (4)$$

Similarly for edge branches E_{AB}:

$$y_{ij}^{+} \leq y_{ij}^{up} \times Y_{ij}^{+}, i \in A, j \in B, (i,j) \in E_{AB},$$
$$y_{ij}^{-} \leq y_{ij}^{up} \times Y_{ij}^{-} 0, i \in A, j \in B, (i,j) \in E_{AB},$$
$$Y_{ij}^{+} + Y_{ij}^{-} \leq 1, i \in A, j \in B, (i,j) \in E_{AB}. \quad (5)$$

In the objective function (1), a small number ε is used to consider the connection between nodes with zero power (idling) (in the calculations the ε = 0.001 is used).

The algorithm for distributing active power flows includes several stages:

- drawing up a replacement scheme for the power supply system;
- generating information on the nodes of sets A and B (generation limits and demand of the energy island's load nodes) and branches (distances between nodes and the value of the design capacity of the networks);
- creating incident matrices based on the targeting of nodal supply and demand;
- calculation of options for power distribution, considering the constraints;
- analysis of the results obtained justification of the choice of the optimal solution and response scenario of the dispatch service to ensure the survivability of the energy island.

For the numerical implementation of the mathematical model for the power grid scheme of the energy island shown in Figure 1, the initial data given in Table 1 were used.

Table 1. Parameters of the power scheme segment

Node designation	A_1	A_2	A_3	A_4	A_5					
Capacity, MVA	800	700	650	500	450					
Node designation	B_1	B_2	B_3	B_4	B_5	B_6	B_7	B_8	B_9	B_{10}
Capacity, MVA	250	630	400	250	160	160	250	250	500	250
Nodes	A_1A_2	A_2A_3	A_3A_4	A_4A_5	A_5A_1	A_1B_1	A_1B_2	A_1B_3	A_1B_4	A_1B_5
Lengths L_i, km	85	90	110	140	95	13	7	9	15	20
Nodes	A_2B_2	A_2B_3	A_2B_5	A_2B_8	A_2B_9	A_3B_2	A_3B_5	A_3B_6	A_3B_9	A_3B_{10}
Lengths L_i, km	12	15	5	20	15	22	15	20	6	11
Nodes	A_4B_3	A_4B_7	A_4B_8	A_4B_9	A_4B_{10}	A_5B_1	A_5B_2	A_5B_4	A_5B_6	A_5B_7
Lengths L_i, km	25	18	6	17	10	7	17	3	18	13

Source: compiled by the authors

From the nodes of the higher voltage class A_i, a certain power P_{ini} is transferred from the grid to the load nodes of the energy island B_i. It is worth noting that in the above example, the demand of load nodes B_i is set as the value of the total reduced load connected to one network class with the length L_{AiBi} and the average electrical distance from the nodes' vertices A_i to the point of flow distribution.

RESULTS

Normal modes are managed following the dispatch schedule. This should ensure the required reliability of power supply to consumers, power quality and maximum efficiency.

An integrated power system allows for the full use of dispatch management tools for electricity production and consumption, and the transfer of excess energy production from one region to another, although this is not the only reason why the system should be unified. If the integrity of the power system is compromised, there is a need to ensure the survivability of individual energy islands that are formed around existing generation facilities or trunk grid substations.

The resilience of regional power systems should be understood as a rather complex task, namely, to comply with the power consumption levels of energy islands, considering the power limit of the generation system and considering the capacity of the networks involved in the region's power supply.

In 2020-2022, many studies use both matrix and graph algorithms for solving transport problems. A solution to the addressability problem using a matrix approach was obtained by V. Kaplun & V. Osypenko (2020). The solution to the problem of optimal resource allocation allows tracing the paths of power transmission from power supply nodes (substations of trunk grids) to load nodes of the energy island (regional distribution system network) by using the proportional method.

The worst-case scenario for an uncontrolled increase in the power deficit is a partial or complete breakdown of the power system. For example, as a result of one or more system failures, automation is triggered, a large number of consumers are cut off almost simultaneously, and load volumes are sharply reduced. This, in turn, leads to the shutdown of some power plants that are technologically unable to instantly reduce their generation levels. The shutdown of generating capacities causes the next group of consumers to be disconnected, as the frequency in the power system decreases. This process is chain-like and leads to a complete blackout of consumers. In the best-case scenario, it is possible to preserve energy islands with power plants that have gone offline as a result of timely separation from the grid.

Configuring distribution system circuits and determining the duration of connection of load nodes (energy islands) to the grid is a non-trivial task of balancing microgrid systems with an individual set of end users. Damage to power equipment as a result of terrorist attacks requires a non-standard set of real-time solutions from dispatch services.

It is in such circumstances that the development of scenarios to ensure the resilience of microgrid systems and the "survivability" of energy islands by optimising algorithms for dispatch services to respond to uncontrollable power shortages due to unpredictable failure of the backbone energy infrastructure is extremely relevant.

Several realisations of the mathematical model allowed us to obtain directional graphs of the distribution of energy flows and the value of the efficiency of this distribution, provided that the studied structure operates normally ($M^* = 40020$). These calculations do not consider the power losses in the cross-sections of the wires, but the study of the objective function is based on the criterion of the minimum power moment in the branches, which is proportional to the losses.

The simulation results under normal operating conditions of the structure under study between nodes A_i and load nodes B_i are shown in Table 2 and Table 3, respectively.

Table 2. Results of modelling power flow between A_i nodes

Node	Node	x_{ij}^{+}, MW	x_{ij}^{-}, MW	X_{ij}^{+}, MW	X_{ij}^{-}, MW	x_{ij}^{up}, MW	d_{ij}^{AA}, km
A_1	A_2	0	0	0	0	800	35
A_2	A_3	0	0	0	0	800	70
A_3	A_4	0	0	0	0	800	50
A_4	A_5	0	0	0	0	800	25
A_5	A_1	0	0	0	0	800	65

Source: compiled by the authors

Table 3. Results of modelling power flow between nodes A_i and load nodes B_i under normal operating conditions of the studied network structure

Network A note	Network B note	y_{ij}^{+}, MW	y_{ij}^{-}, MW	Y_{ij}^{+}, MW	Y_{ij}^{-}, MW	y_{ij}^{up}, MW	d_{ij}^{AB}, km
A_1	B_1	180	0	1	0	180	13
A_1	B_2	180	0	1	0	180	7
A_1	B_3	180	0	1	0	180	9
A_1	B_4	180	0	1	0	180	15
A_1	B_5	80	0	1	0	180	20
A_2	B_2	180	0	1	0	180	12
A_2	B_3	180	0	1	0	180	15
A_2	B_5	80	0	1	0	180	5
A_2	B_8	80	0	1	0	180	20
A_2	B_9	180	0	1	0	180	15
A_3	B_{10}	170	0	1	0	180	11
A_3	B_2	140	0	1	0	180	22
A_3	B_5	0	0	0	0	180	15
A_3	B_6	160	0	1	0	180	20
A_3	B_9	180	0	1	0	180	6
A_4	B_{10}	80	0	1	0	180	10
A_4	B_3	40	0	1	0	180	25
A_4	B_7	70	0	1	0	180	18
A_4	B_8	170	0	1	0	180	6
A_4	B_9	140	0	1	0	180	17
A_5	B_1	70	0	1	0	180	7
A_5	B_2	130	0	1	0	180	17
A_5	B_4	70	0	1	0	180	3
A_5	B_6	0	0	0	0	180	18
A_5	B_7	180	0	1	0	180	13

Source: compiled by the authors

An alternative representation of the modelling results for optimising flows through given network sections is shown in Figure 3. In this case, the optimal power flow distribution was obtained with the value of the objective function $M^* = 40020$. It is worth noting that in this case, the balance between the power flows entering the nodes A_i from the power system trunk grids and the flows transmitted to the distribution system operators' networks B_i. The levels of transmitted capacities are indicated on the corresponding edges of the graph (Fig. 3).

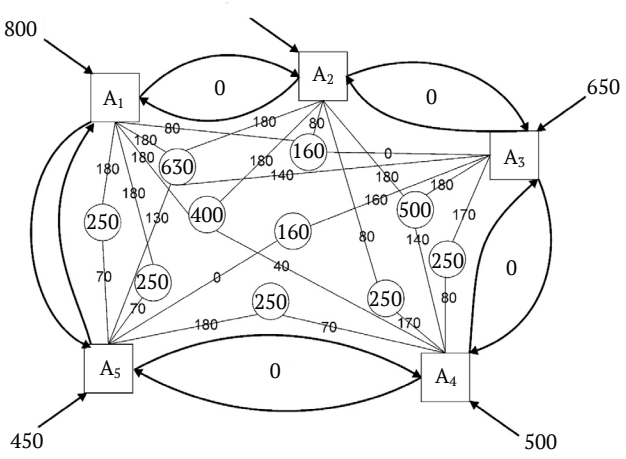

Figure 3. Results of mathematical modelling under the condition of the normal operation of networks
Source: compiled by the authors

The variant with a complete de-energisation of the input lines supplying a certain node A_1, but with preservation of its operating state, while keeping the limits of other nodes A_i, unchanged, is shown in Figure 4. The optimal flow distribution with the value of the objective function $M^* = 26590$ is obtained. It is worth noting that in the absence of a power supply to a certain node A_i, an imbalance between supply and demand of the studied segment of the power system arises (shown in red in Figure 4).

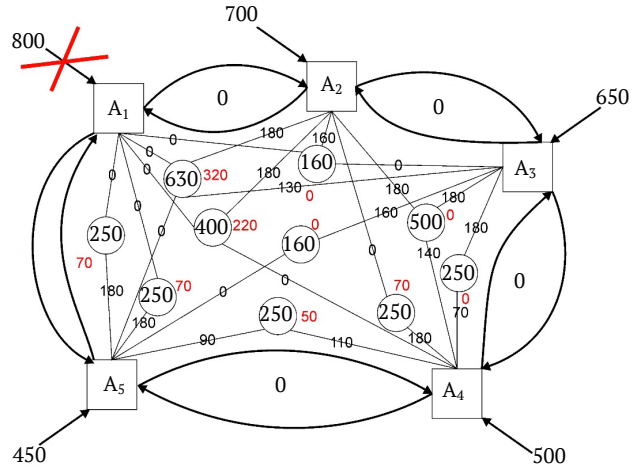

Figure 4. Results of mathematical modelling under the condition of limiting the power of node A_1
Source: compiled by the authors

The variant of the mathematical model implementation with complete de-energisation of the input lines of the energy island supplying a certain node A_i while maintaining its operating state and the condition of proportional change in the power of other nodes of the main grid is shown in Figure 5.

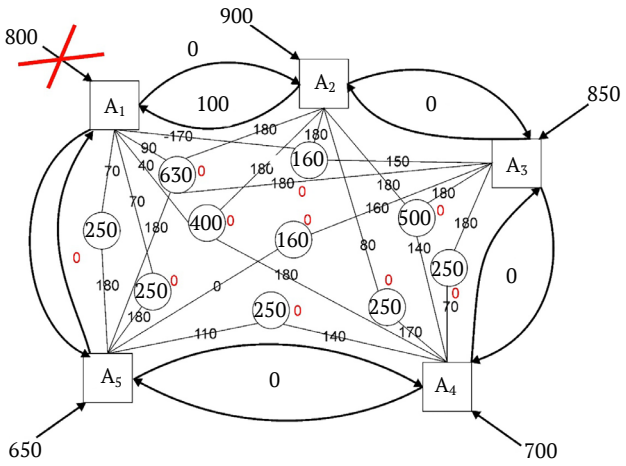

Figure 5. The results of mathematical modelling under the condition of limiting the power of node A_1 and determining the power flows between other nodes A_1
Source: compiled by the authors

The resulting value of the objective function for this case is $M^* = 49790$. It is worth noting that in the absence of a power supply to a certain node A_i and a proportional increase in the power of other nodes of the trunk grid, there is a complete satisfaction of demand from the load nodes. The proposed mathematical model does not consider approaches to the optimal distribution of upper (trunk) level flows, provided that the flow in a node is limited by the minimum loss criterion. At the same time, a proportional increase in the capacity of all operable nodes by the capacity of the node that is out of service was assumed.

DISCUSSION

N. Cai *et al.* (2012) proposed a model that, due to short-term energy shortages in extreme conditions such as earthquakes, tsunamis and hurricanes, flexible dispatch through an efficient energy transmission network, which focuses on the minimum energy recovery time by optimising energy dispatch based on the developed MILP (mixed integer linear programming) model under uncertainty of the initial information, but this model does not consider the efficiency of the selected supply in terms of minimum losses.

A. Ranjan & L. Hughes (2014) investigated the relationship between energy security and the diversity of energy flows in the power system using a set of energy security indicators and the Shannon-Wiener diversity index but did not propose an algorithm and program to solve the problem of addressing flows and power losses in multi-node regional power systems. T. Kulko *et al.* (2017), V. Bodunov *et al.* (2018), and A.F. Zharkin *et al.* (2021) solved a topological problem with variable parameters in the form of a Pareto-optimal region but did not consider the possibility of the presence of a closed mode of operation of the electric power system in the structure.

G. Fotis *et al.* (2023) conducted a similar analysis, which pointed to the possibility of a large-scale blackout in a country of the United European electricity transmission system or, even worse, a blackout in a large area of the European continent, especially given the energy crisis due to the war in Ukraine in the winter of 2022-2023. The authors also investigated how to avoid such a situation and compiled a list of reactions of the system operator in the event of a blackout. In contrast to the proposed approach, a fast and reliable restoration strategy based on the A* algorithm is used, and the effectiveness of the proposed solutions was tested using the classic IEEE-39 and IEEE-68 circuits.

The study of H. Bila *et al.* (2022) describes mathematical programming problems and numerical methods for solving them using NEOS Server based on various solvers, which are further used to solve linear Boolean programming problems for the well-known m-travelling salesman problem and a multi-extreme nonlinear programming problem. The Gurobi solver is available on the NEOS Server and the AMPL modelling language is used for computations.

A.V. Prakhovnik *et al.* (2010) analysed the national power system of Ukraine and pointed out the inefficient generation and distribution infrastructure and proposed a radically new approach to developing a strategy for meeting the demand for dispatchable electricity production, namely traditional centralised generation, decentralised and alternative energy sources, as well as the use of so-called manoeuvrable loads, such as electric heating systems. The authors used game theory and elements of fuzzy set theory as mathematical methods to solve the problem, taking into account the uncertainty of information and the multi-criteria nature of the problem, but it should be noted that this approach is suitable for solving problems of optimising the structure and increasing the efficiency of electricity supply under normal operation of the electricity system and allows finding solutions for situations of rapid emergency changes in the mode parameters to a limited extent.

Based on the material of E. Rosales-Asensio *et al*. (2022) proposed a new approach to power system resilience, which consists in describing and implementing operating modes in the form of transactional power systems, which aim to increase resilience to disasters and failures, while at the same time making it possible to supply electricity to the largest number of consumers. The authors pointed out that when analysing the power system structure for resilience, it is necessary to consider the needs of its critical users (such as control centres, fire stations and hospitals). To assess the resilience of the power system, they introduced "bonus points" for those systems that should continue to provide electricity to their critical users under any circumstances and assessed the resilience indicators taking into account these innovations, but it should be noted that the introduction of the so-called "bonus points" can significantly distort the operation of a particular power system and requires high expertise of the specialists responsible for their distribution.

A. Van Deventer *et al.* (2010) presented an analysis of cost-effective dispatching of emergency reserves with a particular focus on matching supply and demand. The demand is proposed to be balanced by the electricity market and the supply by the use of open-cycle gas turbines. As the reserve stock decreases and demand increases annually, this problem is growing. Reserves are designed to meet failures in the power system to ensure normal frequency. The categories of reserve according to auxiliary requirements are instantaneous, regulatory, ten-minute, additional and emergency, but the article pays little attention to the formation of the optimal structure of the power system according to the minimum cost criterion.

The study of B. Zhang *et al.* (2018) proposed an integrated intelligent monitoring platform for the operation of a dispatch service centre with a cloud server as the brain and land, sea, aviation and thematic services as the end services. In the context of the study, the Internet of Things technology, wireless sensor network technology and radio frequency technology are applied to realise the interaction between devices to complete automatic data collection and automatic remote transmission. The service centre based on cloud computing performs intelligent control, decision-making and tasks such as scheduling, distribution, data processing, data publishing and platform authorisation, which the research on this platform will provide some suggestions for future intelligent monitoring, but it is not indicated how monitoring of parts of the system will ensure the integrity of the power system structure in an emergency and optimise energy flows.

X. Zhou *et al.* (2015), the authors investigated the indicators of quantifying the risk of the emergency reserve allocation scheme and proposed a coordination method for allocating emergency reserves in the power grid, which considers the cost-benefit ratio. The proposed method first analyses the impact of factors such as regional cost-benefit ratio, probability of an outage and cost of reserve on the allocation of emergency reserve in the power grid, as well as the risks caused by the allocation of emergency reserve and insufficient reserve. The effectiveness and feasibility of the proposed allocation method are tested using the standard IEEE 118 scheme, and it should be noted that the proposed mechanism should be used in the normal operation of the power structure since in a critical state it is desirable to allocate the available reserves to eliminate a possible situation of loss of power system stability.

The proposed method of finding optimal points of power flow distribution for normal and limited modes and its implementation for typical cases of power supply of energy islands proves that this approach can be used as an additional tool of the decision-making system in the operational dispatch control of regional power systems.

CONCLUSIONS

The system of operational dispatch control in the face of unforeseen damage to the energy infrastructure requires

a long time to develop adequate responses and scenarios to ensure the resilience of regional power systems. This imposes significant limitations on the development of timely management decisions by central and regional dispatching systems.

A mathematical model of optimisation based on mixed Boolean linear programming is proposed according to the criterion of minimising the power momentum, considering balance constraints and upper limits of the power of supply nodes and loads. The possibilities of solving the optimisation problem using the Gurobi solver available on the NEOS server are investigated using examples. The levels of efficiency of the Boolean linear programming model are established following the selected characteristic cycles of the transport problem under the specified restrictions on the components of the network structure.

Given the same cross-sections, the optimal values of the objective function may be achieved with different distributions of flows through the cross-sections of the network wires. As a rule, this will occur in cases where there is no balance between the energy flows from supply and load nodes. In this case, it will be necessary to modify the mathematical model by considering the proportional distribution of capacities in the energy island network according to the criterion of minimising losses from power outages for the relevant categories of consumers.

This model does not consider the idle mode for a particular section of the network (setting the correct minimum flow on a branch). This can be considered in the further improvement of the software implementation of the model by introducing restrictions that guarantee non-zero lower limits of power flow, considering the network capacity.

An important area for further research is the adaptation of the described transport problem to analyse the total flows in the oriented edges of the graph and to control the addressability of flow distribution between any nodes of the upper (backbone) and lower levels.

ACKNOWLEDGEMENTS

The authors would like to thank the Volkswagen Foundation (grant No. 97775).

CONFLICT OF INTEREST

The authors declare no conflict of interest.

REFERENCES

[1] Bila, H., Korchynskyy, O., Stetsyuk, P., Khomiak, O., & Shekhovtsov, S. (2022) Using the NEOS server for solving two classes of optimization problems. *Cybernetics and Computer Technologies*, 4, 56-81. doi: 10.34229/2707-451X.22.4.5.

[2] Bodunov, V., Kulko, T., Prystupa, A., & Gai, A. (2018). Topological task of distributed generation placement using a pareto optimization. In *2018 IEEE 3rd International Conference on Intelligent Energy and Power Systems (IEPS)* (pp. 183-188). Kharkiv: IEEE. doi: 10.1109/IEPS.2018.8559502.

[3] Bruno, S., Giannoccaro, G., Iurlaro, C., Scala, M.L., & Menga, M. (2022). Predictive optimal dispatch for islanded distribution grids considering operating reserve constraints. In *2022 IEEE 21st Mediterranean Electrotechnical Conference (MELECON)* (pp. 518-523). Palermo: IEEE. doi: 10.1109/MELECON53508.2022.9842967.

[4] Cai, T., Zhao, C., & Xu Q. (2012). Energy network dispatch optimization under emergency of local energy shortage. *Energy*, 42(1), 132-145. doi: 10.1016/j.energy.2012.04.001.

[5] Fotis, G., Vita, V., & Maris, T.I. (2023). Risks in the european transmission system and a novel restoration strategy for a power system after a major blackout. *Applied Sciences*, 13(1), article number 83. doi: 10.3390/app13010083.

[6] Fourer, R., Gay, D., & Kernighan, B. (2003). *AMPL, A modeling language for mathematical programming*. Belmont: Duxburry Press.

[7] Gurobi optimization. Gurobi optimizer reference manual. (n.d.). Retrieved from http://www.gurobi.com.

[8] Hosseinnezhad, V., Rafiee, M., Ahmadian, M., & Siano, P. (2018). Optimal island partitioning of smart distribution systems to improve system restoration under emergency conditions. *International Journal of Electrical Power and Energy Systems*, 97, 155-164. doi: 10.1016/j.ijepes.2017.11.003.

[9] Izvoshchikova, A. In Ukraine, about 50% of the critical energy infrastructure was damaged – Kubrakov. (2022). Retrieved from https://suspilne.media/335756-v-ukraini-poskodzeno-blizko-50-kriticnoi-energoinfrastrukturi-kubrakov/.

[10] Jiang, Y., Li, L., & Liu, Z. (2018). A multi-objective robust optimization design for grid emergency goods distribution under mixed uncertainty. *IEEE Access*, 6, 61117-61129. doi: 10.1109/ACCESS.2018.2875786.

[11] Kaplun, V., & Osypenko, V. (2020). Energy efficiency analyses in polygeneration microgrids with renewable sources. In *2020 IEEE 7th International Conference on Energy Smart Systems* (pp. 139-143). Kyiv: IEEE. doi: 10.1109/ESS50319.2020.9160346.

[12] Kulko, T., Bodunov, V., Prystupa, A., & Gai, A. (2017). Placement of distributed generation considering topology. In *2017 IEEE International Young Scientists Forum on Applied Physics and Engineering (YSF)* (pp. 32-35). Lviv: IEEE. doi: 10.1109/YSF.2017.8126587.

[13] Naughton, J., Wang, H., Cantoni, M., & Mancarella, P. (2021). Co-optimizing virtual power plant services under uncertainty: A robust scheduling and receding horizon dispatch approach. *IEEE Transactions on Power Systems*, 36(5), 3960-3972. doi: 10.1109/TPWRS.2021.3062582.

[14] NEOS Server. (n.d.). Retrieved from https://neos-server.org.
[15] Nosova, H. The biggest blackouts in history: What it was like (2022). Retrieved from https://tsn.ua/svit/nayvidomishi-blekauti-v-istoriyi-2222854.html.
[16] Prakhovnik, A.V., Popov, V.A., & Nakhodov, V.F. (2010). Risk and uncertainty assessment in the development of strategy for forming the potential of dispatchable generation in the national power system of Ukraine. *International Journal of Global Energy*, 34(1-4), 132-138. doi: 10.1504/IJGEI.2010.037400.
[17] Rai, R., & Nagasaka, K. (2018). Analysis of ELD and OPF for a large-scale power system under emergencies. *International Journal of Renewable Energy Research*, 8(4), 2257-2265.
[18] Ranjan, A., & Hughes, L. (2014). Energy security and the diversity of energy flows in an energy system. *Energy*, 73, 137-144. doi: 10.1016/j.energy.2014.05.108.
[19] Rosales-Asensio, E., Elejalde, J., Pulido-Alonso, A., & Colmenar-Santos, A. (2022). Resilience framework, methods, and metrics for the prioritization of critical electrical grid customers. *Electronics*, 11(14), article number 2246. doi: 10.3390/electronics11142246.
[20] Shang, H., Lin, H., Li, Z., Zhao, H., Chen, M., Yang, Z., & Wen, F. (2020). Robust optimal scheduling of mobile emergency power sources considering uncertainties. *Dianli Jianshe/Electric Power Construction*, 41(8), 111-119. doi: 10.12204/j.issn.1000-7229.2020.08.013.
[21] Van Deventer, A., Chowdhury, S., Chowdhury, S.P., & Gaunt, C.T. (2010). Management of emergency reserves dispatching in electricity networks. In *2010 International Conference on Power System Technology* (pp. 1-5). Zhejiang: IEEE. doi: 10.1109/POWERCON.2010.5666078.
[22] Xu, J., Zhang, T., Du, Y., Zhang, W., Yang, T., & Qiu, J. (2020). Islanding and dynamic reconfiguration for resilience enhancement of active distribution systems. *Electric Power Systems Research*, 189, article number 106749. doi: 10.1016/j.epsr.2020.106749.
[23] Zhang, B., Tang, K., & Guo, H. (2018). Research on the unmanned intelligent monitoring platform of geographical conditions. *Proceedings of SPIE – the International Society for Optical Engineering*, 2018, article number 10835. doi: 10.1117/12.2503981.
[24] Zharkin, A.F., Novskiy, V.O., Popov, V.A., & Yarmoliuk, O.S. (2021). Improving the efficiency of distribution network control under the conditions of application of distributed sources generation of electrical energy and means of its accumulation. *Technical Electrodynamics*, 3, 37-43. doi: 10.15407/TECHNED2021.03.037.
[25] Zhou, X., Li, W., Tang, J., Wang, Q., Yu, J., & Zhang, C. (2015). Risk quantification based coordinative allocation of emergency reserve. *Dianwang Jishu/Power System Technology*, 39(7), 1927-1932. doi: 10.13335/j.1000-3673.pst.2015.07.025.
[26] Zhu, X., Yang, J., Li, G., Dong, X., & Liu, S. (2020). Optimal dispatching strategy of regional integrated energy system considering virtual energy storage system. *Electric Power Construction*, 41(8), 99-110. doi: 10.12204/j.issn.1000-7229.2020.08.012.

Віктор Володимирович Каплун
Доктор технічних наук, професор
Національний університет біоресурсів і природокористування України
03041, вул. Героїв Оборони, 15, м. Київ, Україна
https://orcid.org/0000-0001-7040-9344
Олександр Валентинович Гай
Кандидат технічних наук, доцент
Національний університет біоресурсів і природокористування України
03041, вул. Героїв Оборони, 15, м. Київ, Україна
https://orcid.org/0000-0001-5460-7260
Петро Іванович Стецюк
Доктор фізико-математичних наук, старший науковий співробітник
Інститут кібернетики імені В.М. Глушкова НАН України
03187, пр. Академіка Глушкова, 40, м. Київ, Україна
https://orcid.org/0000-0003-4036-2543
Андрій Володимирович Івлічев
Провідний інженер-програміст
Інститут кібернетики імені В.М. Глушкова НАН України
03187, пр. Академіка Глушкова, 40, м. Київ, Україна
https://orcid.org/0009-0005-2823-6204

Забезпечення оптимальних сценаріїв диспетчеризації регіональних енергосистем в умовах некерованого дефіциту потужності

Анотація. Станом на 2023 рік важливим є обґрунтування критеріїв оптимальності балансування навантаження територіальних енергоостровів в умовах некерованого дефіциту потужності внаслідок непередбачуваного виходу з ладу (руйнування внаслідок воєнних бомбардувань) енергетичної інфраструктури верхнього (магістрального) рівня. Метою дослідження було обґрунтування підходів щодо забезпечення керованого функціонування регіональних енергосистем за умов дефіциту потужності. В роботі було застосовано теорію та методи математичного аналізу складних багатокомпонентних систем у формі змішаного булевого лінійного програмування. Для опису режимів роботи електромереж було використано мову моделювання A Mathematical Programming Language та методи моделювання NEOS-сервера на базі солвера Gurobi. В досліджені застосовано метод пропорційного розподілу потужності між вузлами навантаження післяаварійної конфігурації мережі для визначення напряму транзиту електроенергії з найменшими втратами. Запропоновано алгоритм і програму для розв'язування задачі адресності потоків і втрат потужності у багатовузлових регіональних енергосистемах. Сформульована задача оптимізації у формі моделі змішаного булевого лінійного програмування з критерієм мінімізації моменту потужності при врахуванні балансових обмежень та верхніх границь на потужності між вузлами постачання та навантажень. Розроблена транспортна матриця дозволила знаходити оптимальний розподіл потужності для аварійних та післяаварійних режимів за критерієм мінімальних мережевих втрат. Сформовано алгоритми та сценарії реагування диспетчерських служб з урахуванням пропускної здатності електричних мереж та визначення тимчасових схем електропостачання, конфігурація яких дозволить забезпечити «живучість» енергоостровів. Встановлено рівні ефективності моделі булевого лінійного програмування, пов'язаних зі зв'язністю циклів транспортної задачі та порядком обходу його вершин для тестових прикладів в залежності від обмежень, які накладаються на компоненти структури мережі. Процес відстеження потоків електроенергії дозволить встановлювати маршрути, які зв'язують конкретні вузли постачання електроенергії з вузлами навантаження, і визначати їх частки у покритті попиту енергоострова за умов дефіциту потужності

Ключові слова: критерій мінімізації моменту; енергоострів; транспортна матриця; булеве лінійне програмування; балансування навантаження

Machinery & Energetics
Vol. 14, No. 2. 2023

Journal homepage:
https://technicalscience.com.ua/en

UDC 621.316.729:621.396.6
DOI: 10.31548/machinery/2.2023.34

Larysa Nykyforova*
Doctor of Technical Sciences, Professor
National University of Life and Environmental Sciences of Ukraine
03041, 15 Heroiv Oborony, Kyiv, Ukraine
https://orcid.org/0000-0001-6913-1672

Nikolay Kiktev
PhD in Technical Sciences, Associate Professor
National University of Life and Environmental Sciences of Ukraine
03041, 15 Heroiv Oborony, Kyiv, Ukraine
https://orcid.org/0000-0001-7682-280X

Taras Lendiel
PhD in Technical Sciences, Associate Professor
National University of Life and Environmental Sciences of Ukraine
03041, 15 Heroiv Oborony, Kyiv, Ukraine
https://orcid.org/0000-0002-6356-1230

Sergey Pavlov
Doctor of Technical Sciences, Professor
Vinnytsia National Technical University
21021, 95 Khmelnytsky Highway, Vinnytsia, Ukraine
https://orcid.org/0000-0002-0051-5560

Pavel Mazurchuk
Postgraduate Student
National University of Life and Environmental Sciences of Ukraine
03041, 15 Heroiv Oborony, Kyiv, Ukraine
https://orcid.org/0009-0000-0064-8999

Computer-integrated control system for electrophysical methods of increasing plant productivity

Abstract. Due to the growing demand for agricultural products, there is a need to intensify the process of growing plants and reduce their diseases. Therefore, the technical implementation of methods for controlling the functional activity of plants using electromagnetic radiation at different stages of organogenesis and their automation is an urgent task. The research aims to increase the efficiency of plant cultivation by studying electrophysical methods of controlling their productivity and implementing a computer-integrated system. To achieve this goal, a mathematical corrective model of the interaction of laser radiation with solid biological tissue, algorithms for measuring and generating control effects, methods of automatic control theory, and visual programming in LabView were used. The data were processed in MS Excel. The connections in the biotechnical plant-environment system were analysed, material flows and information channels were identified, a set of state parameters, and direct and cross relationships between them were singled out,

Article's History: Received: 08/02/2023; Revised: 02/04/2023; Accepted: 26/04/2023.

Suggested Citation:
Nykyforova, L., Kiktev, N., Lendiel, T., Pavlov, S., & Mazurchuk, P. (2023). Computer-integrated control system for electrophysical methods of increasing plant productivity. *Machinery & Energetics,* 14(2), 34-45. doi: 10.31548/machinery/2.2023.34.

*Corresponding author

and sources of disturbances were argued. The basic principles of the interaction of laser radiation with biological tissue are determined and the biophysical mechanism is substantiated. A set of software and hardware control and management tools for conducting experimental studies of electrophysical effects on plant biological objects has been developed. To obtain feedback from plants, new tools for diagnosing the physiological state of plant organisms were developed and a computer-integrated system for controlling the process of plant irradiation was created. The control system is based on the Arduino microcontroller software and is connected to a PC. An operator panel was created to provide automated process control and a subsystem for recording measured data. In practice, the results of this study can be applied in greenhouses in Ukraine and other countries, including in the cultivation of vegetable crops

Keywords: seed treatment; biotechnical system; laboratory setup; platform, algorithm; automation; integrated circuit board

INTRODUCTION

A decline in the profitability of greenhouses, their environmental friendliness, and the reduction of the area of covered ground is being observed in Ukraine. This problem is both food and environmental, so there is a need to develop high-yielding plant varieties. This requires many years of breeding and agronomic work on farms (Trachyova, 2006). To solve this problem, it is necessary to develop automated control systems for biotechnical objects, in which the plant will be the source of information. The information received from the plant will be transformed into a source for selecting optimal control actions. A biological object in the form of a plant is a complex cybernetic system. It is characterised by the ability to change both the tactics and the optimal management strategy to adapt it to the environment.

Adjustment of plant life processes is made possible by changing the spatial and spectral distribution of external electromagnetic radiation. Various methods, including optical ones, can provide this, as they allow to determine the quantitative and qualitative indicators of biological objects with a certain accuracy.

Many researchers in Ukraine and abroad have conducted experiments on microclimate control for growing plants in greenhouses and phytotrons. Experiments with maintaining the microclimate during plant cultivation are carried out using a phytotron, for example, as described by Taiwanese researchers Y.C. Chu & J.C. Chang (2020) and Algerian scientists H.E. Adjerid *et al.* A. Ouammi *et al.* (2020) presents an integrated energy management system for an intelligent greenhouse based on a microgrid, which allows to ensure optimal parameters of the internal environment during crop growth. The management of greenhouse parameters based on the Internet of Things (IoT) is presented in the article by Turkish researchers M.A. Akkas & R. Sokullu (2017). Scientists are creating a personal phytotron at an affordable price thanks to a wide range of equipment, cloud computing and new opportunities offered by the IoT (Internet of Things). R.A. Abdelouhahid *et al.* (2020) investigated that temperature, relative humidity and lighting as environmental parameters represented the growing regimes of seedlings or plants in different developmental stages tested in phytotron chambers. To evaluate the impact of technological parameters on plants, phytotrons with various electronic control systems are also created to develop new varieties. The article by A.A. Vetchinnikov *et al.* (2021) assesses the impact of different spectra of LED lights on the growth and development of vegetable crops in greenhouses. It is substantiated that LED lamps of different spectra affect the nutritional value of plants.

A. Cherenkov *et al.* (2018) used an electromagnetic pulse method to kill insect pests in gardens. L. Nykyforova (2019) presented the processes in plant production as a biotechnical system, as well as the electrical circuit of a device for measuring the bioelectrical potential of a plant.

The research aims to investigate electrophysical methods of plant productivity control as a biotechnical system, to develop and experimentally test a computer-integrated plant productivity control system.

The following goals were set: analyse the coupling in the biotechnical plant-environment system; create an algorithm for remote temperature measurement; perform the technical implementation of a plant productivity management system based on the Arduino board and the LabView software environment.

MATERIALS AND METHODS

The study used a mathematical correction model for the interaction of laser radiation with solid biological tissue (Cherenkov *et al.*, 2018; Nykyforova, 2019).

When it is necessary to describe the process of high-energy laser radiation affecting solid biological tissue, it is necessary to consider the processes of temperature distribution. The evaporation of biological tissue occurs at a temperature of more than 300°C. Therefore, the amount of heat that enters the area of biological tissue must heat it to a temperature greater than 300°C. To calculate this process, the general spatiotemporal characteristic of the temperature distribution was used (1):

$$\frac{dT}{dt} = \frac{q}{\rho \cdot c} + \frac{l \cdot \nabla^2 \cdot T_1}{\rho \cdot c}, \quad (1)$$

where q – heat amount; l – biological tissue heat conductivity; T_1 – initial biological tissue temperature; ρ – biological tissue density; c – thermal conductivity of biological tissue.

The amount of heat transferred to the biological tissue depends on the pulse power of the laser radiation, generation frequency, beam diameter, and absorption coefficient.

If the temperature of the biological tissue at the end of the previous pulse is not considered, it can be assumed that the time interval between pulses will be equal to the relaxation time of the biological tissue. The relaxation will be small due to the small diameter of the laser spot (2):

$$q = \frac{W_{im} \cdot (t_{im} + t_{rbl})}{t_{im}} - \frac{\pi \cdot d^2}{4} - \mu_\alpha, \quad (2)$$

where t_{im} – impulse length; t_{rbl} – relax time; μ_α – weight absorption coefficient of biological tissue (3):

$$\mu_\alpha = \frac{4 \cdot \rho \cdot R \cdot \mu_\tau}{\lambda \cdot d}. \quad (3)$$

Furthermore, refractive values, and transmittance μ_τ are constants for these biological tissues.

The Lambert-Behr relationship is valid when the absorption of light is significantly greater than its scattering. The mechanism of light absorption depends on the concentration of the absorbing molecules, and the absorption values at the cellular and subcellular levels can vary significantly for different molecules. In addition, the absorption coefficient can vary for lasers operating in different spectral ranges since absorption is a wavelength-dependent function.

Light in the range of 600 to 1200 nm penetrates biological tissue more deeply with minimal effects on absorption and scattering. In this range, the radiation can reach deep molecular layers. Laser devices, such as argon, dye, and IAG (aluminium yttrium garnet): Nd-laser (both conventional and frequency-doubling) have a strong effect on haemoglobin, melanin, and other organic substances, and can have a coagulation effect. The parameters of biological tissue (thermal conductivity and specific thermal conductivity) are functions of water content, so (4):

$$l = \left(0{,}06 + 0{,}57 \cdot \frac{\omega}{\rho}\right), c = \left(1{,}55 + 0{,}28 \cdot \frac{\omega}{\rho}\right). \quad (4)$$

During the evaporation of biological tissue, a heat damage zone is formed. This fact confirms that the temperature distribution in biological tissues is gradient. The temperature distribution depends on the following parameters (5):

- distance of biological tissue (plant) to the radiation source (r^*),
- hole depth (h),
- Time (dynamic) characterisation of a biological tissue sample (N);
- impulse effect duration (t_{im}).

$$T = \frac{1}{r^*} \cdot exp\left(-\left(\frac{N}{t_{im}}\right)^{\frac{1}{2}} - \frac{1}{h}\right), N = \frac{l}{\rho \cdot c}, \quad (5)$$

Considering the above parameters that affect the modelling of the process, the following equation for the dependence of the depth of the hole is derived (h) from the laser radiation duration (6):

$$h = \frac{\sqrt{\frac{l}{\rho \cdot c \cdot t_{im}}}}{ln\frac{\frac{W_{im} \cdot \left(t_{im} + \frac{d^2 \cdot \rho \cdot c}{l}\right) - \pi \cdot d^2 \cdot r^* - N}{4 \cdot t_{im}} + l \cdot N^2 \cdot T_1 \cdot r^*}{\rho \cdot c \cdot t}}. \quad (6)$$

This mathematical model is best suited to describe the process of lithotripsy when biological tissue is ablated. It allows to find the depth of the hole created by the laser beam. The formula for determining the depth of the hole (the thickness of the removed biological layer) can be replaced by a simpler one that gives close values (7):

$$L = \frac{\left(ln\left(\alpha \cdot \frac{E}{E_V}\right)\right)}{\mu_\alpha}, \quad (7)$$

where E – impulse energy; E_V – volume density of absorbed energy; μ_α – absorption coefficient.

The mass of solid biological tissue material removed by ablation was determined by the average value of the volume of the cavity formed under the action of radiation pulses multiplied by the density of the biological tissue. The productivity of the destruction of solid biological tissue is the ratio of the removed mass of biological tissue to the pulse energy. Technical requirements were established and a prototype of a device for seed treatment using a low-intensity non-monochromatic field was used. To perform physiological measurements of seed treatment with a low-energy non-monochromatic field, the following technical equipment was used according to the developed methodology: a prototype of a device for seed treatment with a low-intensity non-monochromatic field (LIK-30A (laser research complex), manufactured in Russia) and a device for rapid diagnosis of biological objects (Prima-2005M, manufactured in Ukraine), which together form a unified optoelectronic technical system for research and rapid diagnosis of plant health.

Figure 1 shows a schematic diagram of a prototype of a laboratory setup for seed treatment using a low-energy non-monochromatic field.

The computer-integrated monitoring and control system is based on the Arduino Mega2560 hardware (Italy), which is based on the ATmega2560 microcontroller (Fig. 2).

The platform was configured to be powered with a voltage of 5-12 V. The chip receives a stabilising voltage for the microcontroller and sensors. This controller cannot communicate with a computer via the USB port. You can

also power the controller through the port. Arduino operates at a frequency of 16 MHz with 54 digital I/O channels, 16 analogue inputs, 14 of which can be used in PWM (pulse width modulation) mode, 4 hardware serial ports UART, which are designed to communicate with a personal computer and other devices connected to a computer-integrated system. In case of an incorrect request, the "Reset" button can be used.

The software implementation of the described system was performed in the LabVIEW environment. The program is executed using a block diagram, and data processing and graphing are performed in MS Excel.

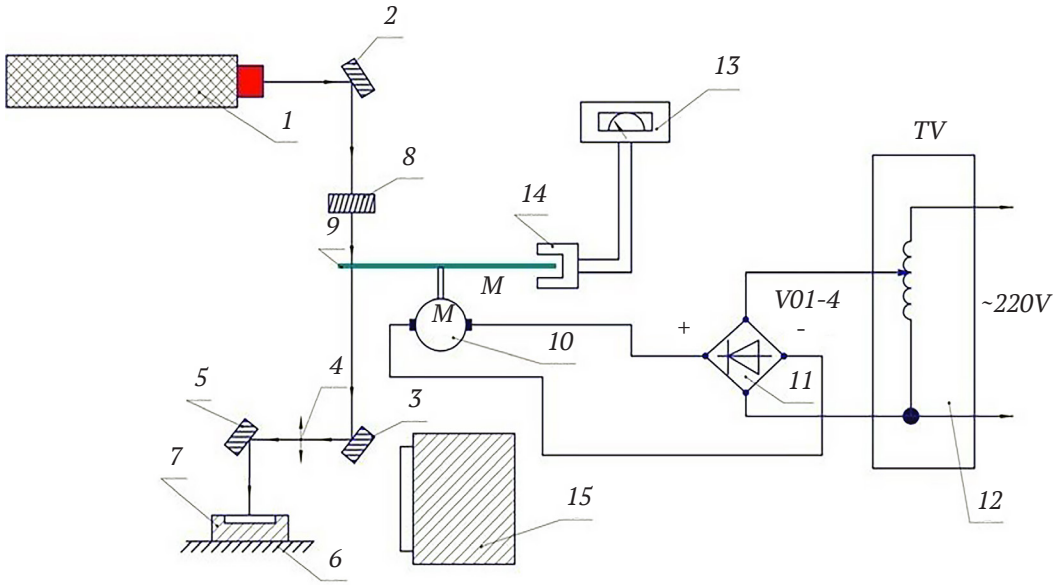

Figure 1. Diagram of a laboratory setup for seed treatment

Note: 1 – laser, 2, 3, 5 – mirror, 4 – lens, 6 – slide, 7 – petri dish with seeds, 8 – light filter, 9 – opaque disc with slots, 10 – electric motor, 11 – rectifier bridge, 12 – autotransformer, 13 – pulse counter/tachometer with sensor, 14, 15 – device for measuring energy density

Source: R.V. Vasilishin (2005)

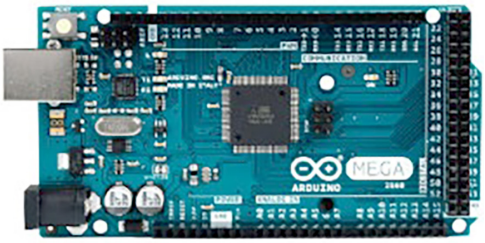

Figure 2. Arduino Mega2560

RESULTS AND DISCUSSION

When analysing the plant-environment biotechnical system, material and information channels were identified, a set of input and output state parameters, as well as the nature of direct and cross-correlation, were determined, and sources of external disturbances were identified. Figure 3 shows a parametric model of a plant biosystem. The most important material and information flows that need to be monitored and analysed are highlighted (Cherenkov *et al.*, 2018, Nykyforova, 2019). These are the solar radiation inflow E, heat inflow Q, water inflowW, carbon dioxide inflow, and mineral elements C.

The following factors also affect the plant in Figure 3: T_n, T_b, Ψ_n, Ψ_b – temperature and humidity, respectively, of the outside air and the plant, C – nitrogen concentration (NO_3), methane (NH_4), calcium K, calcium Ca, phosphate (PO4), f(t) – the impact of external disturbances.

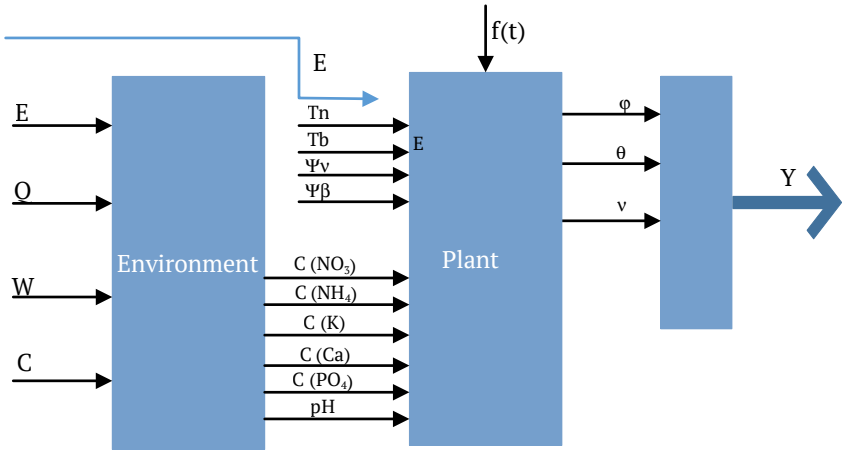

Figure 3. Structural and functional model of a plant biosystem
Note: T_n, T_b, Ψ_n, Ψ_b – temperature and humidity, respectively, of the outside air and the plant, C – nitrogen concentration (NO_3), methane (NH4), calcium K, calcium Ca, phosphate (PO4), f(t) – the impact of external disturbances
Source: A. Cherenkov *et al*. (2018), L. Nykyforova (2019)

These technical requirements make it possible to identify a set of plant condition parameters that will include:

- turgor (i.e. water) potential ν, %;
- bioelectric field potential φ, MW;
- thermodynamic potential θ, °C.

These physical quantities need to be measured in real-time to ensure that the plant's condition is monitored.

Y – is an integrated indicator of the specified output parameters, which is calculated by the formula (8) (Nykyforova, 2019):

$$Y = C \int_t^{t+T_H} y(t)dt, \quad (8)$$

where $y(t)$ – dynamic values of a set of technical parameters.

Thus, to create automated plant productivity management systems, it is necessary to develop a software and hardware complex for measuring bioelectric potential, which will allow for rapid diagnostics while simultaneously monitoring the dynamic state of plants online.

The absorption of laser radiation leads to the appearance of biochemical, bioelectrical and bioenergetic effects in biological tissue. The flowchart in Figure 4 demonstrates the biophysical effects that occur after the absorption of laser radiation, both low and medium power. These effects occur at low power densities and relatively long exposure times.

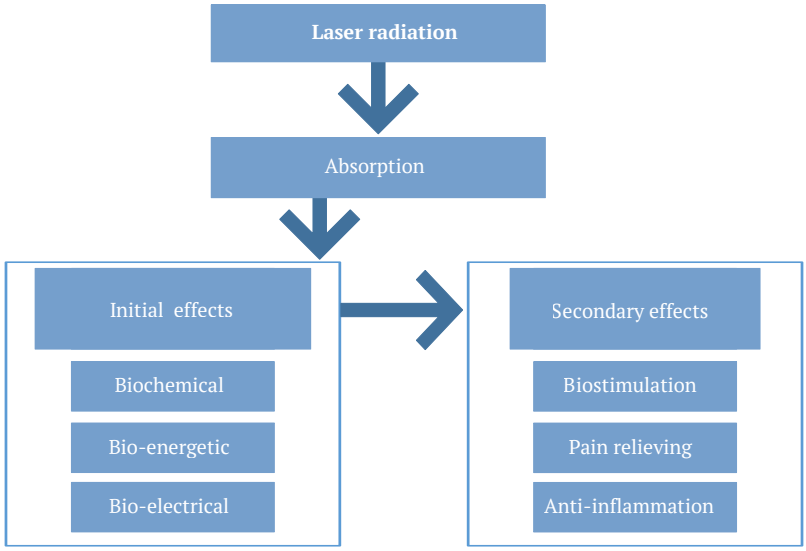

Figure 4. Simplified diagram of the reaction of biological tissue to low or medium-power laser light
Source: compiled by the authors

The photons of the laser source capture a selection in the biological tissue, regardless of the time of illumination of the selected point. In Figure 5, the arrows indicate the amount of energy incident on the biological tissue.

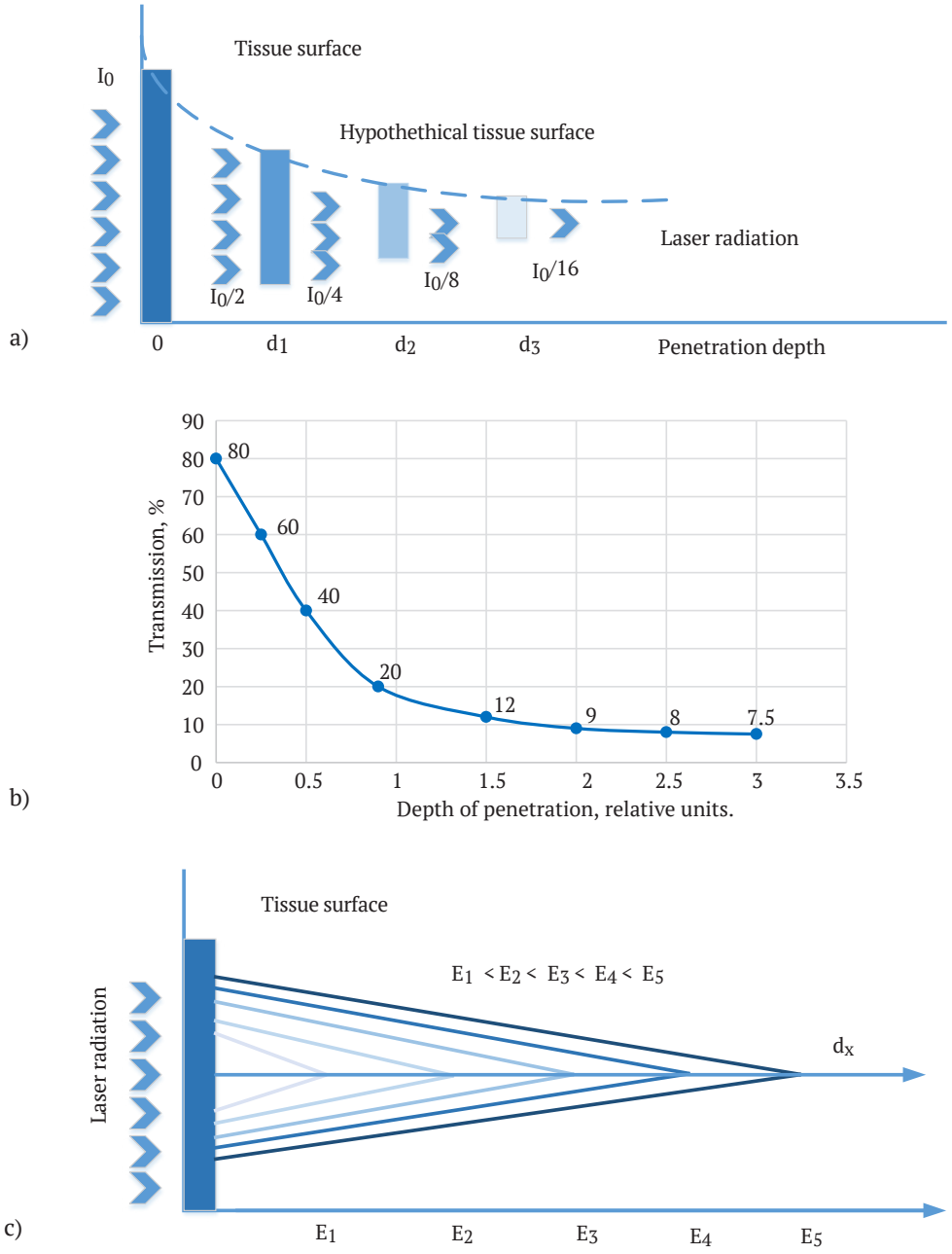

Figure 5. Illustration of the processes of laser radiation penetration into biological tissue
Note: d_1, d_2, d_3... – penetration depth, I0 – laser radiation index, which decreases multiply upon penetration into the plant, E_1-E_5 – types of laser wave energy, d_x – energy value
Source: compiled by the authors

Penetration into such layers of biological tissue is associated with a decrease in energy. The half penetration depth is the depth of the biological tissue layer that accounts for 50% of the initial energy (Fig. 5a). At the same time, the skin transmits about 80% of the incoming light energy of the tissue (Fig. 5b) when the rays are transversely incident on the tissue. The dependence on the intensity of laser wave penetration with different types of energy is shown in a schematic graph in Figure 5c. In general, Figure 5 is a "single photon" instruction. According to this theory, a single photon located in biological tissue is sufficient to achieve a bioenergy process.

Figure 6 shows a comparison of the depth of penetration of laser radiation in experiments related to biology and medicine. The algorithm of the control system is shown in Figure 7.

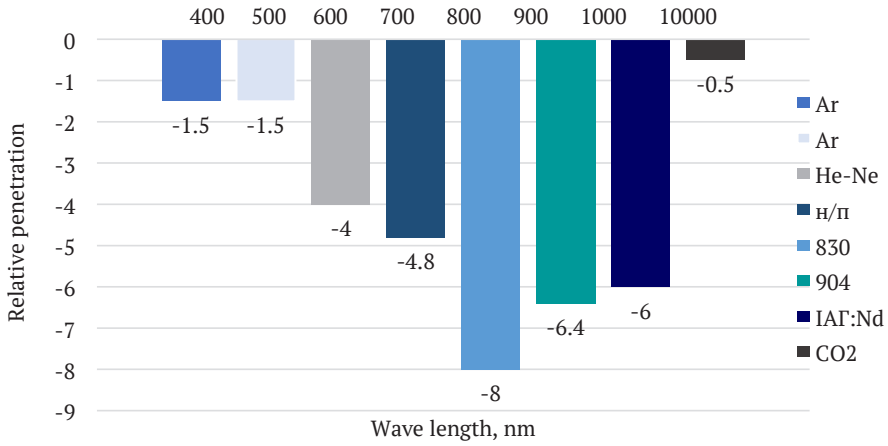

Figure 6. Dependence of the depth of relative penetration of lasers on the wavelength of radiation
Source: compiled by the authors

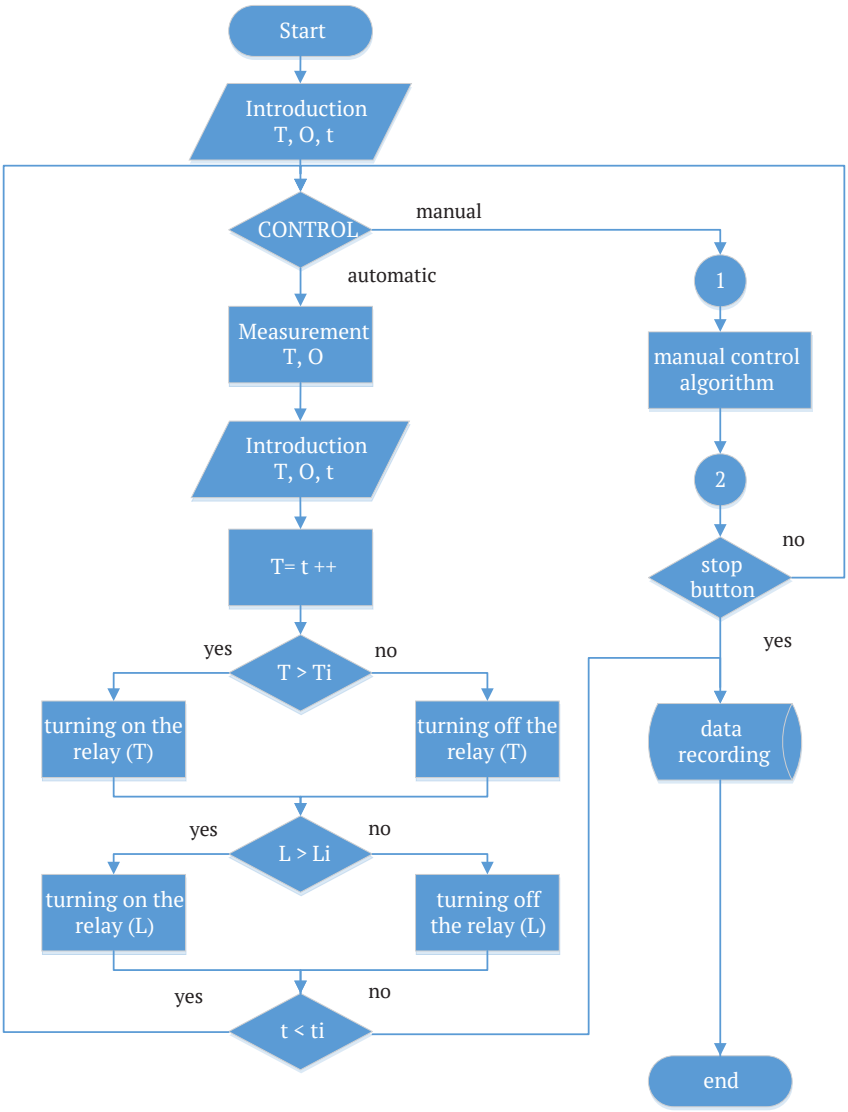

Figure 7. Algorithm for remote temperature measurement (T)
Source: compiled by the authors

The system works as follows:

1) after the power supply is presented, the entire system is initialised, and the critical time value t_k is entered; 2) the effective time value t is compared with the critical time value t_k (the time during which the entire technological process takes place); 3) measurement of process parameters; 4) check the wireless connection, assign an IP address; 5) when connected wirelessly, the measured value is displayed; 6) expectations of the team; go to point 2; 7) in the absence of wireless communication, the system switches to automatic mode; 8) after the control action is transmitted to the actuators, the data is transmitted to the personal computer of the general control system; go to paragraph 2.; 9) when the critical time is reached, the programme is terminated.

One of the most important features of the ESP8266 (Espressif Systems, China) is that it cannot only connect to an existing Wi-Fi network and act as a web server, but it can also set up its network, allowing other devices to directly connect to it and access web pages. This is possible because the ESP8266 can operate in three different modes: station mode, access point mode, and both of the first two modes simultaneously. Figure 8 details the formation of control actions – switching on the relay.

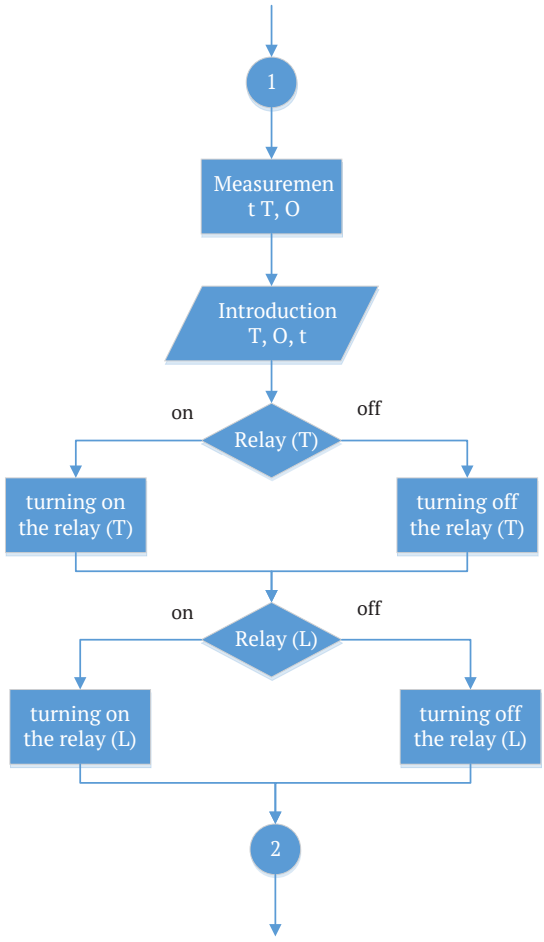

Figure 8. Subroutine for generating control influences

Source: compiled by the authors

Algorithm description.

After the system is initialised, the initial values are entered. Next, select the control mode: automatic or manual. When selecting automatic control, the operation timer (t) is first activated. The control system then measures the process parameters and compares the measured value with the setpoint. After each comparison, the drive relay is switched on or off (relay T, relay L). In the automatic mode, the system timer time is increased by one step after each operation. The automatic mode is executed until the set control time ($t>t_i$) is reached.

In the manual control mode, the process parameters are measured, and when the operator presses the control buttons, the actuator relays (relay T, relay L) are switched on or off. Measurements are recorded in both modes.

A graphical representation of the application system interface is shown in Figure 9.

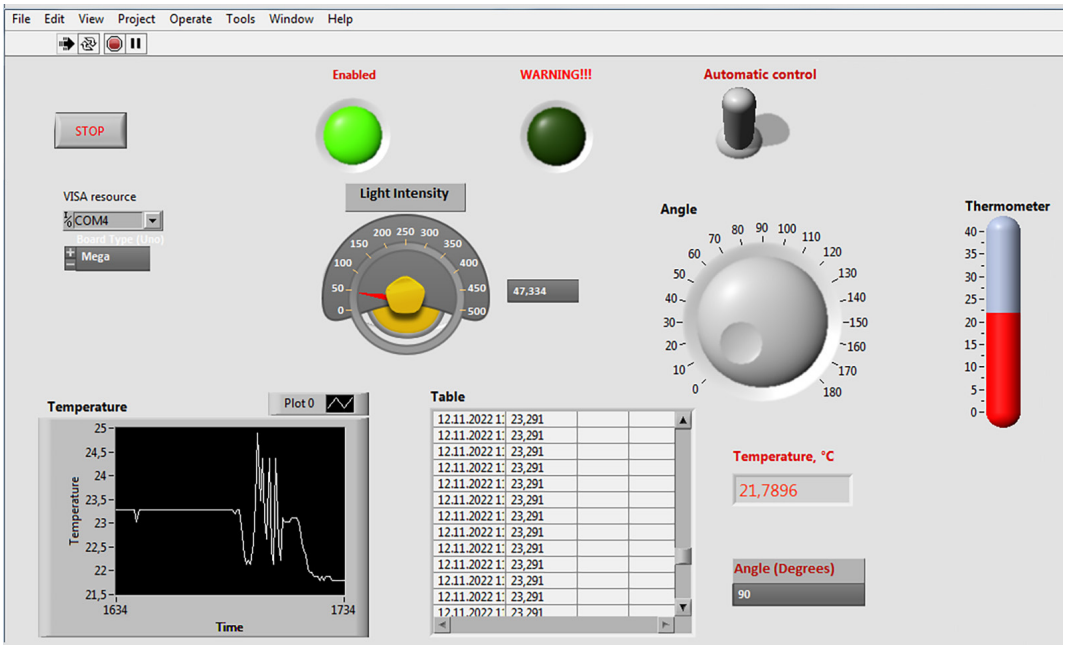

Figure 9. Operator's window

Source: compiled by the authors

The software for this system is implemented in the LabVIEW environment, and the reading of information from the sensors is also decomposed in the operator interface. In addition, the recorded values were transferred to the database for further statistical analysis – building correlation relationships, forecasting, clustering, etc. The data is stored in memory in the form of a table that is unified with data processing programs, the main part of which is Microsoft Office Excel.

Many scientists have also studied the problems of increasing the efficiency of growing seeds and plants by influencing them. A.Y. Cherenkov *et al.* (2018), and I.G. Smirnov *et al.* (2019) considered the treatment of seeds with a magnetic pulse field. The authors conducted experiments to study the effect of a low frequency pulsed magnetic field on seed germination and growth of garden strawberry seedlings. For this purpose, an installation for magnetic pulse treatment of plants in the form of a low frequency pulsed magnetic field emitter was developed. The use of this device made it possible to stimulate the processes of vital activity and growth of garden plants, vegetables, and crops. During the experiment, different treatment conditions were established with a periodic sequence of magnetic induction pulses in the low-frequency range with simultaneous irradiation with light pulses of certain wavelengths of the optical range. It was found that the germination energy of seeds treated with a pulsed magnetic field ranged from 29 to 47%, and the germination rate from 34 to 48%. The analysis of the data from the factorial experiments showed that the most effective irradiation parameter for increasing germination and germination energy of seeds is irradiation with a frequency of 15.325 Hz, a band gap of 16.145 and magnetic induction in the irradiation zone of 5.05 mT.

The control of plant functional activity by coherent light was described by J. Chávez *et al.* (2018). In particular, the methodology, analytical equipment, and technical means for studying the interaction of coherent light with biological systems and structures were developed, and a block-modular principle for designing laser installations and diagnostic devices for crop production was proposed and developed. The study presents experiments on the irradiation of both seeds and ripened fruits. Multifunctional installations of the LIC series (laser research complex) and production installations of the LOS series (agricultural laser irradiator) were used in the studies.

The LIK-30A complex (laser research complex) can be used as an irradiation device, which allows for solving a wide range of research tasks, including irradiation of biological objects according to a given programme. The LIK-30A control system (Russia) provides automatic irradiation of one or two biological objects in the mode of single or multiple periodic exposures to optical radiation with specified parameters. The control block diagram is given by J. Chávez *et al.* (2018) and includes three blocks connected by electrical signals: BUCF (control and operation unit), BOS (object feedback unit) and BFPI (radiation flux formation unit).

The most modern device for laser irradiation is Lika-Led (PE "Photonika-plus", Cherkasy, Ukraine). Development and implementation of a system for phytomonitoring of technological parameters of cultivation in a phytotron and the possibility of remote switching of connected devices of the electrical complex.

Optimisation of energy costs for growing vegetables in greenhouses is presented by Canadian researchers M.C. Bozchalui *et al.* (2015). The developed monitoring

system based on a wireless sensor network for a greenhouse using solar energy is described in the article by Chinese researchers J. Hou & Y. Gao (2010). An energy-efficient greenhouse based on renewable energy sources is presented in the article by Romanian researchers R. Grigoriu *et al.* (2015).

Similar computer-integrated systems have been implemented by the authors for a phytotron (Lendiel *et al.*, 2021), a feed store and a livestock building (Kiktev *et al.*, 2021). In recent years, there have been publications on studies of laser effects on plants and seeds. Scientists from Saudi Arabia, Egypt, and Belgium, M.K. Okla *et al.* (2021) described the effect of laser-irradiation on lemongrass seedlings, namely on improving biomass photosynthesis, chemical composition, and biological activity. The authors found that laser light improved photosynthetic activity, respiration and, consequently, the seedlings' fresh weight. Polish researchers A. Klimek-Kopyra *et al.* (2020), J. Dłużniewska *et al.* (2021) evaluated the productivity and health of soybean plants as a result of coherent seed irradiation together with irradiation of a fungal inoculum, which showed a decrease in the incidence of diseases in this crop. The authors determined the best wavelength for laser irradiation, which was 514 and 632.8 nm.

A system for controlling plant germination performance based on a plant for laser irradiation of corn seeds using a time relay is presented by Malaysian and Iraqi authors M. Hasan *et al.* (2020). The authors have established the best wavelengths and optimal time for irradiating the seeds of a given crop.

Compared to the studies conducted by scientists around the world on increasing plant productivity, it can be noted that this study combines biophysical research with modern algorithms and technical means of automation, i.e., an automated process of plant productivity management.

CONCLUSIONS

Based on the results described above, a model for studying plant development was developed and implemented, which links the inflows of solar radiation, heat, water, carbon dioxide and mineral elements with an integral indicator that combines bioelectric, water and thermodynamic potential. A plant productivity management system based on electrophysical methods was designed and investigated. Diagrams of the amount of energy incident on biological tissue, the transmittance of incoming light energy to the tissue when the rays are transversely incident on the tissue, and a graph of the dependence on the intensity of laser wave penetration with different types of energy were constructed. The structure of the laboratory setup and control system was developed, an algorithmic control flowchart was built, and a phytomonitoring system for plant growth parameters was implemented using computer-integrated technologies, namely the Arduino Mega2560 integrated circuit board and the LabView software package. An interface for the graphical display of measured data from temperature, pressure, and humidity sensors and the ability to switch relays to which the devices of the electrical complex are connected was built. The data received from the sensors is transferred to the database in MS Excel for further processing.

In the future, it is planned to develop the project, namely, to use a modern device for laser radiation of different frequencies, LIKA-LED, and to include it in the circuit of the developed computer-integrated system. Studies are also planned to measure the bioelectrical potential of plants, radiation by CWH signals (short high-frequency waves) with a frequency of 39-56 GHz and the effect of radiation on the plant life cycle at different stages of vegetation. Future studies are also planned to analyse the effect of different laser wavelengths on the growth of seeds and seedlings of vegetable crops.

ACKNOWLEDGEMENTS

None.

CONFLICT OF INTEREST

The authors declare no conflict of interest.

REFERENCES

[1] Abdelouhahid, R.A., Debauche, O., Mahmoudi, S., Marzak, A., Manneback, P., & Lebeau, F. (2020). Open phytotron: A new IoT device for home gardening. In *2020 5th International Conference on Cloud Computing and Artificial Intelligence: Technologies and Applications, CloudTech 2020* (pp. 1-8). Marrakesh, Morocco. doi: 10.1109/CloudTech49835.2020.9365892.

[2] Adjerid, H.E., Remram, Y., & Attari, M. (2020). Development of an electronic system for the control of climatic parameters in a phytotron. In *2020 – 1st International Conference on Communications, Control Systems and Signal Processing* (pp. 417-421). El Oued, Algeria. doi: 10.1109/CCSSP49278.2020.9151598.

[3] Akkas, M.A., & Sokullu, R. (2017). An IoT-based greenhouse monitoring system with micaz motes. *Procedia Computer Science*, 113, 603-608. doi: 10.1016/j.procs.2017.08.300.

[4] Bozchalui, M.C., Cañizares, C.A., & Bhattacharya, K. (2015). Optimal energy management of greenhouses in smart grids. *IEEE Transactions on Smart Grid*, 6(2), 827-835. doi: 10.1109/TSG.2014.2372812.

[5] Chávez, J.A.D., Michtchenko, A., & Budagovskii, A.V. (2014). Biostimulation of the growth of wheat seeds produced by modulated pulsed diode lasers radiation. In *2014 11th International Conference on Electrical Engineering, Computing Science and Automatic Control,* (article number 6978305). Ciudad del Carmen: Institute of Electrical and Electronics Engineers Inc.

[6] Cherenkov, A.D., Kosulina, N.G., Yaroslavskyy, Y.I., Titova, N.V., Aizhanova, A., & Tanas, J. (2018). Justification of the electromagnetic impulse method destruction of insect pests in gardens. In *SPIE Proceedings Potonics Applications in Astronomy, Communications, Industry, and High-Energy Physics Experiments*, 10808, article number 108083P. doi: 10.1117/12.2501665.

[7] Chu, Y.C., & Chang, J.C. (2020). Regulation of floral bud development and emergence by ambient temperature under a long-day photoperiod in white-fleshed pitaya (*Hylocereus undatus*). *Scientia Horticulturae*, 271, article number 109479. doi: 10.1016/j.scienta.2020.109479.

[8] Dłużniewska, J., Klimek-Kopyra, A., Czech, T., Dobrowolski, J.W., Dacewicz, E. (2021). The use of coherent laser stimulation of seeds and a fungal inoculum to increase the productivity and health of soybean plants. *Agronomy*, 11, article number 1923. doi: 10.3390/agronomy11101923.

[9] Grigoriu, R., Voda, A., Arghira, N., Calofir, V., & Iliescu, S.S. (2015). Temperature control of a greenhouse heated by renewable energy sources. In *2015 Intl Aegean Conference on Electrical Machines & Power Electronics* (pp. 494-499). Side, Turkey. doi: 10.1109/OPTIM.2015.7427009.

[10] Hasan, M., Hanafiah, M.M., Aeyad Taha, Z., AlHilfy, I.H.H., & Said, M.N.M. (2020). Laser irradiation effects at different wavelengths on phenology and yield components of pretreated maize seed. *Applied Sciences*, 10(3), article number 1189. doi: 10.3390/app10031189.

[11] Hou, J., & Gao, Y. (2010). Greenhouse wireless sensor network monitoring system design based on solar energy. In *2010 International Conference on Challenges in Environmental Science and Computer Engineering* (pp. 475-479). Wuhan, China. doi: 10.1109/CESCE.2010.274.

[12] Izmailov, A.Y., Smirnov, I.G., Khort, D.O., Filippov, R.A., & Kutyrev, A.I. (2018). Magnetic-pulse processing of seeds of berry crops. *Research in Agricultural Engineering*, 64(4), 181-186. doi: 10.17221/9/2018-RAE.

[13] Kiktev, N., Lendiel, T., Vasilenkov, V., Kapralyuk, O., Hutsol, T., Glowacki, S., Kuboń, M., & Kowalczyk, Z. (2021). Automated microclimate regulation in agricultural facilities using the air curtain system. *Sensors*, 21(24), article number 8182. doi: 10.3390/s21248182.

[14] Klimek-Kopyra, A., Dłużniewska, J., Ślizowska, A., & Dobrowolski, J.W. (2020). Impact of coherent laser irradiation on germination and mycoflora of soybean seeds – innovative and prospective seed quality management. *Agriculture,* 10(8), article number 314. doi: 10.3390/agriculture10080314.

[15] Lendiel, T., Kiktev, N., & Pasichnyk, N. (2021). Control system of electrotechnical phytotron complex with the use of internet of things technology. In *VIII International Scientific Conference "Information Technology and Implementation"* (Vol. 3179, pp. 251-261). Kyiv: CEUR.

[16] Nykyforova, L. (2019). Conception of creation of biotechnical in plant-grower. *Energy and Automation*, 4(44), 80-90. doi: 10.31548/energiya2019.04.080.

[17] Okla, M.K., El-Tayeb, M.A., Qahtan, A.A., Abdel-Maksoud, M.A., Elbadawi, Y.B., Alaskary, M.K., Balkhyour, M.A., Hassan, A.H.A., & AbdElgawad, H. (2021). Laser light treatment of seeds for improving the biomass photosynthesis, chemical composition and biological activities of lemongrass sprouts. *Agronomy*, 11(3), article number 478. doi: 10.3390/agronomy11030478.

[18] Ouammi, A., Achour, Y., Dagdougui, H., & Zejli, D. (2020). Optimal operation scheduling for a smart greenhouse integrated microgrid. *Energy for Sustainable Development*, 58, 129-137. doi: 10.1016/j.esd.2020.08.001.

[19] Smirnov, I.G., Khort, D.O., Filippov, R.A., & Kutyrev, A.I. (2019). Factor analysis of irradiation of the strawberries (fragaria × ananassa) seeds pulsed low-frequency magnetic field. *Indian Journal of Agricultural Sciences*, 89(5), 113-118. doi: 10.56093/ijas.v89i5.89672.

[20] Trachyova, D.M. (2006). *Effectiveness of greenhouse vegetables production*. (PhD thesis, NSC "Institute of Agrarian Economics" UAAS, Kyiv, Ukraine)

[21] Vasilishin, R.V. (2005). *Substantiation of technological regimes and parameters of the device for laser pre-sowing irradiation of vegetable seeds* (PhD thesis, Tavria State Agrotechnological University, Melitopol, Ukraine).

[22] Vetchinnikov, A.A., Filatov, D.A., Olonina, S.I., Kazakov, A.V., & Olonin, I.Y. (2021). Influence of the radiation intensity of LED light sources of the red-blue spectrum on the yield and energy consumption of microgreens. *IOP Conference Series: Earth and Environmental Science,* 723(3), article number 032046. doi: 10.1088/1755-1315/723/3/032046.

Лариса Євгенівна Никифорова
Доктор технічних наук, професор
Національний університет біоресурсів і природокористування України
03041, вул. Героїв Оборони, 15, м. Київ, Україна
https://orcid.org/0000-0001-6913-1672

Микола Олександрович Кіктєв
Кандидат технічних наук, доцент
Національний університет біоресурсів і природокористування України
03041, вул. Героїв Оборони, 15, м. Київ, Україна
https://orcid.org/0000-0001-7682-280X

Тарас Іванович Лендєл
Кандидат технічних наук, доцент
Національний університет біоресурсів і природокористування України
03041, вул. Героїв Оборони, 15, м. Київ, Україна
https://orcid.org/0000-0002-6356-1230

Сергій Володимирович Павлов
Доктор технічних наук, професор
Вінницький національний технічний університет
21021, Хмельницьке шосе, 95, м. Вінниця, Україна
https://orcid.org/0000-0002-0051-5560

Павло Миколайович Мазурчук
Аспірант
Національний університет біоресурсів і природокористування України
03041, вул. Героїв Оборони, 15, м. Київ, Україна
https://orcid.org/0009-0000-0064-8999

Комп'ютерно-інтегрована система керування електрофізичними методами підвищення продуктивності рослин

Анотація. У зв'язку зі зростанням попиту на аграрну продукцію, виникає потреба інтенсифікації процесу вирощування рослин, зменшення їх захворювань. Тому технічна реалізація методів управління функціональною активністю рослин за допомогою електромагнітного випромінювання на різних етапах органогенезу та їх автоматизація є актуальною задачею. Метою статті було підвищення ефективності вирощування росли шляхом дослідження електрофізичних методів управління їх продуктивністю та реалізації комп'ютерно-інтегрованої системи. Для реалізації поставленої мети була використана математична коригуюча модель взаємодії лазерного випромінювання із твердою біологічною тканиною, алгоритми вимірювання і формування управляючих впливів, методи теорії автоматичного управління, а також візуальне програмування в пакеті LabView. Дані оброблялися в пакеті MS Excel. Проаналізовано зв'язки в біотехнічній системі рослина-середовище, виділені матеріальні потоки та інформаційні канали, виокремлена множина параметрів стану, прямі та перехресні взаємозв'язки між ними, аргументовані джерела збурень. Визначено основні положення взаємодії лазерного випромінювання з біологічною тканиною та обґрунтовано біофізичний механізм. Розроблено комплекс програмно-апаратних засобів контролю та керування для проведення експериментальних досліджень режимів електрофізичного впливу на рослинні біологічні об'єкти. З метою отримання зворотного зв'язку від рослин розроблено новий інструментарій діагностики фізіологічного стану рослинних організмів та створено комп'ютерно-інтегровану систему керування процесом опромінення рослин. На базі програмного забезпечення мікроконтролера Arduino реалізована система управління, яка підключається до ПК. Створено панель оператора, де забезпечено автоматизоване керування процесом та розроблена підсистема реєстрації вимірюваних даних. На практиці результати цього дослідження можуть бути застосовані у тепличних господарствах України та інших країн, в тому числі при вирощувані овочевих культур

Ключові слова: обробка насіння; біотехнічна система; лабораторна установка; платформа; алгоритм; автоматизація; інтегрована плата

Machinery & Energetics
Vol. 14, No. 2. 2023

Journal homepage:
https://technicalscience.com.ua/en

UDC 631.171:631.334
DOI: 10.31548/machinery/2.2023.46

Natalia Pasichnyk
PhD in Agricultural Sciences, Associate Professor
National University of Life and Environmental Sciences of Ukraine
03041, 15 Heroiv Oborony Str., Kyiv, Ukraine
https://orcid.org/0000-0002-2120-1552

Oleksiy Opryshko*
PhD in Technical Sciences, Associate Professor
National University of Life and Environmental Sciences of Ukraine
03041, 15 Heroiv Oborony Str., Kyiv, Ukraine
https://orcid.org/0000-0001-6433-3566

Sergey Shvorov
Doctor of Technical Sciences, Professor
National University of Life and Environmental Sciences of Ukraine
03041, 15 Heroiv Oborony Str., Kyiv, Ukraine
https://orcid.org/0000-0003-3358-1297

Alla Dudnyk
PhD in Technical Sciences, Associate Professor
National University of Life and Environmental Sciences of Ukraine
03041, 15 Heroiv Oborony Str., Kyiv, Ukraine
https://orcid.org/0000-0001-9797-3551

Viktor Teplyuk
National University of Life and Environmental Sciences of Ukraine
03041, 15 Heroiv Oborony Str., Kyiv, Ukraine
https://orcid.org/0009-0002-3429-6738

Remote field monitoring results feasibility assessment for energy crops yield management

Abstract. Most vegetation indices for UAV data analysis are developed for low-resolution satellite platforms, which requires the use of other monitoring methods and agrochemical measures to accurately determine the state of plantations, considering different stages of vegetation and spectral characteristics. The research aims to develop a methodology for assessing the suitability of remote sensing spectral data for energy crop nutrition management. The study was conducted using winter crops, including wheat and rapeseed. The results for winter wheat for the period from 2017 to 2020 were analysed. Stresses associated with nutrient deficiencies were studied in the fields of long-term stationary experiments at the National University of Life and Environmental Sciences of Ukraine. The results obtained from the Slantrange sensor and Slantview software were used. The studies confirmed that the pixel distribution in images of plantations (wheat and winter rape) can be described by a Gaussian distribution. The coefficient of determination for wheat was higher than for rape due to the peculiarities of the plant leaf structure. For rapeseed, a higher coefficient of determination was found for the

Article's History: Received: 20/12/2022; Revised: 21/03/2023; Accepted: 26/04/2023.

Suggested Citation:
Pasichnyk, N., Opryshko, O., Shvorov, S., Dudnyk, A., & Teplyuk, V. (2023). Remote field monitoring results feasibility assessment for energy crops yield management. *Machinery & Energetics,* 14(2), 46-59. doi: 10.31548/machinery/2.2023.46.

*Corresponding author

lognormal distribution, which is not convenient for automating fertilisation processes in precision farming technologies. The analysis of the distribution by spectral channels, in particular the presence of several maxima, may indicate the presence of foreign inclusions or transitional stages of vegetation, which makes such data unsuitable for crop management. It has been established that if, after soil filtration, the maximum amplitude of the distribution exceeds the nearest one by more than 3 times, the growing season can be considered stable for a particular area, and the results of spectral monitoring are reliable for further analysis It has been confirmed that the vegetation indices GNDVI and RNDVI are not effective for assessing the reliability of data based on the standard deviation of the distribution. Reference values of the standard deviation of the distribution can be established at research stations with controlled stress factors, which will help in crop management

Keywords: precision agriculture; data suitability; vegetation indices; Gaussian distribution

INTRODUCTION

Unmanned aerial vehicles (UAVs) are an innovative tool for field monitoring that addresses some of the significant drawbacks of satellite systems, such as inaccessibility, high cost, and limited image resolution. However, most vegetation indices used to analyse UAV data have been developed for satellite platforms with low resolution, where a group of plants is displayed in a single pixel. The indices based on the "soil line" concept are mainly aimed at assessing the presence of biomass, but other methodological approaches are needed to monitor crop production. The spectral characteristics of plants also depend on the stages of vegetation, and in such cases, the calculation of the average value for the entire plot, which is typical for satellite monitoring, is not sufficiently accurate.

The problem of determining the conformity of the results of spectral monitoring of plantations with their condition remains unresolved. Unless this issue is resolved, the automation of processes for differentiated fertiliser applications remains unresolved, which critically affects the technical aspect of precision agriculture. Erroneous data on the interpretation of monitoring results fundamentally complicate the selection of plantations for the production of pellets, heat briquettes and biogas. Developing a methodology for assessing the suitability of remote sensing spectral data for nutrition management, and hence crop formation, was the research goal.

Researchers were interested in the presence of crops and their nomenclature, while the issue of crop management was less relevant. The task of obtaining and interpreting information has become fundamentally more complex for precision farming technology, as the spectral characteristics of objects depend significantly on lighting conditions. With this in mind, a set of technical and organisational measures is used to achieve data reproducibility. H. Aasen *et al.* (2015) considered the construction of 3D plant models, where a methodology for combining data from several flights is proposed to achieve high accuracy. Despite interesting results, this approach requires several consecutive flights in different directions, which is not practical on an industrial scale with limited time. F. Liu *et al.* (2021b) consider an approach to determine plant architecture features by mass phenotyping using UAVs and comparing spectral portraits with reference templates. Information on plant size is useful for detecting stress conditions. However, in the early stages of the growing season, high image resolution is required to accurately identify plant conditions, which can only be obtained from low altitudes, making it difficult to use this technology on an industrial scale. Another technical tool for estimating plant size is LiDAR (Light Detection and Ranging), which is described in the review article by H. Dhami *et al.* (2020). However, even this innovative equipment, according to a study by B.P. Banerjee *et al.* (2019), is less effective for small plants with leaves only a few millimetres wide.

R. Lottering & K. Peerbhay (2022) proposed a different approach to identifying the spread of pests in the forest, based on the use of reference values of plant spectral parameters. The authors estimate the deviation of NDVI (Normalised difference vegetation index) from seasonal changes calculated at different stages of the growing season, since satellite imagery is performed at high frequency and data for a specific stage of plant development can be selected. However, in real production conditions, spectral equipment is a valuable resource, and it is necessary to minimise the number of flights.

Y. Cao *et al.* (2020) present an original approach to determining the state of plants by changing their dimensions using sugar beet as an example. The researchers proposed a new vegetation index – WDRVI (Wide-dynamic-range vegetation index), introduced with an additional coefficient for the infrared channel. However, the 5% increase in accuracy achieved requires compensation for the cost of determining dynamically changing coefficients for the infrared channel, which may not be feasible from the point of view of large-scale production. Given this, a more promising approach is to compare the spectral performance with certain reference samples.

The prospects of these innovative indices for crop yield management are described by N. Amarasingam *et al.* (2022). The standard functionality of Slantview is limited to ready-made vegetation indices and does not provide access to the original data adjusted for light and geolocation, so information about the channels was taken according to the method described by S. Shvorov *et al.* (2020).

G. Yan *et al.* (2019) showed that a decrease in the resolution of the images leads to a loss of the ability to distinguish separate bands corresponding to soil and plants. The approach was improved by A. Coy *et al.* (2016), where

the identification was refined by assessing the distribution of intensity values of colour components in CIELAB space. The authors used thresholds to determine the area of the plant dome. However, this approach can be effective only in the early stages of the growing season, when the shadow formed on the lower tiers of plant leaves can be neglected.

Soil and plant identification in the study of L. Li *et al.* (2018) were based on the left or right half of the Gaussian distribution. This approach allows for the identification of two components in the presence of three components, but its effectiveness is questionable.

Thus, the analysis of the literature shows that the Gaussian distribution describes the dependence of the number of pixels on the intensity values of colour components for plants and soil. However, the above studies were conducted under stationary conditions with the same plant growing season and air-dry soil conditions. For practical implementation, it is necessary to explore other options, including production fields.

MATERIALS AND METHODS

The study was conducted using winter crops, including wheat and rapeseed. For winter wheat, the results obtained during the period from 2017 to 2020 were analysed. Stresses associated with nutrient deficiencies were investigated in the fields of long-term stationary experiments conducted at the Department of Agrochemistry and Crop Production Quality of the National University of Life and Environmental Sciences of Ukraine, where fertiliser application systems are studied.

This study was conducted under the Convention on Biological Diversity (2022). Multispectral studies in the infrared range were carried out using the Slantrange 3p system (USA) and Slantview software (version 2.13.1.2304), specially developed for this sensor equipment. A feature of Slantview software is the ability to create maps of vegetation index distribution directly quickly and autonomously on the field. It also provides the formation of a general orthophoto plan from the images, and lighting correction and provides the user with ready-made maps of the distribution of vegetation indices, such as various variants of NDVI (Normalised difference vegetation index). Using standard Slantview software tools, the data can be exported in GeoTIFF format. Rapeseed plots with and without signs of technological stress were considered in the study. Data from individual spectral channels and vegetation indices calculated by Slantview were analysed.

To ensure clear identification of pixels in the image, reference points were used, which were implemented in the Slantview software for the image and map windows. These points were present both in the map window and in the images (Fig. 1). Slantview has a distance measurement option in the map window, which is not available in the image window. Therefore, to accurately identify the position of the study plots on the images, it is necessary to have at least two reference points with a known distance between them.

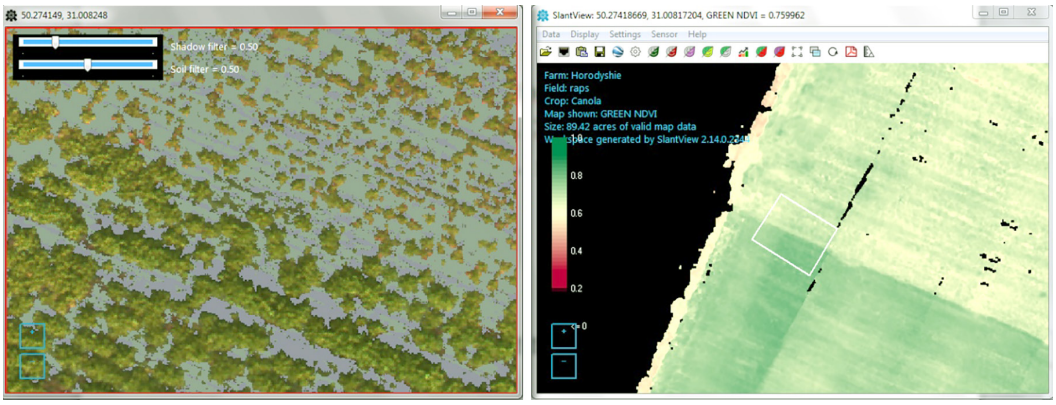

Figure 1. Slantview interfaces, with the "snapshots" and "maps" windows on the left and right, respectively (Green NDVI index)

Note: a white quadrangle in the map window marks the area displayed in the snapshot window

Source: compiled by the authors

The highest detail (GSD of 0.04 m/pixel) was obtained using the snapshot window in Slantview software, which provides access to various NDVI options such as Green, Red and RedEdge. When studying the results for individual spectral channels in the snapshot window, monochrome images were used, which were saved in BMP format to preserve complete information. To do this, Paint (Microsoft Windows 7.0 Sp.1) was used to copy the screen.

Using the map window in Slantview, a smaller-scale map of the index distribution was obtained. In this window, in addition to the standard NDVI indices, indices proposed by Slantview developers, such as Stress, Vegetative fraction and Yield potential, were calculated. The methodology was further improved by using reference points that were also displayed in the image window for individual spectral channels (Pasichnyk *et al.*, 2021). The minimum scale (GSD 0.5 m/pixel) of the index distribution was obtained from the geotiff file, where geospatial data can be stored in Slantview software. Statistical processing of the experimental data on the distribution parameters was carried

out using OriginPro v/8.0951 (B951) software developed by OriginLab Corporation.

For the mathematical processing of the spectral data, an approach described by D. Liu *et al.* (2021a), when the distribution was considered as a Gaussian distribution, was used. This particular approach focuses on the early stages of the growing season, when the number of pixels associated with plants and soil is approximately the same, and correctly uses the sum of two Gaussian distributions – one for soil presence and the other for plants, and in the later stages of the growing season, the proportion of the sum attributed to plants will dominate the proportion due to soil, which requires modification of the methodology for assessing the suitability of spectral data for crop management.

In the first stage, using the amplitude version of the modified Gaussian function (GaussAmp) without a shift along the ordinate axis, the parameters of the distribution of the largest peak (Max1) were calculated based on experimental data.

$$N = A \times exp^{\frac{-(X-xc)^2}{2w^2}}, \quad (1)$$

where N – number of measurements (in our case, the number of pixels); X – colour component intensity, A – amplitude; xc – average value; w – standard deviation (according to value A/2).

The amplitude version of the Gaussian function was selected as it better describes peak values compared to the classical Gaussian function and is also easier to adapt to the variable size of the experimental plots, which is important for the industrial implementation of solutions.

In the second stage, based on the results of experimental measurements (EHR) and the calculated values of Max1, the difference between them was calculated (EHR – Max1). In the third stage, using expression (1), the results obtained at stage 2 for the second maximum of the distribution (Max2) were calculated. In the fourth stage, the calculated distribution data for (EHR – Max2) were subtracted from the experimental data. In the fifth stage, the parameters of the distribution equation for MAX1 were refined based on the results obtained in stage 4. Stages 2-5 can be performed cyclically to refine the results. The calculations are terminated when the difference in the mean value of the distribution before and after the cycle becomes less than 1.

RESULTS AND DISCUSSION

Following a study by V. Lysenko *et al.* (2018), the state of nitrogen nutrition can be assessed in the optical range. No characteristic colouration was found for technological stresses (Dolia, *et al.*, 2019). However, plants that were damaged by the phytotoxic effect of herbicides or the aftereffects of their application showed typical signs of damage, such as curvature of the leaf blade (Fig. 2). As a result, fragments of the upper and lower sides of the leaf blade were recorded during horizontal scanning.

Technological stresses on winter rape caused abnormal colouration of the 2 lower leaves, the palette of which, depending on the stage of development and the nature of the stress, contained from white to red-yellow-purple colours (Fig. 3).

Figure 2. Winter wheat crops were affected by herbicide residue, which caused leaf curl

Figure 3. Winter oilseed rape crops with the abnormal colouration of the 2 lower leaves, which is a sign of technological stress (2020.10.28)

Stresses associated with technological operations were investigated in the production fields of farms located in the Kyiv region. The presence of technological stress was noted by the farm's employees since, as a result of the unusually warm and snowy winter, herbicides from the previous season were not destroyed, which led to the damage of winter crops.

Figure 4 shows the results of the calculations for the red component for the experimental wheat data obtained in 2017.05.05.

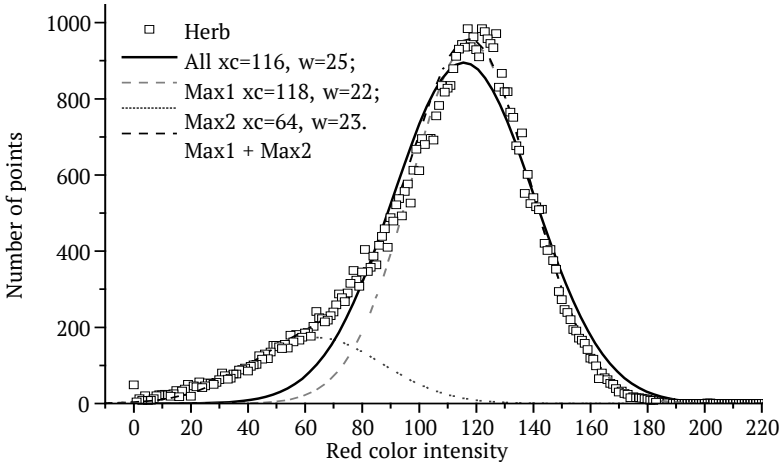

Figure 4. Results of approximation of the dependence of the number of pixels on the intensity of the red colour component (2017.05.05)

Source: compiled by the authors

According to the data presented, the use of the proposed methodology showed that the mean value of the distribution increased by 2 units while the standard deviation w decreased by 3 units. The nature of the distribution corresponds to the data presented in the study by L. Li *et al.* (2018), but it is more correct to consider not one but the sum of 2 distributions, Max1 and Max2, which overlap. This contradicts the results presented in D.-Zh. Liu *et al.* (2021a), but the researchers considered the initial stages of vegetation and the overlap in the results can be explained by possible effects due to the peculiarities of the jpeg data storage format.

The presence of a distribution of Max2 can be explained by the presence of a shadow on the lower leaves that differs from the upper ones, as well as by soil fixation. The proposed approach to processing experimental results will be effective if a condition Max1≫Max2. In practical application, a situation is often encountered when plants of the same crop are simultaneously present in the field at different stages of vegetation or in different physiological states (for example, after the appearance of the flag leaf, which was recorded during the monitoring on 2018.06.08). The analysis of the dependencies presented in Figure 5 shows that Max1≅Max2. This gives grounds to use an approach where, at the first stage, two Gaussian distributions are separately determined, and then 2 separate distributions are considered in parallel.

It is possible to detect the presence of several separate maxima by using expression (1) to describe the experimental results and knowing the value of the standard deviation. For the results obtained, the value of w was 28. However, if we consider the data as the sum of three distributions, Max1, Max2, and Max3, the corresponding w values were between 18 and 23, which is typical for plants and soil (Fig. 5).

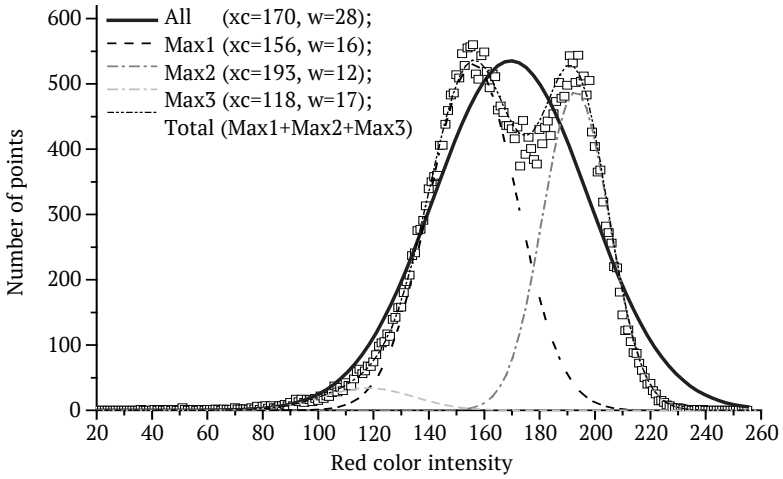

Figure 5. Results of approximation of the dependence of the number of pixels on the intensity of the red colour component for winter wheat (2018.06.08 – there is a flag sheet)

Source: compiled by the authors

The results obtained by approximating the data using the general Gaussian relationship (All) are incorrect since the mean value of the general distribution does not correspond to any of the maximums of the distributions. This indicates that the plants were monitored in a transitional state. Thus, the vegetation stage can be considered stable for the site, and the results of its spectral monitoring are reliable if, after soil filtration, the maximum amplitude of the distribution exceeds the closest amplitude by more than 3 times. Therefore, it is recommended to repeat the experiment in a few days when the crop has fully entered the appropriate vegetation phase. To automate the processing of the monitoring results, you can obtain reference values for the pixel distribution by conducting stationary experiments.

For universal optical range digital cameras like the FC200, it is not necessary to observe the selectivity of the filters exactly. Therefore, to verify the results obtained, a study was carried out using the specialised spectral complex Slantrange 3. The results of these studies, showing a lack of mineral nutrition, are shown in Figure 6.

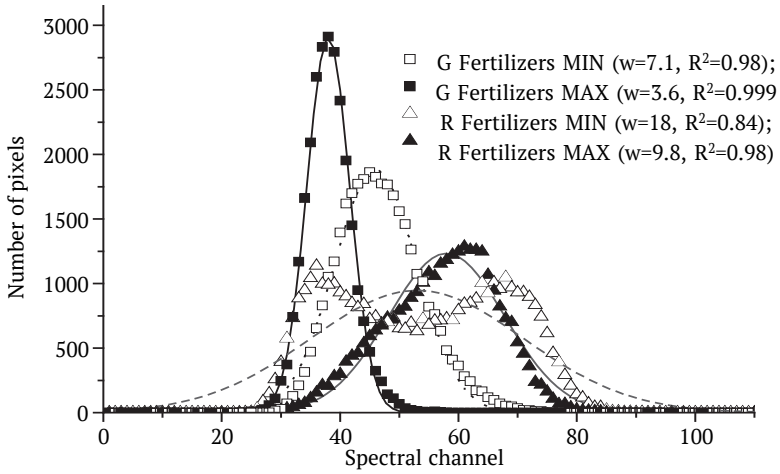

Figure 6. Dependence of the number of pixels on the intensity of green (G) and red (R) colour components (27.04.20)
Note: Fertilisers MAX – 1.5 norms of mineral fertilisers have been applied; Fertilisers MIN – no fertilisers have been applied
Source: compiled by the authors

When the experimental data were approximated using GaussAmp, the standard deviation for the green channel was 7.1 for stressed plants and 3.6 for healthy plants (with a coefficient of determination $R^2 \geqslant 0.98$). Regarding the red component, regardless of the nutritional condition, two maxima were observed, which were more pronounced in conditions of insufficient nutrition. Similarly, to the green channel, for the red channel, the standard deviation for healthy plants was about half that of plants under stress – 9.8 and 18, respectively. The coefficient of determination for the increased rate of mineral fertilisers was 0.98, and for damaged plants – 0.84. Studies on the manifestation of technological stress caused by herbicide aftereffects were conducted on production fields near the village of Hvardiyske with latitude 50.0347 and longitude 30.0286. This is shown in Figure 7.

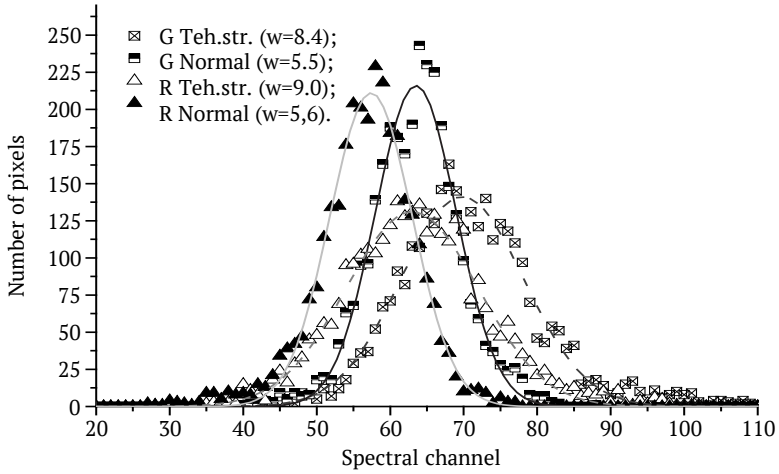

Figure 7. The dependence of the number of pixels on the intensity of the green (G) and red (R) colour components and the presence of technological stresses (The.str). Date of research: 2020.04.27
Source: compiled by the authors

According to the results obtained, the width of the distribution for the green and red channels was 1.5 times larger for plants under stress compared to healthy plants. In the red channel, there were no two distinct maximums of the distribution, regardless of the presence of technological stress, in contrast to the results obtained at the experimental station. The coefficient of determination R2 was ⩾ 0.98 regardless of the channel. The authors assume that the difference in plant development in the production field and the experimental station is due to different sowing dates and wheat varieties. Given that sowing can take several days, the use of unmanned aerial vehicles (UAVs) has an additional advantage over satellite platforms in terms of data reliability.

Vegetation index distribution maps for wheat

To conduct research using remote sensing with the help of unmanned aerial vehicles (UAVs), the width of the study areas of the hospital was relatively small. Therefore, the results from the Slantview software map window were used to obtain data for the studies. The results of the research on stresses related to power shortages and technological stresses are shown in Figure 8.

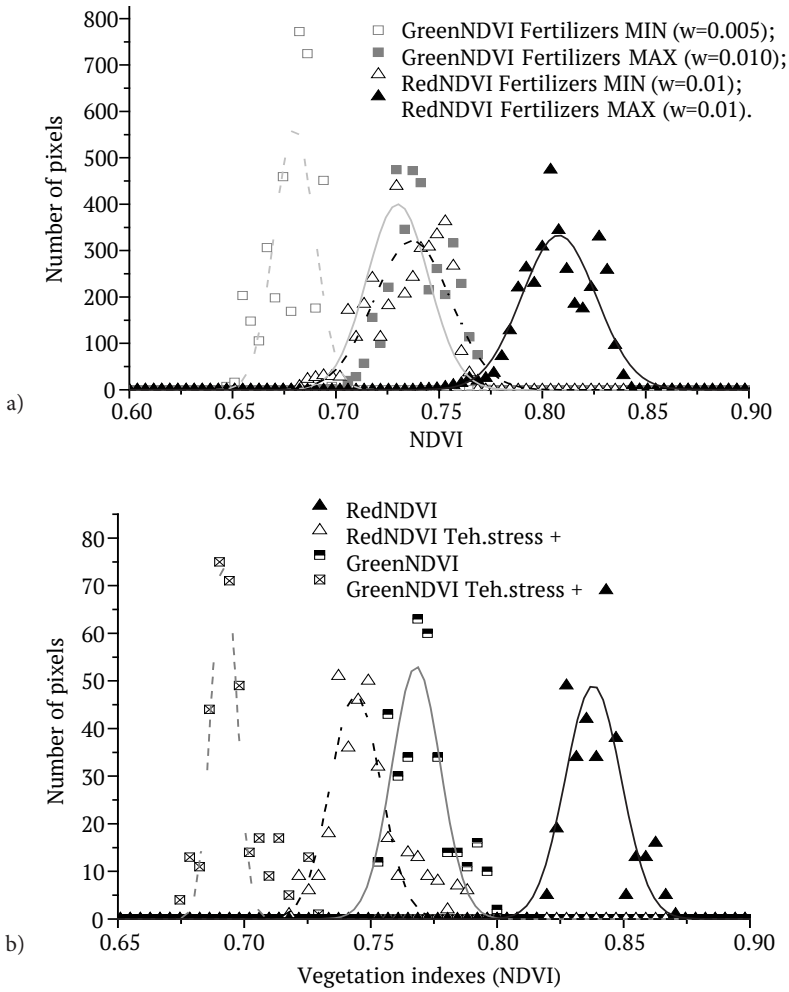

Figure 8. Dependence of the number of pixels on the value of the vegetation index GreenNDVI (GNDVI) and RedNDVI (RNDVI)

Note: a – stress caused by nutrient deficiency – fertilisers; b – stress caused by inadequate performance of technological operations – stress

Source: compiled by the authors

Considering the obtained experimental results, it is possible to conclude that the characteristics of the Gaussian distribution for pixels of the NDVI vegetation index map differ significantly from those obtained directly using spectral channels. For example, for NDVI, the standard deviation of the distribution in damaged plants was equal to or even smaller than in healthy plants (in contrast to the results obtained using spectral channels). The coefficient of determination for the NDVI distribution was 0.85-0.95, which is significantly lower than the distribution obtained using the green and red spectral channels. This implies that the use of standard NDVI indices does not allow for a sufficient assessment of the suitability of spectral monitoring results for further analysis.

Winter rape (separate spectral channels)

In the early stages of plant growth, it is not enough to completely cover the soil. Slantview software is not capable of filtering out soil and shadows in images acquired using spectral channels. Therefore, to identify plants, we used the infrared channel (NIR 800-900 nm) to filter the soil. The monitoring was carried out under uniform cloud cover, so shadows from the leaves were not considered during the filtration. It was found that, in comparison with wheat, the experimental data for rape are better described by a lognormal dependence, considering the value of the coefficient of determination:

$$N = \frac{A1}{\sqrt{2\pi}w1X} e^{\frac{-\left[ln\frac{X}{xc}\right]}{2w1^2}}, \quad (2)$$

where N – number of measurements (in our case, the number of pixels); X – intensity of the colour component (8-bit model), $A1$ – area; xc – mean; $w1$ – standard deviation (correlates with A1/2).

Based on the analysis of the distribution for rapeseed in the G channel (Fig. 9), it was found that the lognormal relationship is slightly better than the Gaussian relationship in explaining the left part of the distribution. This applies to the plots with healthy plants (40-50) and those showing technological stress (60-80). These results confirm the conclusions about the nature of the relationship given in W. Song *et al.* (2015), where the authors also considered the shadow from the upper leaves on the lower ones, which is probably relevant for plants with wide leaves such as rape.

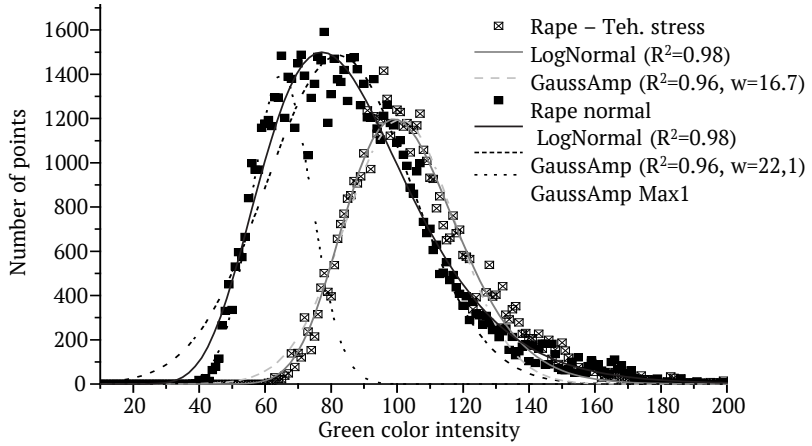

Figure 9. Results of approximation of the dependence of the number of pixels on the intensity of the green component of colour for winter rape (2019.10.30)

Source: compiled by the authors

Reducing errors can be achieved by considering the experimental results as a sum of Gaussian distributions, for example, using the Max1 function. This can be attributed to the fact that not only the length/width ratio is different, but also the dimensions of rapeseed leaves are much larger than those of wheat, and the camera can capture individual plant parts, such as "petiole", "leaf veins", etc., from the same height, and these parts create their distributions. The ratio of such parts can vary significantly, which will affect the distribution parameters and fundamentally complicate the interpretation of the data. The presence of a shadow additionally increases the number of factors that affect the results of spectral studies. As a solution to this problem, which is necessary for crop management in crop production practices, Z.Y. Niu *et al.* (2021) and Z. Wang *et al.* (2023) proposed the use of machine learning technologies. However, the problems of neural network training, which are indicated in these papers when classifying plant images, may include the following aspects:

- Insufficient training data: for successful training of neural networks, a sufficient number of diverse plant images is required. However, collecting a large amount of high-quality data can be a time-consuming and resource-intensive process, especially when it comes to classifying a wide range of numerous plant varieties and hybrids, the number of which is growing every year.
- Unbalanced classes: an uneven distribution of images between different plant classes can sometimes occur in the training data. This can lead to incorrect weighting of certain classes during training, and the model may be more inclined to classify more represented classes.
- Influence of external factors: When capturing photos of plants, various factors can affect the image, such as lighting, angle, noise, and image resolution. These factors can create additional noise or change the appearance of plants, which makes it difficult to classify them, including by neural networks.
- Processing large amounts of data: classification of plant images can be computationally intensive and time-consuming, especially when deep learning and complex models are used. Processing large amounts of data can be burdensome for systems that are limited by computing power.

Q. Yuan & Z. Zuo (2022) tried to limit the number of training images to 800, but even this number can be problematic in terms of research organisation.

To overcome these problems approaches such as data augmentation, training set augmentation, the use of pre-trained models, transfer learning techniques, and neural

network architecture optimisation can be used. However, the issues remain controversial and require additional research, as shown in the study by H. Li & L. Zhang (2021). Thus, it is premature to consider the focus on machine learning technologies as the most promising approach.

Y. Liu *et al.* (2012) suggested using combinations of Gaussian distributions to obtain the average value of plant spectral parameters. This required capturing the bands belonging to plants and soil separately in the image. Although positive results were achieved, the high resolution of the images taken from a height of 3 metres made it difficult to apply on a large scale in industry.

As for the R channel, the nature of the distribution remained unchanged – the coefficient of determination was higher for the lognormal dependence than for the GaussAmp dependence (Fig. 10).

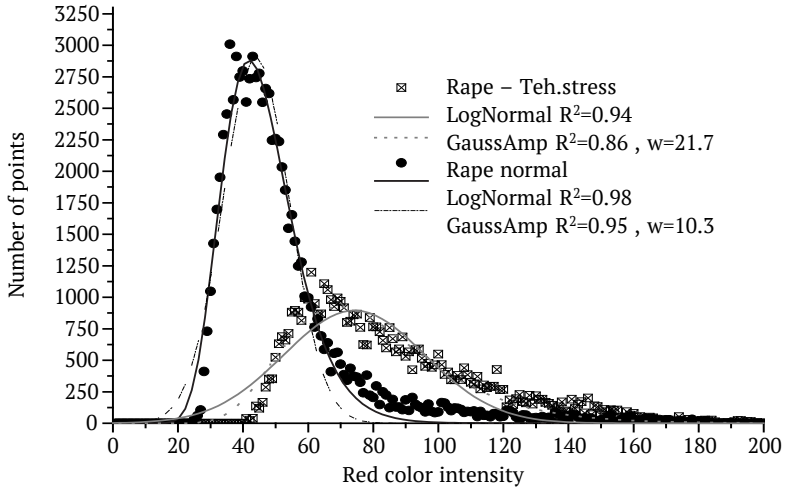

Figure 10. Results of approximation of the relationship between the number of pixels and the value of red colour intensity for winter rape (2019.10.30)

Source: compiled by the authors

When the experimental data were approximated by the Gaussian equation, the standard deviation for healthy plants was half that of plants showing technological stress (as opposed to the G channel). This is probably due to the abnormal colour of the two lower leaves of rapeseed affected by technological stress, which have a palette of yellow to red colours. The results obtained for the RedEdge spectral channel are similar to those for the green channel (Fig. 11). The use of a lognormal relationship instead of GaussAmp to approximate the experimental data did not bring a significant improvement – the R^2 value increased by only 0.006.

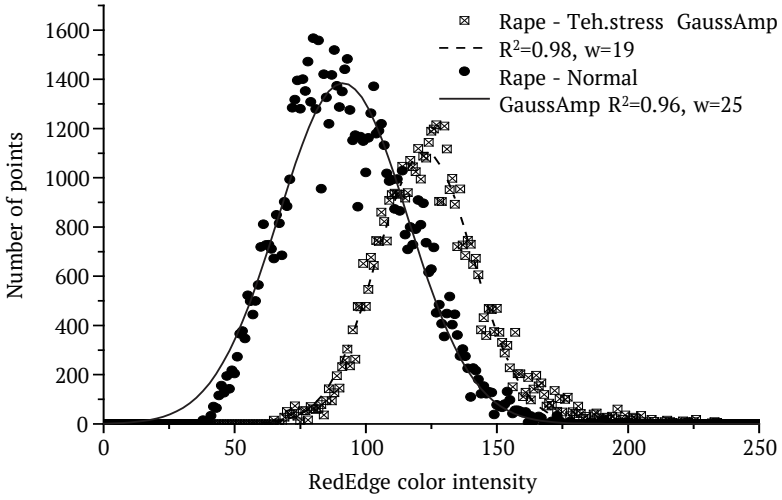

Figure 11. Results of approximation of the dependence of the number of pixels on the intensity of the green component of colour for winter rape (2019.10.30)

Source: compiled by the authors

Winter rape (maps of the distribution of vegetation indices)
For vegetation indices, the possibility of soil and shadow filtering is provided, but the manufacturer does not disclose the algorithms, so the parameters recommended by the developers were used (Soil filter = 0.5, Shadow filter = 0.5). The results are presented in Table 1.

Table 1. Results of approximation of experimental data using GaussAmp distribution for winter rape plots

No.	Index	GSD m/pixel	Plot sample	xc	*w*	R^2	$w_p/w_{r.t.str}$
1	2	3	4	5	6	7	8
1	Green NDVI	0.04	Rapeseed + technical stress	0.671	0.039	0.972	***1.05***
2			Rapeseed	0.767	0.041	0.921	
3		0.25	Rapeseed + technical stress	0.675	0.016	0.932	0.5
4			Rapeseed	0.772	0.008	0.915	
5		0.5	Rapeseed + technical stress	0.671	0.015	0.961	0.53
6			Rapeseed	0.767	0.008	0.967	
7	RedNDVI	0.04	Rapeseed + technical stress	0.716	0.06	0.945	*0.067*
8			Rapeseed	0.830	0.004	0.848	
9		0.25	Rapeseed + technical stress	0.72	0.016	0.966	0.56
10			Rapeseed	0.83	0.009	0.958	
11		0.5	Rapeseed + technical stress	0.717	0.012	0.971	0.75
12			Rapeseed	0.823	0.009	0.961	
13	RedEdgeNDVI	0.04	Rapeseed + technical stress	0.39	0.117	**0.792**	***0.812***
14			Rapeseed	0.578	0.095	**0.711**	
15		0.25	Rapeseed + technical stress	0.406	0.026	0.898	0.46
16			Rapeseed	0.567	0.012	0.921	
17		0.5	Rapeseed + technical stress	0.384	0.034	0.899	0.59
18			Rapeseed	0.560	0.020	0.877	
19	Stress	0.5	Rapeseed + technical stress	0.305	0.215	0.02	0.037
20			Rapeseed	0.372	0.008	0.902	
21	Veg. Fract.	0.5	Rapeseed + technical stress	0.068	0.029	0.732	0.65
22			Rapeseed	0.439	0.019	0.258	
1	2	3	4	5	6	7	8
23	Yield pot.	0.5	Rapeseed + technical stress	0.068	0.029	0.732	3.1
24			Rapeseed	0.49	0.09	0.65	

Source: compiled by the authors

Table 1 of the results shows that the lowest coefficient of determination was obtained for the RedEdge spectral channel at the maximum resolution. According to Figure 12, regardless of the presence of technological stress, two separate distributions with different amplitudes are observed for winter rape in the RedEdge channel.

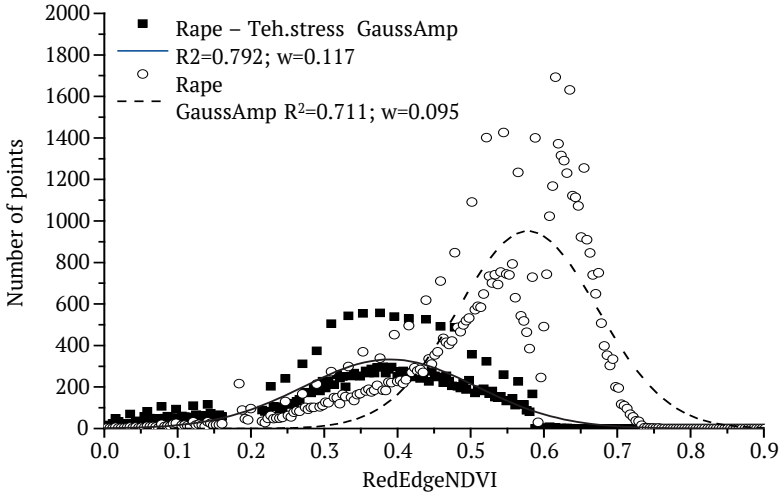

Figure 12. Results of approximation of the dependence of the number of pixels on the value of the RedEdgeNDVI index at GSD=0.04 for winter rape (2019.10.30)

Source: compiled by the authors

One of the possible reasons for this phenomenon is the difference in the fixation of individual components of the leaves and stem of rape in this range. This is confirmed by the fact that when the resolution decreases (GSD⩾0.25), this phenomenon is no longer observed. This phenomenon was not observed for other variants of the NDVI index. In the future, a specific study of this phenomenon for the RedEdge channel could be useful for foliar diagnosis of rapeseed.

The presence of a significant difference in the NDVI index between healthy and damaged rape plants, in our opinion, is explained by the abnormal colouration characteristic of technological stresses, which is not recorded in the considered spectral ranges for wheat. For all variants of the NDVI index with a resolution of GSD⩾0.25, the standard deviation (w) for plots with rapeseed damaged by technological factors was larger than for healthy plants. With the high resolution of Slantview software, recording organic residues from the previous crop as separate objects, the following manifestations are observed (Fig. 13).

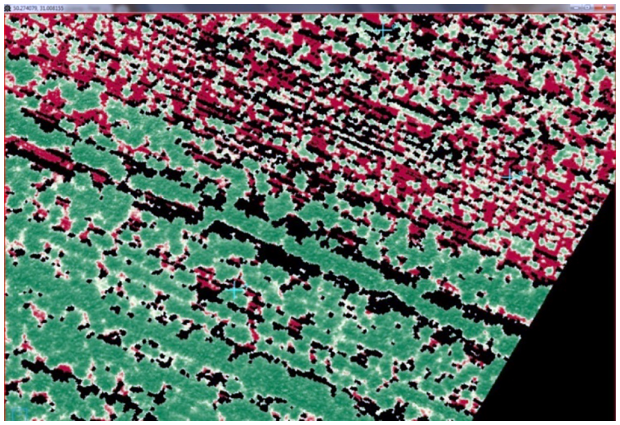

Figure 13. Image of the Slantview software image window with the distribution of the RedNDVI index for the boundary between healthy rapeseed plants (bottom) and those with technological stress (top)
Note: blue crosses indicate reference points for pixel positioning in different spectral channels
Source: compiled by the authors

The study considers the Slantrange system to capture maps of vegetation index distribution only at maximum resolution. This software operation mode and the use of the snapshot window interface allow the agronomist to assess the quality of tillage and the number of organic residues in the fields. High-resolution maps of vegetation index distribution can be useful for estimating not the total plant area, but separately for determining the area of photosynthetically active leaves. For example, leaf borders have lower vegetation index values in the images, and damaged plants with underdeveloped leaves have a higher percentage of the area covered by leaf mass.

CONCLUSIONS

The study experimentally confirmed the statement that the distribution of pixels in images of plantations (wheat and winter rape) can be described by a Gaussian distribution. The coefficient of determination in the approximation of experimental data for wheat is higher than for rape, which can be explained by the peculiarities of the plant leaf structure. For rapeseed, the highest coefficient of determination was obtained for a lognormal distribution. Such a distribution is inconvenient given the automation of fertilisation processes in precision farming technologies.

Analysis of the distribution by spectral channels, in particular the presence of several maxima, may indicate the presence of foreign inclusions or transitional stages of vegetation, which means that such data may not be suitable for crop management.

The vegetation stage can be considered stable for a particular site, and the results of spectral monitoring are reliable for further analysis if, after soil filtration, the maximum distribution amplitude exceeds the nearest value by more than 3 times, based on agronomic crop management rules.

The reliability of the data can be assessed based on the calculated standard deviation of the colour component distribution for pixels, rather than the average value used for traditional vegetation indices. The reference values of the standard deviation for the proposed GaussAmp equation for approximating experimental data should be established at research stations with controlled stress factors.

The GNDVI and RNDVI vegetation indices proved to be ineffective for assessing data reliability based on the standard deviation of the distribution. This highlights the need to introduce additional packages in GIS that separately describe the green and red spectral channels for inclusion in the standard set of vegetation indices.

The issue of shadowing from the upper leaves to the lower leaves significantly affects the distribution results and, accordingly, the assessment of the suitability of the data for crop management, machine learning technologies are a possible option, which, despite their effectiveness, will have to be adjusted for all varieties and hybrids separately. In further research, the use of alternative colour formation models is a possible solution to this issue.

ACKNOWLEDGEMENTS

The authors would like to express their sincere gratitude to Dmytro Komarchuk, a member of the NULES of Ukraine, and Oksana Zui from Odesa National University for their assistance in the filming.

CONFLICT OF INTEREST

The authors declare no conflict of interest.

REFERENCES

[1] Aasen, H., Burkart, A., Bolten, A., & Bareth, G. (2015). Generating 3D hyperspectral information with lightweight UAV snapshot cameras for vegetation monitoring: From camera calibration to quality assurance. *ISPRS Journal of Photogrammetry and Remote Sensing*, 108, 245-259. doi: 10.1016/j.isprsjprs.2015.08.002.

[2] Amarasingam, N., Salgadoe, A.S.A., Powell, K., Gonzalez, L.F., & Natarajan, S. (2022). A review of UAV platforms, sensors, and applications for monitoring of sugarcane crops. *Remote Sensing Applications: Society and Environment*, 26, article number 100712. doi: 10.1016/j.rsase.2022.100712.

[3] Banerjee, B.P., Raval, S., Cullen, P.J., & Kumar Singh. S. (2019). Mapping of complex vegetation communities and species using UAV-LIDAR metrics and high-resolution optical data. In *2019 IEEE International Geoscience and Remote Sensing Symposium* (6110-6113). Yokohama: IEEE. doi: 10.1109/IGARSS.2019.8899160.

[4] Cao, Y., Li, G.L., Luo, Y.K., Pan, Q., & Zhang, S.Y. (2020) Monitoring of sugar beet growth indicators using wide-dynamic-range vegetation index (WDRVI) derived from UAV multispectral images. *Computers and Electronics in Agriculture*, 171, article number 105331, doi: 10.1016/j.compag.2020.105331.

[5] Convention on Biological Diversity. (2022). Retrieved from https://www.cbd.int/convention/.

[6] Coy, A., Rankine, D., Taylor, M., Nielsen, D.C., & Cohen, J. (2016). Increasing the accuracy and automation of fractional vegetation cover estimation from digital photographs. *Remote Sensing*, 8, article number 474. doi: 10.3390/rs8070474.

[7] Dhami, H., Yu, K., Xu, T., Zhu, Q., Dhakal, K., Friel, J., Song, L., & Tokekar, P. (2020). Crop height and plot estimation for phenotyping from unmanned aerial vehicles using 3D LiDAR. In *2020 IEEE/RSJ International Conference on Intelligent Robots and Systems (IROS)* (pp. 2643-2649). Las Vegas: IEEE. doi: 10.1109/IROS45743.2020.9341343.

[8] Dolia, M., Lysenko, V., Pasichnyk, N., Opryshko, O., Komarchuk, D., Miroshnyk, V., Lendiel, T., & Martsyfei, A. (2019). Information technology for remote evaluation of after effects of residues of herbicides on winter crop rape. In *2019 3rd International Conference on Advanced Information and Communications Technologies (AICT)* (pp. 469-473). Lviv: IEEE. doi: 10.1109/AIACT.2019.8847850.

[9] Li, H., & Zhang, L. (2021) A bilevel learning model and algorithm for self-organizing feed-forward neural networks for pattern classification. *IEEE Transactions on Neural Networks and Learning Systems*, 32(11), 4901-4915. doi: 10.1109/TNNLS.2020.3026114.

[10] Li, L., Mu, X., Macfarlane, C., Song, W., Chen, J., Yan, K., & Yan, G. (2018) A half-Gaussian fitting method for estimating fractional vegetation cover of corn crops using unmanned aerial vehicle images. *Agricultural and Forest Meteorology*, 262, 379-390. doi: 10.1016/j.agrformet.2018.07.028.

[11] Liu, D.-Zh., Yang, F.-F., & Liu, S.-P. (2021a). Estimating wheat fractional vegetation cover using a density peak k-means algorithm based on hyperspectral image data. *Journal of Integrative Agriculture*, 20(11), 2880-2891. doi: 10.1016/S2095-3119(20)63556-0.

[12] Liu, F., Hu, P., Zheng, B., Duan, T., Zhu, B., & Guo, Y. (2021b) A field-based high-throughput method for acquiring canopy architecture using unmanned aerial vehicle images. *Agricultural and Forest Meteorology*, 296, article number 108231. doi: 10.1016/j.agrformet.2020.108231.

[13] Liu, Y., Mu, X., Wang, H., & Yan, G. (2012) A novel method for extracting green fractional vegetation cover fromdigital images. *Journal of Vegetation Science*, 23, 406-418. doi: 10.1111/j.1654-1103.2011.01373.x.

[14] Lottering, R., & Peerbhay, K. (2022). Mapping wattle rust induced defoliation within South Africa's wattle commercial forest plantations over two seasons. In *2022 International Conference on Electrical, Computer and Energy Technologies (ICECET)* (pp. 1-5). Prague: IEEE. doi: 10.1109/ICECET55527.2022.9872628.

[15] Lysenko, V., Opryshko, O., Komarchuk, D., Pasichnyk, N., Zaets, N., & Dudnyk, A. (2018). Information support of the remote nitrogen monitoring system in agricultural crops. *International Journal of Computing*, 17(1), 47-54.

[16] Niu, Y., Han, W., Zhang, H., Zhang, L., Chen, H. (2021). Estimating fractional vegetation cover of maize under water stress from UAV multispectral imagery using machine learning algorithms. *Computers and Electronics in Agriculture*, 189, article number 106414. doi: 10.1016/j.compag.2021.106414.

[17] Pasichnyk, N., Komarchuk, D., Opryshko, O., Shvorov, S., & Zui, O. (2021). Validation of data obtained after field sensing using UAV for management of future crops. *CEUR Workshop Proceeding*, 3126, 328-334.

[18] Shvorov, S., Lysenko, V., Pasichnyk, N., Rosamakha, Y., Rudenskyi, A., Lukin, V., Martsyfei, A. (2020). The method of determining the amount of yield based on the results of remote sensing obtained using UAV on the example of wheat. In *2020 IEEE 15th International Conference on Advanced Trends in Radioelectronics, Telecommunications and Computer Engineering (TCSET)* (pp. 245-248). Kyiv: IEEE. doi: 10.1109/PICST47496.2019.9061238.

[19] Song, W., Mu, X., Yan, G., & Shuai, H. (2015). Extracting the green fractional vegetation cover from digital images using a shadow-resistant algorithm (SHAR-LABFVC), *Remote Sensing*, 7(8), article number 10425. doi: 10.3390/rs70810425.

[20] Wang, Z., Chen, W., Xing, J., Zhang, X., Tian, H., Tang, H., Bi, P., Li, G., & Zhang, F. (2023). Extracting vegetation information from high dynamic range images with shadows: A comparison between deep learning and threshold methods. *Computers and Electronics in Agriculture*, 208, article number 107805. doi: 10.1016/j.compag.2023.107805.

[21] Yan, G., Li, L., Coy, A., Mu, X., Chen, S., Xie, D., Zhang, W., Shen, Q., & Zhou, H. (2019) Improving the estimation of fractional vegetation cover from UAV RGB imagery by colour unmixing. *ISPRS Journal of Photogrammetry and Remote Sensing*, 158, 23-34. doi: 10.1016/j.isprsjprs.2019.09.017.

[22] Yuan, Q., & Zuo, Z. (2022). Research on the performance of different convolutional neural network models on small datasets. In *2022 International Conference on Machine Learning and Intelligent Systems Engineering (MLISE)* (pp. 57-62). Guangzhou: IEEE. doi: 10.1109/MLISE57402.2022.00019.

Наталія Анатоліївна Пасічник
Кандидат сільськогосподарських наук, доцент
Національний університет біоресурсів і природокористування України
03041, вул. Героїв Оборони, 15, м. Київ, Україна
https://orcid.org/0000-0002-2120-1552

Олексій Олександрович Опришко
Кандидат технічних наук, доцент
Національний університет біоресурсів і природокористування України
03041, вул. Героїв Оборони, 15, м. Київ, Україна
https://orcid.org/0000-0001-6433-3566

Сергій Андрійович Шворов
Доктор технічних наук, професор
Національний університет біоресурсів і природокористування України
03041, вул. Героїв Оборони, 15, м. Київ, Україна
https://orcid.org/0000-0003-3358-1297

Алла Олексіївна Дудник
Кандидат технічних наук, доцент
Національний університет біоресурсів і природокористування України
03041, вул. Героїв Оборони, 15, м. Київ, Україна
https://orcid.org/0000-0001-9797-3551

Віктор Михайлович Теплюк
Національний університет біоресурсів і природокористування України
03041, вул. Героїв Оборони, 15, м. Київ, Україна
https://orcid.org/0009-0002-3429-6738

Оцінка придатності результатів дистанційного моніторингу полів для управління врожаєм енергетичних культур

Анотація. Більшість вегетаційних індексів для аналізу даних БПЛА розроблені для супутникових платформ низької роздільної здатності, що вимагає використання інших методів моніторингу та агрохімічних заходів для точного визначення стану рослинних насаджень, враховуючи різні стадії вегетації і спектральні характеристики. Тому головна мета дослідження – розробка методики оцінки придатності спектральних даних дистанційного моніторингу для управління живленням енергетичних культур. Дослідження проведено з використанням озимих культур, зокрема пшениці і ріпаку. Аналізувалися результати для пшениці озимої за період з 2017 по 2020 рік. Дослідження стресів, пов'язаних з нестачею елементів живлення, проводилися на полях багаторічних стаціонарних дослідів Національного університету біоресурсів і природокористування України. Використовувались результати отримані від сенсору Slantrange та програмного забезпечення Slantview. У проведених дослідженнях підтверджено, що розподіл пікселів на зображеннях рослинних насаджень (пшениці та ріпаку озимих) може бути описаний розподілом Гауса. Коефіцієнт детермінації для пшениці був вищим, ніж для ріпаку, через особливості будови листів рослин. Для ріпаку було виявлено вищий коефіцієнт детермінації для логнормального розподілу, який не є зручним для автоматизації процесів підживлення в технологіях точного землеробства. Аналіз розподілу за спектральними каналами, зокрема наявність кількох максимумів, може свідчити про наявність сторонніх включень або перехідних етапів вегетації, що робить такі дані непридатними для керування врожаєм. Встановлено, що якщо після фільтрації ґрунту максимальна амплітуда розподілу перевищує найближчу більш ніж в 3 рази, етап вегетації може вважатися стабільним для певної ділянки, а результати спектрального моніторингу є надійними для подальшого аналізу Підтверджено, що вегетаційні індекси GNDVI та RNDVI не є ефективними для оцінки надійності даних на основі стандартного відхилення розподілу. Еталонні значення стандартного відхилення розподілу можуть бути встановлені на дослідницьких станціях з контрольованими стресовими чинниками, що допоможе в керуванні врожаєм

Ключові слова: точне землеробство; придатність даних; вегетаційні індекси; розподіл Гауса

Machinery & Energetics
Vol. 14, No. 2. 2023

Journal homepage:
https://technicalscience.com.ua/en

UDC 662.763.3.2
DOI: 10.31548/machinery/2.2023.60

Viktor Polishchuk*
Doctor of Technical Sciences, Professor
National University of Life and Environmental Sciences of Ukraine
03041, 15 Heroiv Oborony, Kyiv, Ukraine
https://orcid.org/0000-0002-9654-9051

Timur Valiev
Postgraduate Student
National University of Life and Environmental Sciences of Ukraine
03041, 15 Heroiv Oborony, Kyiv, Ukraine
https://orcid.org/0000-0003-3400-6147

Study of the anaerobic destruction of post-alcohol distillery waste by mateen

Abstract. Post-alcohol distillery waste is an environmental pollutant, which determined the relevance of its disposal. One of the ways to utilise post-alcohol distillery waste is through its anaerobic methane destruction in biogas plants. The research aims to determine the optimal amount of post-alcohol distillery wastes to be added to the substrate to achieve maximum biomethane yield. The research was conducted on a laboratory biogas plant consisting of a 30-litre digester and a gas holder in a mesophilic mode at a substrate temperature of 40°C with a periodic substrate loading mode. It was found that the highest biogas yield of 5.369 l/(h·kg DOM) was obtained by anaerobic methane mono-degradation of post-alcohol distillery waste. However, the methane content in the biogas is in the range of 48-52%. During the anaerobic methane destruction of a mixture of post-alcohol distillery waste with cow manure, the methane content in biogas increases to 70-76%, but the biogas yield is lower and is 4.577 l/(h·kg DOM) at 36% post-alcohol distillery waste content in the substrate, 3.294 l/(h·kg DOM) at 27%, 2.960 l/(h·kg DOM) at 18%, 1.538 l/(h·kg DOM) at 9%. The optimum content of post-alcohol distillery waste in the substrate, at which the biomethane yield will be maximum (3.821 l/(h·kg DOM)), is 46.7% of the substrate content and 100% of the organic part of the substrate. The results of this study can be used in planning the composition of the substrate of biogas plants and designing and building new biogas plants near distilleries

Keywords: biomethane; biogas plant; digester; fermenter; bioreactor; digester

INTRODUCTION

For biogas production, the main substrate is traditionally cow manure, which already contains methane-producing bacteria and has an optimal C/N ratio (Rogovskii *et al.*, 2020). However, the biogas yield from the anaerobic methane destruction of cow manure is relatively low. Therefore, to increase the biogas yield from livestock by-products, substrates are used – waste from processing and agricultural production. This eliminates the need for their disposal. Such concentrates include vegetable oil sludge, granulated straw, substandard flour, and biodiesel production waste: crude glycerine – a by-product of biodiesel production, and soap stock – a by-product of biodiesel neutralisation. However, these co-substrates cannot undergo anaerobic methane degradation on their own, so biogas plants are often limited to corn silage, poultry manure, pig manure and cattle manure as feedstock. One of the co-substrates for biogas production, which can also undergo mono-degradation, is post-alcohol distillery waste.

Article's History: Received: 05/01/2023; Revised: 31/03/2023; Accepted: 26/04/2023.

Suggested Citation:
Polishchuk, V., & Valiev, T. (2023). Study of the anaerobic destruction of post-alcohol distillery waste by mateen. *Machinery & Energetics,* 14(2), 60-69. doi: 10.31548/machinery/2.2023.60.

*Corresponding author

Post-alcohol distillery waste is the final by-product of brew distillation in the production of ethanol from sugar and starch crops or cellulosic material. E. Carrilho *et al.* (2016), I. Syaichurrozi (2016) determined that it consists of 93% water and 7% solids. For every litre of ethanol produced in the sugar industry, 15 litres of distillery waste can be produced. This residue contains high levels of salt and organic matter and has a low pH. Every year, 22.4 gigalitres of post-alcohol distillery waste are produced worldwide (Parsaee *et al.*, 2019). As argued by A.M. Rosales *et al.* (2022), it is an environmental pollutant that is difficult to dispose of. It is disposed of in filtration fields, but there is an unpleasant odour in the vicinity of filtration fields. Disposal of post-alcohol distillery waste in soils and water bodies causes serious environmental problems, mainly due to soil salinity and changes in pH.

The post-alcohol distillery waste can be utilised by processing it into biogas, with no foul odour from distillery waste decomposition and the resulting biogas being an energy-valuable product.

The anaerobic methane degradation of post-alcohol distillery wastes can generate significant amounts of biogas that can be used for electricity or biomethane production. Biomethane can be injected into the natural gas network or used as a substitute for petroleum fuels (Neto *et al.*, 2019).

Nevertheless, following G. Kulichkova *et al.* (2020), post-alcohol distillery waste has a low carbon-to-nitrogen ratio. Therefore, additional substances, such as animal manure, organic industrial waste, and lime fertilisers, should be added to increase the biogas yield. R. Yuliasni *et al.* (2021) concluded that post-alcohol sugarcane distillery waste has an acidic pH (3.5-5.0) and a high concentration of sulphuric acid (over 150 mg/l).

G. Kulichkova (2022) argued that the thickened distillery waste obtained after sugar beet alcohol production is more suitable for anaerobic methane degradation than liquid distillery waste.

A. Calvo *et al.* (2019) investigated the co-digestion of anaerobic methane degradation of post-alcohol sugarcane distillery waste with sludge from oxidation and cooling lagoon. A concentration of 90% of the distillery waste was found to give the highest yield (674.5 ml of biogas over 18 days in a 400 ml working volume). N. Golub *et al.* (2019) describe the results of a study of the one-stage combined anaerobic methane destruction of post-alcohol distillery waste and poultry manure in a dry organic matter (DOM) ratio of 1:1.7. To ensure the utilisation of the post-alcohol distillery waste, one-sixth of the reactor volume was replaced daily with post-alcohol distillery waste with a pH of 3.7, without adding new portions of poultry manure. The research has shown that a ratio of dry organic material of poultry manure to post-alcohol distillery waste of less than 1:1 leads to a decrease in biogas yield and methane content. Periodic daily replacement of the fermented part of the substrate with post-alcohol distillery waste without disturbing the stabilisation of the process is possible at a pH value of at least 6.5. Manure utilisation leads to the establishment of a steady state after 20 days, which is maintained for at least 10 days. In the work of K. Jaman *et al.* (2023) studied the co-degradation of cow manure and molasses distillery waste at different ratios and changes in the organic load rate (OLR). The studies were conducted from OLR 1 g/l/day to OLR 7 g/l/day. At OLR of 7 g/l/day, signs of methanogen inhibition began to appear. The optimal OLR was found to be 5 g/l/day. At the same time, the biomethane yield was 1.24 l/g volatile solids (VS). In this case, the best model of biomethane yield was the first-order model with a determination coefficient of $R^2 = 0.94035$.

Thus, the literature review shows that post-distillation distillery waste can be used for biogas production. However, it is acidic and contains chemicals (molasses distillery waste, sugar cane distillery waste – sulphuric acid salts, sulphates) that are added to the mash in the process of ethanol production from sugar-containing raw materials and remain in the post-distillation distillery waste. These chemicals cause inhibition of methane-forming bacteria, making methane formation impossible, so it is recommended to add molasses distillery waste to the substrate in small amounts, diluting it with water. However, the reviewed literature does not mention how anaerobic methane destruction of post-alcohol distillery waste is carried out without the presence of harmful impurities.

The research aims to determine the optimal amount of post-alcohol distillery waste in a substrate based on cow manure to obtain maximum biomethane yield.

MATERIALS AND METHODS

The influence of post-alcohol distillery waste on biomethane generation was studied at a laboratory biogas plant at the National University of Life and Environmental Sciences of Ukraine (Fig. 1), which consists of a 30-litre fermenter and a gas holder.

Figure 1. Laboratory biogas installation
Source: compiled by the authors

The dynamics of the biomethane yield rate were carried out under the periodic mode of fermenter loading during the mono-degradation of cow manure, during the mono-degradation of post-alcohol distillery waste and the combined anaerobic destruction of cow manure and post-alcohol distillery waste in different proportions. The content of substrate components in the study of biogas yield dynamics is given in Table 1.

Table 1. Content of substrate components in the study of biogas yield dynamics

The content of the post-alcohol distillery waste to:		Substrate components, kg		
substrate contents, %	water organic matter percentage in the substrate, %	water	post-alcohol distillery waste	cow manure
0	0	4.5	0	3.5
9	20	4.5	0.7	2.8
18	40	4.5	1.4	2.1
27	60	4.5	2.1	1.4
36	80	4.5	2.8	0.7
47	100	4.5	3.5	0

Source: compiled by the authors

A total of 8.0 kg of substrate was loaded. The temperature mode of the digester during the study was 40 ± 0.5°C and was set using a TRC02 "Universal" thermostat manufactured by the Zhytomyr plant "Promprylad" (Ukraine). The biomethane content in biogas was determined by a GEM-500 gas analyser manufactured by LANDTEC (USA). The post-alcohol distillery waste had a pH of 4.8, which was determined by a pH meter PH-009 manufactured by Kelilong Electron (China).

The graphical dependences of the dynamics of biogas and biomethane yields, and accumulated biogas and biomethane yields over time were constructed on a computer using the EXCEL spreadsheet processor. The analytical model of the maximum biomethane yield during anaerobic methane destruction of the substrate with different content of post-alcohol distillery waste was obtained by approximating the maximum biomethane yield on a computer using the EXCEL spreadsheet processor at different content of the organic part of the post-alcohol distillery waste in the substrate.

The coefficient of determination (Foerster & Roenz, 1979) was used to assess the extent to which the regression function is described by the determinants:

$$R^2 = 1 - \frac{\sigma_z^2}{\sigma^2}, \quad (1)$$

where R^2 – determination coefficient; where σ^2 – general dispersion; σ_z^2 – remaining (group internal) dispersion.

The general dispersion is determined by the formula (Foerster & Roenz, 1979):

$$\sigma^2 = \sum_i (y_i - \bar{y})^2, \quad (2)$$

where y_i – actual values of time series levels; $\bar{y}$ – arithmetic mean of the actual values of the time series levels.

The remaining dispersion is determined by the formula (Foerster & Roenz, 1979):

$$\sigma_z^2 = \sum_i (y_i - \hat{y}_i)^2, \quad (3)$$

where $\hat{y}_i$ – estimated values of the time series levels obtained by the approximated expression.

The higher the coefficient of determination R^2 is close to one, the better the regression is defined.

To make a statistical conclusion about the presence or absence of a correlation between the variables under study, it is necessary to check the significance of the coefficient of determination. Since the reliability of statistical characteristics, including the coefficient of determination, depends on the sample size, a situation may arise when the value of the coefficient of determination is entirely due to random fluctuations in the sample based on which it is calculated. The significance of the paired coefficient of determination is assessed by Fisher's criterion (Foerster & Roenz, 1979):

$$F = \frac{R^2 \cdot (n-2)}{1-R^2}, \quad (4)$$

where F – Fisher's criterion; R^2 – determination coefficient; n – measurements, pcs.

The value of Fisher's criterion calculated by formula (4) was compared with the critical values of Fisher's criterion given in (Foerster & Roenz, 1979) at a given level of significance and the corresponding number of degrees of freedom. If $F > F_{cr}$, then the calculated coefficient of determination is significantly different from zero. This conclusion is ensured with a probability of 1-α. The determination of the coefficient of determination and Fisher's test was carried out on a computer using the EXCEL spreadsheet processor.

By studying the function $w_{bm} = f(Vin)$ for the extremum $w_{bm} \rightarrow max$, the optimal content of post-alcohol distillery waste in the substrate was determined, at which the biomethane yield would be maximised. The study of the function $w_{bm} = f(Vin)$ for the extremum $w_{bm} \rightarrow max$ was carried out on a computer in MATHCAD using the built-in optimisation function Maximize, which includes the algorithm of the "gradient descent" method.

RESULTS AND DISCUSSION

The dynamics of biogas yields from anaerobic mono-degradation of cow manure, anaerobic mono-degradation of post-alcohol distillery waste and combined anaerobic methane degradation of cow manure and post-alcohol distillery waste in different proportions are shown in Figure 2.

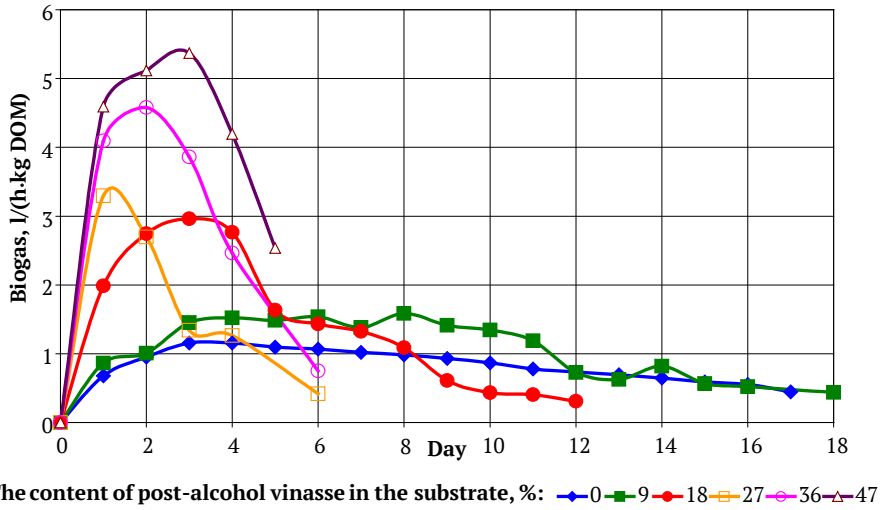

Figure 2. The dynamics of biogas yields from anaerobic mono-degradation of cow manure, anaerobic mono-degradation of post-alcohol distillery waste and combined anaerobic methane degradation of cow manure and post-alcohol distillery waste in different proportions

Source: compiled by the authors

As can be seen from Figure 2, the dynamics of biogas yield correspond to all phases of microbial development. Initially, a logarithmic phase is observed when anaerobes, in the presence of a nutrient medium (freshly added substrate to the digester), actively multiply, producing more and more of their vital product – biogas. The logarithmic phase gradually turns into a short stationary phase, when the number of anaerobes is in dynamic equilibrium with the availability of nutrients. At this time, the maximum biogas yield is observed. After that, the substrate nutrients begin to be depleted due to their active consumption by the anaerobic biomass, which has grown to a significant size. The active reproduction of anaerobes stops, and their gradual death begins due to a lack of nutrients in the substrate. The phase of dying off begins. At the same time, the biogas yield gradually decreases. Both during the anaerobic mono-degradation of cow manure, anaerobic mono-degradation of post-alcohol distillery waste, and combined anaerobic methane degradation of cow manure and post-alcohol distillery waste in different proportions, the phase of anaerobes getting used to a new substrate (lag phase) was not observed. No diauxia was observed, which is typical for multicomponent substrates, when methane-forming bacteria first consume one, in their opinion, the most palatable component of the substrate. After its exhaustion, methanogens switch to another component of the substrate. In this case, there are two peaks of maximum biogas yield, i.e., two stationary phases (Malinin *et al.*, 2021).

Moreover, with the increase of post-alcohol distillery waste content in the substrate, the duration of the logarithmic phase and the die-off phase decreases, resulting in a shorter period of anaerobic methane destruction. Thus, if the maximum biogas yield at 18%, 27%, and 36% of the post-alcohol distillery waste content in the substrate and during the mono-degradation of post-alcohol distillery waste is observed on day 2-3 of anaerobic methane destruction, at 9% of the post-alcohol distillery waste content in the substrate and during the mono-degradation of cow manure – on day 4-8.

At the same time, the maximum biogas yield increases with the increase in the content of post-alcohol distillery waste in the substrate. Thus, during the mono-degradation of cow manure, the maximum biogas yield is 1.157 l/(h·kg DOM), with the content of post-alcohol distillery waste in the substrate of 9% – 1.538 l/(h·kg DOM), at 18% – 2·960 l/(h·kg DOM), at 27% – 3.294 l/(h·kg DOM), at 36% – 4.577 l/(h·kg DOM). The maximum biogas yield of the post-alcohol distillery waste is 5.369 l/(h·kg DOM), which is 4.6 times higher than the maximum biogas yield of cow manure mono-digestion.

Accumulated biogas output yields from anaerobic mono-degradation of cow manure, anaerobic mono-degradation of post-alcohol distillery waste and combined anaerobic methane degradation of cow manure and post-alcohol distillery waste in different proportions are shown in Figure 3.

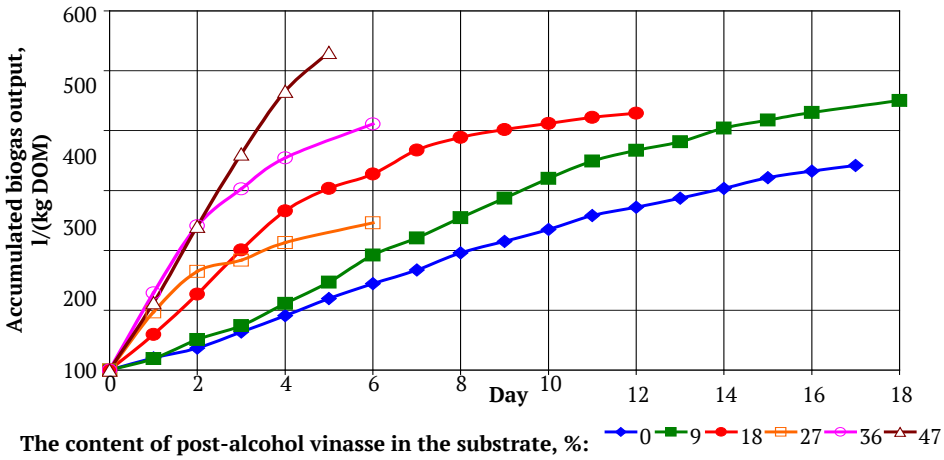

Figure 3. Accumulated biogas output yields from anaerobic mono-degradation of cow manure, anaerobic mono-degradation of post-alcohol distillery waste and combined anaerobic methane degradation of cow manure and post-alcohol distillery waste in different proportions

Source: compiled by the authors

Figure 3 shows that with an increase in the content of post-alcohol distillery waste in the substrate, the slope of the curve of the accumulated biogas yield increases, which indicates a more intensive biogas yield. Thus, already on the fifth day, the accumulated biogas yield during the mono-degradation of post-alcohol distillery waste is 530.6 l/(kg DOM), with the content of post-alcohol distillery waste in the substrate of 9% – 382.8 l/(kg DOM), 18% – 303.3 l/(kg DOM), 27% – 229.6 l/(kg DOM), 36% – 146.9 l/(kg DOM), and with the mono-degradation of cow manure – 119.4 l/(kg DOM). The accumulated biogas yield on the fifth day of mono-degradation of post-alcohol distillery waste is higher than the accumulated biogas yield on the 18th day of mono-degradation of cow manure.

The methane content in biogas produced during anaerobic methane destruction of the substrate with 9% and 18% post-alcohol distillery waste on the first day of anaerobic methane destruction is insignificant (biogas does not burn), and a persistent hydrogen sulphide smell is felt. On the second day of anaerobic methane digestion, the methane content in biogas increases to 65%, and on the next day and subsequently stabilises at 70-72%. With the content of post-alcohol distillery waste in the substrate of 27% and 36% on the first day of anaerobic methane digestion, the methane content in biogas is 58-60% and subsequently increases to 74-76%. During anaerobic methane digestion of the substrate without cow manure (post-alcohol distillery waste content 46.7%), the methane content in biogas from the first day ranges from 66-68%. The methane content in biogas during the mono-degradation of cow manure without the addition of post-alcohol distillery waste is lower than when using post-alcohol distillery waste and is in the range of 48-52%.

The dynamics of biomethane yields from anaerobic mono-degradation of cow manure, anaerobic mono-degradation of post-alcohol distillery waste and combined anaerobic methane degradation of cow manure and post-alcohol distillery waste in different proportions are shown in Figure 4 (Bulhakova, 2022).

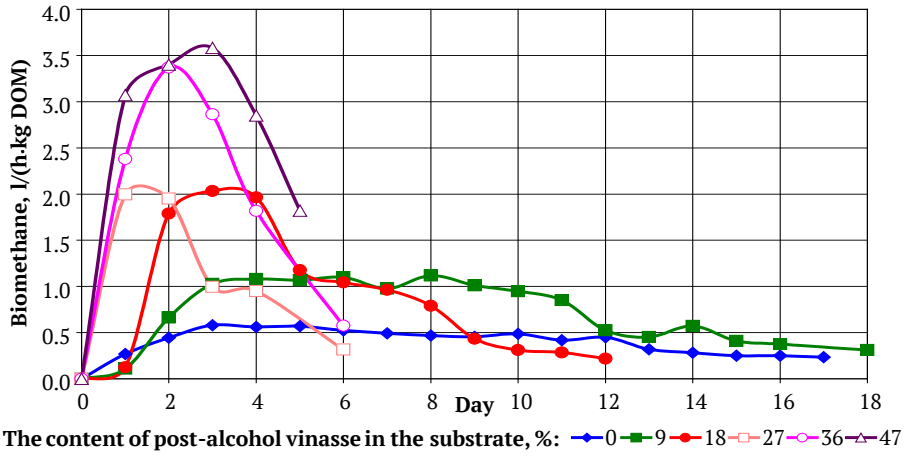

Figure 4. The dynamics of biomethane yields from anaerobic mono-degradation of cow manure, anaerobic mono-degradation of post-alcohol distillery waste and combined anaerobic methane degradation of cow manure and post-alcohol distillery waste in different proportions

Source: compiled by the authors

The maximum biomethane yield during anaerobic mono-degradation of cow manure is 0.58 l/(h·kg DOM), during the combined anaerobic methane degradation of cow manure and post-alcohol distillery waste at the content of post-alcohol distillery waste to the substrate of 9% – 1. 118 l/(h·kg DOM), 18% – 2.033 l/(h·kg DOM), 27% – 1.997 l/(h·kg DOM), 36% – 3.371 l/(h·kg DOM), with anaerobic mono-destruction of post-alcohol distillery waste – 3.582 l/(h·kg DOM).

The maximum biomethane yield during anaerobic mono-degradation of post-alcohol distillery waste and combined anaerobic methane degradation of cow manure and post-alcohol distillery waste (18%, 27% and 36%) is observed already on day 1-3 of methane fermentation, while during combined anaerobic methane degradation of cow manure and 9% of post-alcohol distillery waste – on day 8.

Accumulated biomethane output yields from anaerobic mono-degradation of cow manure, anaerobic mono-degradation of post-alcohol distillery waste and combined anaerobic methane degradation of cow manure and post-alcohol distillery waste in different proportions are shown in Figure 5.

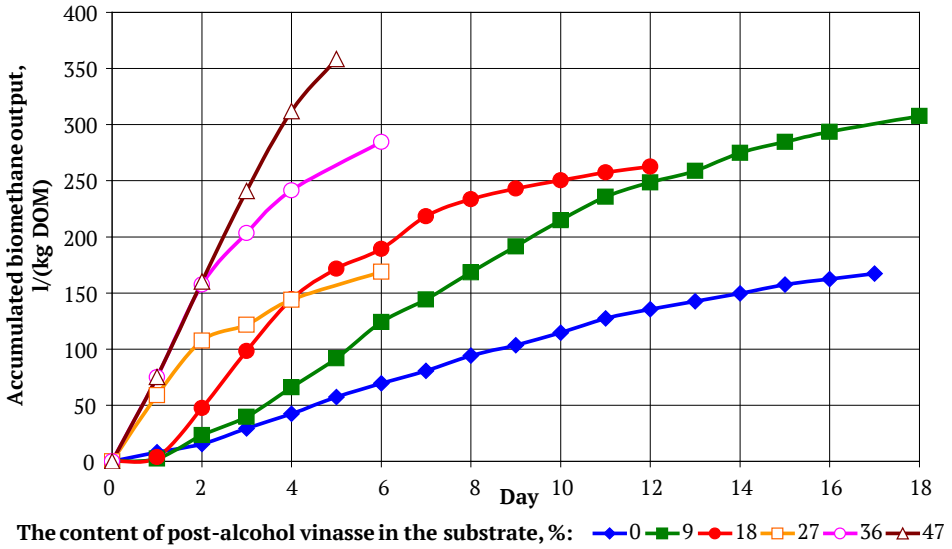

Figure 5. Accumulated biomethane output yields from anaerobic mono-degradation of cow manure, anaerobic mono-degradation of post-alcohol distillery waste and combined anaerobic methane degradation of cow manure and post-alcohol distillery waste in different proportions

Source: compiled by the authors

Figure 5 shows that the curves of the accumulated biomethane yields follow the curves of the accumulated biogas yields. The only difference between them is that the biomethane yield is lower than the biogas yield per biomethane content in the biogas and that at the initial stage of anaerobic methane degradation at a certain content of post-alcohol distillery waste in the substrate, biogas does not contain methane, so some curves of the accumulated biomethane yield start to grow from the next day after the start of anaerobic methane degradation.

The fermenter of the biogas plant, where experimental studies of anaerobic destruction of substrates based on cow manure with the addition of post-alcohol distillery waste were carried out, is suitable for batch loading of the substrate. At the same time, due to the peculiarities of biogas yield during batch loading of the substrate, when the biogas yield increases sharply to the maximum and then decreases, it is impossible to obtain the maximum biogas yield for a rather significant period. Therefore, industrial biogas plants use a semi-continuous mode of fermenter loading, when the substrate is added in small portions over a short period (about 10 minutes). In this case, the constant biogas yield with a semi-continuous fermenter loading system used in industrial bioreactors will be close to the maximum biomethane yield with a batch loading system (Polishchuk *et al.*, 2021). Therefore, based on the data of the maximum biogas yield with batch loading of the substrate into the fermenter, a model of constant biogas yield with a semi-continuous mode of substrate loading into the fermenter used in industrial biogas plants can be obtained.

The maximum biomethane yield during the anaerobic methane degradation of a substrate with different post-alcohol distillery waste content is shown in Figure 6.

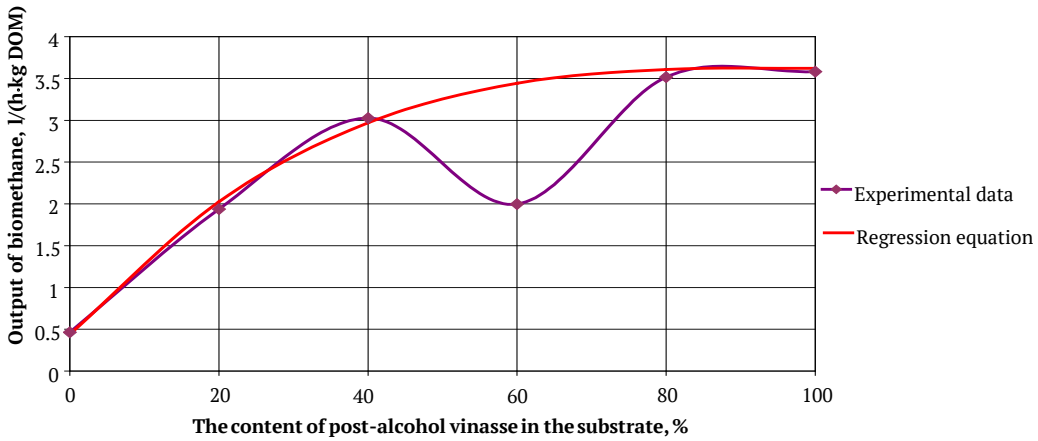

Figure 6. The maximum biomethane yield during the anaerobic methane degradation of a substrate with different post-alcohol distillery waste content

Source: compiled by the authors

The modelled biomethane yield rate can be represented as a third-order Newtonian polynomial:

$$w_{bm} = 0.0000036 \cdot Vin^3 - 0.001 \cdot Vin^2 + 0.0978 \cdot Vin + 0.4412, \quad (5)$$

where w_{bm} – is the biomethane yield rate, l/(h·kg DOM); Vin – is the content of post-alcohol distillery waste in the substrate, %.

The coefficient of determination of expression (5) is 0.7445 due to the loss of the biomethane yield point at 60% of the post-alcohol distillery waste content in the substrate from the overall process dynamics.

The significance of the coefficient of determination of the function $w_{bm} = f(Vin)$ according to Fisher's criterion (Fisher's calculated criterion is 11.7, Fisher's critical criterion at $\alpha = 5\%$ – 225 (Foerster & Roenz, 1979)).

When studying the function $w_{bm} = f(Vin)$ for the extremum $w_{bm} \rightarrow max$ using the gradient descent method, the optimal content of post-alcohol distillery waste in the substrate at which the biomethane yield will be maximum (3.821 l/(h·kg DOM)) was found to be $Vin = 46.7\%$.

Thus, this study shows that post-alcohol distillery waste can be successfully subjected to anaerobic methane degradation both without and with the addition of other substrates (in this case, cow manure). The highest biomethane yield is achieved during the mono-degradation of the post-alcohol distillery waste and is 3.582 l/(h·kg DOM), or 86 l/kg DOM per day. This daily biomethane yield can be achieved in a quasi-continuous mode of digester loading (used in large industrial biogas plants) when small portions of the fresh substrate are fed into the digester continuously at short intervals (from 10 minutes to 1 hour). When the substrate is periodically loaded into the digester, the biomethane yield is lower. Thus, during the mono-fermentation of post-alcohol distillery waste, the average biomethane yield during 5 days of anaerobic methane destruction (it is irrational to subject this substrate to destruction for more time since the biomethane yield decreases sharply) is 2.939 l/(h·kg DOM), or 71 l/kg DOM per day, or 355 l/kg DOM per day for the entire fermentation period (5 days). Taking into account that the DOM content in the DM of the post-alcohol distillery waste is 5%, the biomethane yield from the mono-degradation of the post-alcohol distillery waste in the batch mode of loading is 187 l/kg DM for the entire fermentation period, which is slightly lower than the result obtained by J.C. de Carvalho *et al.* (2023), which is 215-324 l/kg DM during the anaerobic methane degradation of post-alcohol distillery waste, and S.S. Hashemi *et al.* (2022) – 425 ml/g VS during the anaerobic methane degradation of the substrate in the ratio of post-alcohol distillery waste to whey 25:75, which was used for cultivation of fungi at pH = 6.5. At the same time, J.C. de Carvalho *et al.* (2023) and S.S. Hashemi *et al.* (2022) do not specify the time to which the results refer. As for the quasi-continuous mode of the digester loading, the biogas yields reported in these works can be achieved on the 3-5th day of anaerobic methane degradation, while the HRT for a digester is usually taken at the level of 20-25 days. However, our results are close to the results (380 ± 20 cm^3/g DOM, methane content in biogas – 70 ± 2%) obtained in N. Golub & M. Potapova (2018), where the co-digestion of anaerobic methane degradation of wastewater, post-alcohol distillery waste and poultry manure in a ratio of 0.2:1:7 in a two-stage mode was studied. N. Golub & M. Potapova (2018) noted that the problem of anaerobic methane destruction of post-alcohol distillery waste in its pure form is its low pH and insufficient content of nitrogen compounds, which are necessary for the development of microorganisms-destructors and producers of methane. It is to neutralise these problems that methane destruction was carried out in conjunction with poultry manure. To maximise the conversion of pollutants into biogas, the liquid fraction is fermented in a second fermenter after the solid residue is separated. The concentration of dry organic urea in the first reactor did not exceed 10%, the temperature of the reactor was 40 ± 2°C, the stirring speed was 100 rpm, and the final pH of the substrate – 7.0 ± 0.5.

The methane content in biogas during the mono-destruction of the post-alcohol distillery waste is in the range of 48-52%, which is lower than the value of 77% for the hydraulic retention time (HRT) of 21 days reported by S. Belhamidi *et al.* (2021), but correlates with the methane content in biogas (42.89-58.06%) reported by I. Utami *et al.* (2016) and 57.21% reported by N. Harihastuti *et al.* (2020) and 50-55% during the anaerobic methane degradation of post-alcohol distillery waste from the production of miscal (an alcoholic beverage obtained by distillation of fermented agave sucrose) in combination with activated sludge in a ratio of 3: 7 (Santos *et al.*, 2019). The obtained methane content in biogas from anaerobic methane digestion of post-alcohol distillery waste and cow dung substrate is 70-76%, which correlates with 70% methane in biogas from anaerobic methane digestion of post-alcohol distillery waste and cow dung substrate at a hydraulic retention time of 20 days, as reported in C.E. de Farias Silva & A.K. de Souza Abud (2017), and 81% for anaerobic methane digestion of a substrate consisting of post-alcohol distillery waste from the production of miscal and cow manure, as reported by L.V. Santos *et al.* (2020). Thus, based on our research and comparison with the results reported in the literature, it can be stated that the methane content of biogas is lower in the case of mono-degradation of post-alcohol distillery waste than in the case of combined anaerobic methane degradation of post-alcohol distillery waste with cow manure.

The results differ significantly from the conclusions presented by W. Romaniuk *et al.* (2022), which state that anaerobic mono-degradation of molasses distillery waste yields significant biogas, but it contains almost no methane and consists mainly of carbon dioxide. Only when cow manure is added to the substrate in large quantities does methane appear in the biogas and the lower calorific value of biogas reaches 16.5-20.5 MJ/m^3. This difference can be explained by the peculiarities of the ethanol production technology from molasses distillery waste when sulphuric acid is required. As a result, sulphuric acid salts are formed – sulphites, which harm methane formation during molasses biodegradation. The addition of cow manure to the substrate significantly improves the biodegradation process with methane production. By the way, as noted in A. Calvo *et al.* (2019), the same problem as in the biodegradation of molasses distillery waste is observed in the biodegradation of post-alcohol distillery waste from sugar cane.

C.R. Tunes *et al.* (2016) found that the biogas yield from post-alcohol sugarcane distillery waste in an 87-litre reactor over 15 days was 1160 litres with a methane concentration of 48-57%. B. Budiyono *et al.* (2013) modelled the biogas yield from anaerobic methane degradation of post-alcohol distillery waste according to the Gompertz model. The maximum biogas yield according to this model is 83.982 ml/(kg DOM).

In general, cow manure is considered to be an ideal substrate for anaerobic methane fermentation, but, unfortunately, the yield of biogas, and, accordingly, biomethane, is low. Thus, the study of the efficiency of biomethane production using anaerobic methane destruction of cow manure and post-alcohol distillery waste with different content showed a reduction in the period of biomethane production with an increase in the content of post-alcohol distillery waste

CONCLUSIONS

In the case of combined anaerobic methane destruction of cow manure and post-alcohol distillery waste with periodic loading of the digester with an increase in the content of post-alcohol distillery waste, the effective period of biomethane production is reduced. If the effective period of biomethane production is 10-12 days with a post-alcohol distillery waste content of 9%, then with a post-alcohol distillery waste content of more than 9%, it is reduced to 4-5 days, after which the biomethane yield decreases significantly.

With an increase in the content of post-alcohol distillery waste in the substrate, the maximum biomethane yield increases and exceeds the biogas yield from cow manure mono-degradation by 4 times at a post-alcohol distillery waste content of 9%, and by 6-7 times at a post-grain distillery waste content of more than 9%.

The modelling of the constant biomethane yield at quasi-continuous substrate loading into the digester was carried out based on studies of the maximum biomethane yield at periodic substrate loading. The dependence of biomethane yield on the content of post-alcohol distillery waste in the substrate is described by a third-order Newton polynomial with a determination coefficient of 0.7445. As a result of studying this dependence at the extremes, it was found that the optimal way to obtain the maximum biomethane yield is to use anaerobic mono-destruction of post-alcohol distillery waste. In this case, the biogas yield will be 3.821 l/(h·kg DOM).

Mathematical models of the digester functioning during the anaerobic mono-degradation of post-alcohol distillery waste and the combined anaerobic methane degradation of cow manure and post-alcohol distillery waste are planned to be developed in the future. These models will describe the dynamics of changes in the concentration of nutrients in the substrate, the concentration of methane-forming bacteria biomass (considering the growth of the methanogen population according to the Mono equation and their death according to the Kolpikov equation) and biogas generation depending on different concentrations and modes of loading the digester. These mathematical models will be compared with the results of experimental studies and, if deviations are found, the coefficients of the mathematical models will be adjusted.

ACKNOWLEDGEMENTS

None.

CONFLICT OF INTEREST

None.

REFERENCES

[1] Belhamidi, S., Elkhdime, H., Omar Elrhaouat, O., Sarra Kitanou, S., Taky, M., & Elmidaoui, A. (2021). Biogas production from vinasse derived from ethanol manufacturing using a continuous stirred tank reactor pilot plant. *Desalination and Water Treatment*, 240, 216-224. doi: 10.5004/dwt.2021.27763.

[2] Budiyono, B., Syaichurrozi, I., & Sumardiono, S. (2013). Biogas production kinetic from vinasse waste in batch mode anaerobic digestion. *Malaysian Journal of Science*, 32(2). 2-14. doi: 10.22452/mjs.vol32no2.1.

[3] Bulhakova, A. (2022). Mass spectrometric studies of valine molecules by electron shock in the gas phase. *Scientific Herald of Uzhhorod University. Series "Physics"*, 51, 9-17. doi: 10.54919/2415-8038.2022.51.9-17.

[4] Calvo, A., Ravelo, R., Cadavid, P., Andrés, C., & Jhoan, D. (2019). Biogas production evaluation and reduction of vinasse organic load by anaerobic digestion. *Revista Colombiana de Biotecnología*, 21(2), 118-130. doi: 10.15446/rev.colomb.biote.v21n2.79555.

[5] Carrilho, E.N.V.M., Labuto, G., & Kamogawa, M.Y. (2016). Destination of vinasse, a residue from alcohol industry: Resource recovery and prevention of pollution. *Environmental Materials and Waste Resource Recovery and Pollution Prevention*. 21-43. doi: 10.1016/B978-0-12-803837-6.00002-0.

[6] de Carvalho, J.C., de Souza Vandenberghe, L.P., Sydney, E.B., Karp, S.G., Magalhães, A.I., Martinez-Burgos, W.J., Medeiros, A.B.P., Thomaz-Soccol, V., Vieira, S., Letti, L.A.J., Rodrigues, C., Woiciechowski, A.L., & Soccol, C.R. (2023). Biomethane production from sugarcane vinasse in a circular economy: Developments and innovations. *Fermentation*, 9(4), article number 349. doi: 10.3390/fermentation9040349.

[7] de Farias Silva, C.E., & de Souza Abud, A.K. (2017). Influence of manure concentration as inoculum in anaerobic digestion of vinasse. *Acta Scientiarum. Biological Sciences*, 39(2), 173-180. doi: 10.4025/actascibiolsci.v39i2.34007.

[8] Foerster, E., & Roenz, B. (1979). *Methods of correlation and regression analysis*. Berlin: Verlag Die Wirtschaft.

[9] Golub, N., & Potapova, M. (2018). Technology of biogas production from distillery spent wash. *Scientific and Applied Journal Vidnovluvana Energetika*, 2(53), 70-78.

[10] Golub, N., Potapova, M., & Karpenko, Yu. (2019). Mathematical modeling of the biogas production process from the distillery spent wash on the first stage. *Scientific and Applied Journal Vidnovluvana energetika*, 3(2). 96-104. doi: 10.20535/ibb.2019.3.2.166429.

[11] Harihastuti, N., Yuliasni, R., Djayanti, S., Irnaning, H.N., Rame, R., & Prasetio, A. (2020). Hybrid Upflow-Anaerobic Filter (HU-AF) Integrated technology for bio-methane generation from vinasse with shorter hydraulic retention time. *E3S Web of Conferences,* 202, article number 10008. doi: 10.1051/e3sconf/202020210008.

[12] Hashemi, S.S, Karimi, K., & Taherzadeh, M.J. (2022). Valorization of vinasse and whey to protein and biogas through an environmental fungi-based biorefinery. *Journal of Environmental Management*, 303(5), article number 114138. doi: 10.1016/j.jenvman.2021.114138.

[13] Jaman, K., Idrus, S., Wahab, A.M.A., Harun, R.; Daud, N.N.N., Ahsan, A., Shams, S., & Uddin, M.A. (2023). Influence of molasses residue on treatment of cow manure in an anaerobic filter with perforated weed membrane and a conventional reactor: variations of organic loading and a machine learning application. *Membranes*, 13, article number 159. doi: 10.3390/ membranes13020159.

[14] Kulichkova, G. (2022). Comparative characteristics of native (liquid) and concentrated up to 40% vinasse as a raw material for anaerobic fermentation. *Eureka: Life Sciences*, 6, 25-35. doi: 10.21303/2504-5695.2022.002692.

[15] Kulichkova, G.I., Ivanova, T.S., Köttner, M., Volodko, O.I., Spivak, S.I., Tsygankov, S.P., & Blume, Ya.B. (2020). Plant feedstocks and their biogas production potentials. *The Open Agriculture Journal*, 14, 219-234. doi: 10.2174/1874331502014010219.

[16] Malinin, A.N., Molnar, K.B., & Malinina, A.O. (2021). Parameters of gas-discharge plasma of barrier discharge on mixtures of vapours of diiodide, dibromide and mercury dichloride with helium. *Scientific Herald of Uzhhorod University. Series "Physics"*, 50, 9-14.

[17] Neto, J.V.S., Gallo, W.L.R., & Nour, E.A.A. (2019). Production and use of biogas from vinasse: Implications for the energy balance and GHG emissions of sugar cane ethanol in the brazilian context. *Environmental Progress & Sustainable Energy*, 39(1), article number 13226. doi: 10.1002/ep.13226.

[18] Parsaee, M., Kiani Deh Kiani, M., & Karimi, K. (2019). A review of biogas production from sugarcane vinasse. *Biomass and Bioenergy*, 122, 117-125. doi: 10.1016/j.biombioe.2019.01.034.

[19] Polishchuk, V.M., Shvorov, S.A., Zablodskiy, M.M., Kucheruk, P.P., Davidenko, T.S., & Dvornyk, Ye.O. (2021). Effectiveness of adding extruded wheat straw to poultry manure to increase the rate of biogas yield. *Problemele Energeticii Regionale*, 3(51), 111-124. doi: 10.52254/1857-0070.2021.3-51.10.

[20] Rogovskii, I.L., Titova, L.L., Sivak, I.M., Vyhovskyi, A.Yu., Polishchuk, V.M., Drahnev, S.V., & Voinash, S.A. (2020). Study of biogas during fermentation of cattle manure using a stimulating additive in form of vegetable oil sediment. *ARPN Journal of Engineering and Applied Sciences*, 15(22), 2652-2663.

[21] Romaniuk, W., Rogovskii, I., Polishchuk, V., Titova, L., Borek, K., Shvorov, S., Roman, K., Solomka, O., Tarasenko, S., Didur, V., & Biletskii, V. (2022). Study of technological process of fermentation of molasses vinasse in biogas plants. *Processes*, 10(10), article number 2011. doi: 10.3390/pr10102011.

[22] Rosales, A.M., Montalvo-Romero, N., Santamaría, L.E.G., Herazo, L.G.S., Bautista-Santos, H., & Lambert, G.F. (2022). Post-industrial use of sugarcane ethanol vinasse: A systematic review. *Sustainability*, 14(18), article number 11635. doi: 10.3390/su141811635.

[23] Santos, L.V., Ramos, M.V., Morales, E.J.R., & Hensel, J.A. (2019). Inoculum adaptation for the anaerobic digestion of mezcal vinasse. *Revista Internacional de Contaminación Ambiental*, 35(2), 447-458. doi: 10.20937/rica.2019.35.02.15.

[24] Santos, L.V., Ramos, M.V., Morales, E.J.R., & Hensel, J.A. (2020). Effect of inoculum source on the anaerobic digestion of mezcal vinasse at different substrate-inoculum ratios. *Revista Internacional de Contaminación Ambiental,* 36(1), 81-95. doi: 10.20937/RICA.2020.36.53276.

[25] Syaichurrozi, I. (2016). Review – biogas technology to treat bioethanol vinasse. *Waste Technology*, 4(1), 16-23. doi: 10.12777/wastech.4.1.16-23.

[26] Tunes, C.R, de Morais, P.P., Caeser, A., Portella, F., De Souza Aguiar, R.W., da Silva, A.R., Bis, D.P., & Scheidt, G.N. (2016). Biogas production from anaerobic digestion of vinasse in upflow anaerobic sludge blanket reactor. *International Journal of Current Research*, 8(9), 38699-38703.

[27] Utami, I., Redjeki, S., Astuti, D.H., & Sani. (2016). Biogas production and removal COD – BOD and TSS from wastewater industrial alcohol (Vinasse) by modified UASB bioreactor. *MATEC Web of Conferences*, 58, article number 01005. doi: 10.1051/matecconf/20165801005.

[28] Yuliasni, R., Yuliastuti, R., & Setianingsih, N.I. (2021). Biogas production from sugarcane vinasse: A review. *Jurnal Riset Teknologi Pencegahan Pencemaran Industri*, 12(2), 34-44. doi: 10.21771/jrtppi.2021.v12.no2.p34-44.

Віктор МиколайовичПоліщук

Доктор технічних наук, професор
Національний університет біоресурсів і природокористування України
03041, вул. Героїв Оборони, 15, м. Київ, Україна
https://orcid.org/0000-0002-9654-9051

Тимур Одилович Валієв

Аспірант
Національний університет біоресурсів і природокористування України
03041, вул. Героїв Оборони, 15, м. Київ, Україна
https://orcid.org/0000-0003-3400-6147

Дослідження анаеробної матенової деструкції післяспиртової барди

Анотація. Післяспиртова барда є забруднювачем довкілля, тому проблема її утилізації є актуальною. Одним із способів утилізації післяспиртової барди є її анаеробна метанова деструкція на біогазових установках. Метою цього дослідження було визначити оптимальну кількість післяспиртової барди, яку необхідно додати до субстрату, щоб досягти максимального виходу біометану. Дослідження проводились на лабораторній біогазовій установці, яка складається із дайджестера обємом 30 л і газгольдера, в мезофільному режимі за температури субстрату 40°С при періодичному режимі завантаження субстрату. Встановлено, що найвищий вихід біогазу в 5.369 л/(год.·кг DOM) отримується при анаеробній метановій монодеструкції післяспиртової барди. Однак вміст метану в біогазі при цьому знаходитьсся в межах 48-52 %. При анаеробній метановій деструкції суміші післяспиртової барди з коров'ячим гноєм вміст метану в біогазі зростає до 70–76 %, однак вихід біогазу менший і становить: 4.577 л/(год.·кг DOM) при вмісті післяспиртової барди в субстраті 36 %, 3.294 л/(год.·кг DOM) – при 27 %, 2.960 л/(год.·кг DOM) – при 18 %, 1.538 л/(год.·кг DOM) – при 9 %. Оптимальний вміст післяспиртової барди в субстраті, при якому вихід біометану буде максимальним (3,821 л/(год.·кг DOM)), становить 46,7 % від вмісту субстрату і 100% від вмісту органічної частини субстрату. Результати даного дослідження можуть бути застосовані при плануванні складу субстрату біогазових установок, проєктуванні і будівництві нових біогазових установок поблизу спиртзаводів

Ключові слова: біометан; біогазова установка; метантенк; ферментатор; біореактор; дайджестер

Machinery & Energetics
Vol. 14, No. 2. 2023

Journal homepage:
https://technicalscience.com.ua/en

UDC 664.854:534.838.7
DOI: 10.31548/machinery/2.2023.70

Leonid Chervinsky*
Doctor of Technical Sciences, Professor
National University of Life and Environmental Sciences of Ukraine
03041, 15 Heroiv Oborony Str., Kyiv, Ukraine
https://orcid.org/0000-0001-7215-2474

Oleksandr Savoiskyi
Senior Lecturer
Sumy National Agrarian University
40021, 160 Gerasim Kondratyev Str., Sumy, Ukraine
https://orcid.org/0000-0002-6459-4931

Viktor Sirenko
PhD in Technical Sciences, Associate Professor
Sumy National Agrarian University
40021, 160 Gerasim Kondratyev Str., Sumy, Ukraine
https://orcid.org/0000-0003-0831-6563

The influence of ultrasonic processing on the structure and electrophysical properties of fruit in combined drying

Abstract. The intensification of ultrasonic vibrations for the processing of agricultural products is becoming increasingly important in the food industry, as it can reduce energy consumption for the dehydration of raw materials. The research aims to study the effect of sonication on the change of electrophysical parameters and structure of apple raw materials in the process of combined drying using direct electric heating. Using scanning electron microscopy, images of the surface structure of dried apple samples were obtained at different combinations of sonication duration and methods of heat supply to the raw material during the drying process. Based on the experimental studies, the dependences of the current flowing through the sample in the process of combined drying using direct electric heating on the duration of raw material processing in an ultrasonic bath were obtained. The influence of preliminary sonication on the maximum values of the current strength during direct electric heating was determined. The dependences of changes in the resistivity of apple samples during dehydration at different pretreatment durations were investigated. The effect of ultrasound on the initial resistivity of apples, the duration of electro-plasmolysis, and the resistivity values at which the maximum values of the direct electric heating current are observed were determined. The results of the experiments show that the pretreatment of raw materials in an ultrasonic bath can reduce the peak current values by up to 27%. The initial values of the resistivity of the raw material after sonication are reduced by 7.8-13.8% compared to the control samples. The obtained images of the dried fruit surfaces showed an increase in the porosity and roughness of the samples. The obtained results of experimental studies can become a prerequisite for the development of an energy-efficient technical means of ultrasonic processing of fruit and vegetable raw materials before drying and the selection of optimal operating modes

Keywords: raw apple; convective dehydration; direct electric heating; resistivity; scanning electron microscopy; roughness

Article's History: Received: 08/01/2023; Revised: 03/04/2023; Accepted: 26/04/2023.

Suggested Citation:
Chervinsky, L., Savoiskyi, O., & Sirenko, V. (2023). The influence of ultrasonic processing on the structure and electrophysical properties of fruit in combined drying. *Machinery & Energetics,* 14(2), 70-79. doi: 10.31548/machinery/1.2023.70.

*Corresponding author

INTRODUCTION

Vegetables and fruits are indispensable sources of useful vitamins and minerals necessary for the normal functioning of the human body. Due to their high moisture content (up to 90%), these products are very sensitive to temperature and spoil quickly, requiring them to be processed for long-term storage. According to V. Chandramohan (2020), drying is the easiest, cheapest, and least labour-intensive way to store fruits and vegetables.

The products obtained by this processing method are well stored, do not require special storage facilities and take up little space. In recent years, the development of technologies and equipment for the thermal dehydration of food products has focused on improving consumer properties by making production more complex, and high profitability is supported by marketing.

Drying units differ in the methods of heat supply to the dehydration object: convective (Carmeliet & Verboven, 2017), infrared (Huang *et al.*, 2021), high, ultra-high frequency currents (Zhou & Wang, 2019) and ultrasound (Fan *et al.*, 2017). A more innovative method of drying fruit and vegetable products is the freeze-drying method, which is described in S. Bhatta *et al.* (2020). All of these drying methods are based on the use of a clean form of energy – electricity. However, most of the proposed methods cannot provide an acceptable drying time for a given quality of the finished product. In addition, the specific energy consumption for the dehydration process is several times higher than the theoretical energy consumption for the evaporation of one kilogram of moisture.

Despite the numerous dehydration methods available today, drying remains the most energy-intensive stage of raw material processing. The quality and speed of the drying process largely determine the quality and cost of the final product. The research aims to reduce energy consumption for drying fruit and vegetable raw materials and improve the quality of the finished product.

The most common thermal method is the blanching of fresh raw materials in hot water. The authors (Guida *et al.*, 2013; Doymaz *et al.*, 2015) proved that immersion of products in hot water before drying reduces the duration of their dehydration, which is explained by an increase in the permeability of material cells as a result of high temperature. H. Xiao *et al.* (2017) found that thermal blanching also slightly improves the quality of the finished product by inactivating enzymes and microorganisms. At the same time, exposure to high temperatures can lead to discolouration of the finished product, loss of water-soluble and heat-sensitive vitamins and minerals.

An effective method of heat treatment is the preheating of raw materials by passing an alternating electric current through them. J. Moreno *et al.* (2013) and A. Isci *et al.* (2018) demonstrated the use of ohmic heating of raw materials before drying reduces the duration of dehydration by up to 30%. The reduction in drying time is caused by the damage and destruction of cell membranes as a result of electroplasmolysis. However, due to the significant heating of the raw material, the sample may boil. This leads to the destruction of the cell structure of the material and discolouration of the finished product.

According to J. Garcia-Noguera *et al.* (2012), due to the unique effects on agricultural products, low-frequency ultrasound waves are commonly used to intensify freezing, thawing, and drying processes.

J. Zubernik *et al.* (2018) noted that the use of ultrasound during the pretreatment of apples in an ethanol solution reduces the duration of convective dehydration by 18.3% compared to control samples. At the same time, an increase in the electrical conductivity of the solution was observed with an increase in the sonication time, which indicates the leakage of intracellular juice into the treated medium and a decrease in the number of nutrients in the finished product.

The research conducted by Z. Ren & Y. Bai (2018) showed the effectiveness of sonication of apple slices before vacuum freeze-drying. Pretreatment of the samples for 5 min in water at 25°C at an ultrasonic frequency of 100 kHz increased the drying rate by 25%. At the same time, increasing the processing time to 10 and 15 min did not improve the result or, on the contrary, worsened the rate of moisture removal from the samples. A.M. Jambrak *et al.* (2018) explained this behaviour by the possibility of closing surface pores during prolonged ultrasound application, which limits mass transfer. This situation can prevent the leakage of water-soluble solids from the intercellular space to the environment.

Studies of the electrophysical properties of raw materials after sonication show an ambiguous effect of ultrasound on the electrical conductivity of the material. Despite many studies on the preliminary sonication preceding the drying process, its effect on the electrophysical parameters and structure of dried raw materials is not well understood. The results of ultrasound exposure will vary depending on the type of raw material to be dried, methods of heat supply and technological parameters of the dehydration process.

The research primarily aims to obtain the dependences of changes in the electric current strength of direct electric heating and the resistivity of apple raw materials during dehydration, as well as to study the changes in the microstructure of dried apples under different processing modes in an ultrasonic bath.

MATERIALS AND METHODS

The research was conducted at Sumy National Agrarian University (Sumy, Ukraine). The objects of research were apples of early summer and summer ripening of the varieties “Red Mac”, “Mantet” and “Helios” grown in the Sumy region (Ukraine) and harvested in 2022.

The pre-prepared apples were cut into discs of 0.005 m height and 0.028 m diameter. Ultrasonic (US) treatment of the sliced apples before drying was carried out in an ultrasonic bath DSA 50-JY2 (China) according to the procedure provided by O. Savoiskyi *et al.* (2023). Then, the treated

samples were dried in a convection-type drying oven SNOL-2.5 (Ukraine) with additional heating by direct electric heating. The scheme of the drying unit and the drying methodology are given by O. Savoiskyi *et al.* (2021). During drying, the value of the electric current passing through the samples, their mass, and linear dimensions were recorded. Based on the measurements, the value of the current resistivity of the raw material during the drying process was calculated using the expression:

$$\rho = RS/l, \quad (1)$$

where ρ – current resistivity, Ohm·m; R – electrical resistance of the sample; Ohm, l – current length (height) of the sample, m, S – cross-sectional area, m^2. Statistica 12 (USA) was used to visualise the research results.

The methodology for studying the structure of dried fruit was as follows: samples pre-dried by various methods before sputtering the conductive film were dried in a drying oven to a constant weight at a temperature of 40°C. Complete removal of moisture from the samples before sputtering is a prerequisite, since, as a result of placing the latter in a working chamber with a high vacuum value, the moisture remaining in the sample begins to move from the inner layers to the surface and evaporate. This phenomenon negatively affects the quality of the sputtered conductive film, which further reduces the quality of the images obtained.

Subsequently, the dried samples were placed in the working chamber of the vacuum post-VUP-5 (VUP – vacuum universal post) (Ukraine), where an electrically conductive carbon film was sputtered onto their surface under a high vacuum (10^{-5} mmHg) (Fig. 1).

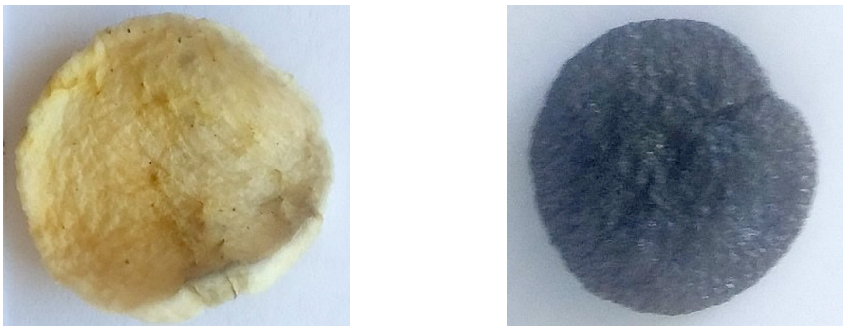

a) b)

Figure 1. The appearance of samples before and after carbon film deposition
Note: a – before sputtering; b – after sputtering

The electron microscopic examination of the surface of dried fruit samples was carried out using a REM-106I device (REM – scanning electron microscope, I – measuring) (Ukraine) (Fig. 2).

Figure 2. Scanning electron microscope REM-106I (Ukraine)

To create additional "bridges" of electrical conductivity, the sputtered samples were glued to the slide on carbon tape and placed in the working chamber of the microscope, where, after vacuum evacuation, the surface was scanned (Fig. 3).

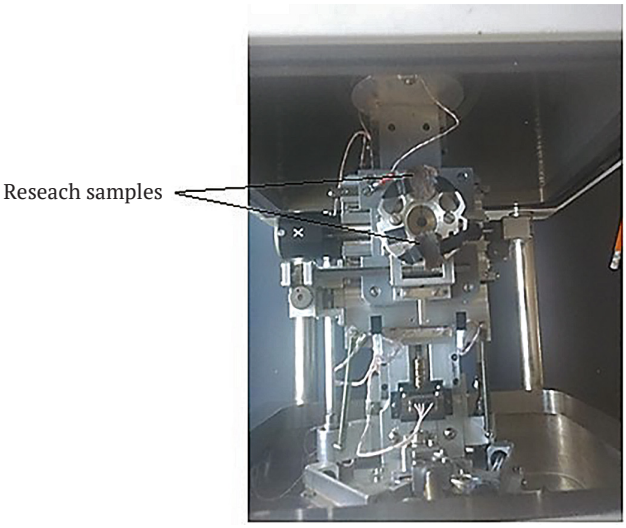

Figure 3. Vacuum chamber REM-106I (Ukraine) with the samples placed in it in action

The surface was scanned in the proprietary SELMI software environment, where the optimal scanning mode and magnification were selected.

The amount of heat energy supplied by direct electric heating during convective drying is primarily determined by the resistivity of the raw material and the amount of current flowing through the sample.

Direct electric heating dramatically changes the course of the dehydration process (Savoiskyi *et al.*, 2021). Drying by the proposed combined method can be divided into two main periods: a period of increasing and a period of decreasing drying rate. In this case, during the period of increasing drying rate, 30-35% of the moisture mass is removed, and the period of constant rate, which is characteristic of the convective dehydration process, is absent.

RESULTS AND DISCUSSION

Figures 4 and 5 show the results of experimental studies of the effect of sonication on the electrophysical characteristics of fruit in the process of combined drying using direct electric heating.

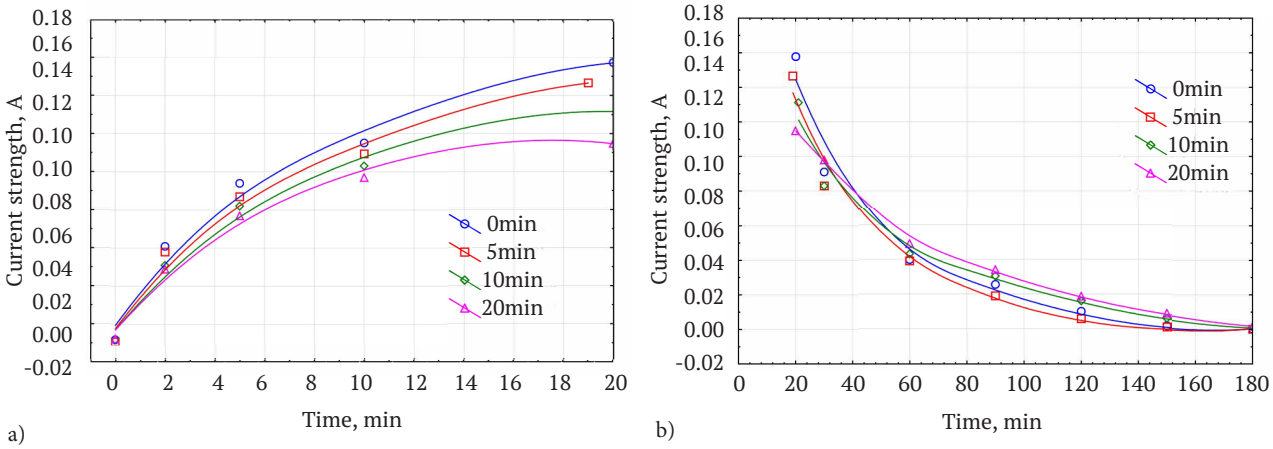

Figure 4. Dependences of the electric current strength passing through the sample during the drying process after sonication

Note: a – during the period of increasing drying rate, b – during the period of decreasing drying rate

Source: compiled by the authors

The main parameter that determines the quality of the finished product and the amount of energy consumed for moisture evaporation during drying by the proposed method is the magnitude of the electric current passing through the dried material. At the beginning of the drying process, when the fruit is heated by direct electric heating, the phenomenon of electro plasmolysis occurs, which is characterised by a constant increase in the strength of the electric current through the object (Fig. 4a). The increase in current is explained by a sharp decrease in the resistivity of the samples (Fig. 5a) due to irritation and destruction of cell membranes, resulting in the release of a significant amount of electrically conductive juice (Groza & Siddelev, 2022).

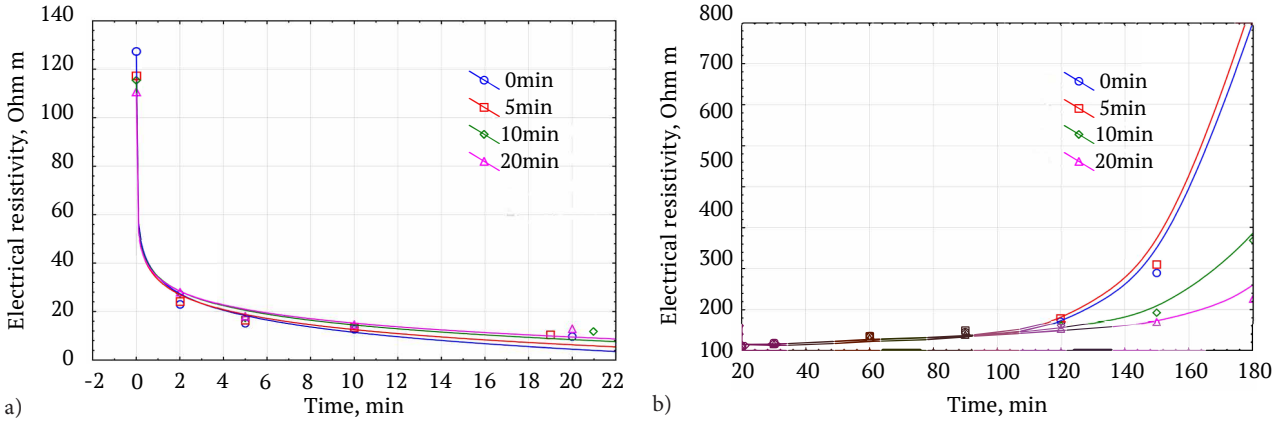

Figure 5. Dependences of the current fruit electric resistance during the drying process after sonication
Note: a – during the period of increasing drying rate; b – during the period of decreasing drying rate
Source: compiled by the authors

The obtained research results (Fig. 4) show that the pretreatment of raw materials in an ultrasonic bath before drying leads to a decrease in peak current values. The maximum value of the electric current that passed through the untreated samples during combined heating was 0.159 A. After sonication for 5 min, the maximum current during the drying process reached a value of 0.142 A.

Further increasing the sonication duration to 10 and 20 min reduced the maximum current values during the dehydration process to 0.131 and 0.116 A. Thus, increasing the sonication duration to 20 min reduced the maximum current through the sample by 27%.

The measurement of the resistivity of the raw material can be used to evaluate the efficiency of using direct electric heating during the drying process. The analysis of the results in Figure 5 shows that the sonication of fruit before drying leads to a reduction of its initial resistivity. The initial resistivity of the untreated fruit was about 127 Ohm-m (Fig. 5a). After treatment in an ultrasonic bath for 5 min, the initial resistance values decreased by 7.8% and amounted to 117 Ohm-m. Further increasing the duration of the ultrasonic treatment to 10 and 20 min reduced the initial resistivity values by 9.4 and 13.4% and amounted to 115 and 110 ohm-m, respectively. The obtained results confirm the data of A. Wiktor *et al.* (2016), showed that contact sonication for 5 min increased the electrical conductivity of the material by 57.7% compared to control samples. However, the effect of ultrasound on the electrical conductivity of tissues was ambiguous. Increasing the treatment duration to 20 min without changing the frequency reduced the electrical conductivity by 12% compared to the control samples. This can be explained by the phenomenon of pore closure in the material described by A.M. Jambrak *et al.* (2018).

The decrease in the electrical resistance of raw materials is explained by changes in the microstructure of fruit. Ultrasound causes leakage of the intracellular content of apple raw materials, which leads to an increase in free moisture in the samples and an improvement in the electrical conductivity of the material (Savoiskyi *et al.*, 2023). It should be noted that the decrease in electric current strength as a result of ultrasonic treatment has virtually no effect on the time of electro-plasticization of raw materials. In all cases, the duration of electroplasmolysis was up to 19-20 minutes. At the same time, the peak current values are reached at slightly higher values of the electrical resistance of the raw material, as can be seen in Figure 4a. This is due to the damage to the cell membranes by ultrasonic vibrations (ultrasonic cavitation), which reduces their current and thermal resistance.

After reaching the peak values, a gradual decrease in the strain force through the sample (Fig. 4b) is observed as a result of an increase in the specific electrical resistance of the raw material (Fig. 5b), which is explained by a decrease in the amount of moisture in the samples. When the critical moisture content is reached (140-150 min in Fig. 5b), there is a significant increase in the electrical resistance values, which may indicate the inappropriateness of using direct electric heating at this stage.

Figure 6 shows the results of the study of the surface structure of fruit at different processing times in an ultrasonic (US) bath, dried by different methods: convective (CK) and convective with direct electric heating (CK+ED).

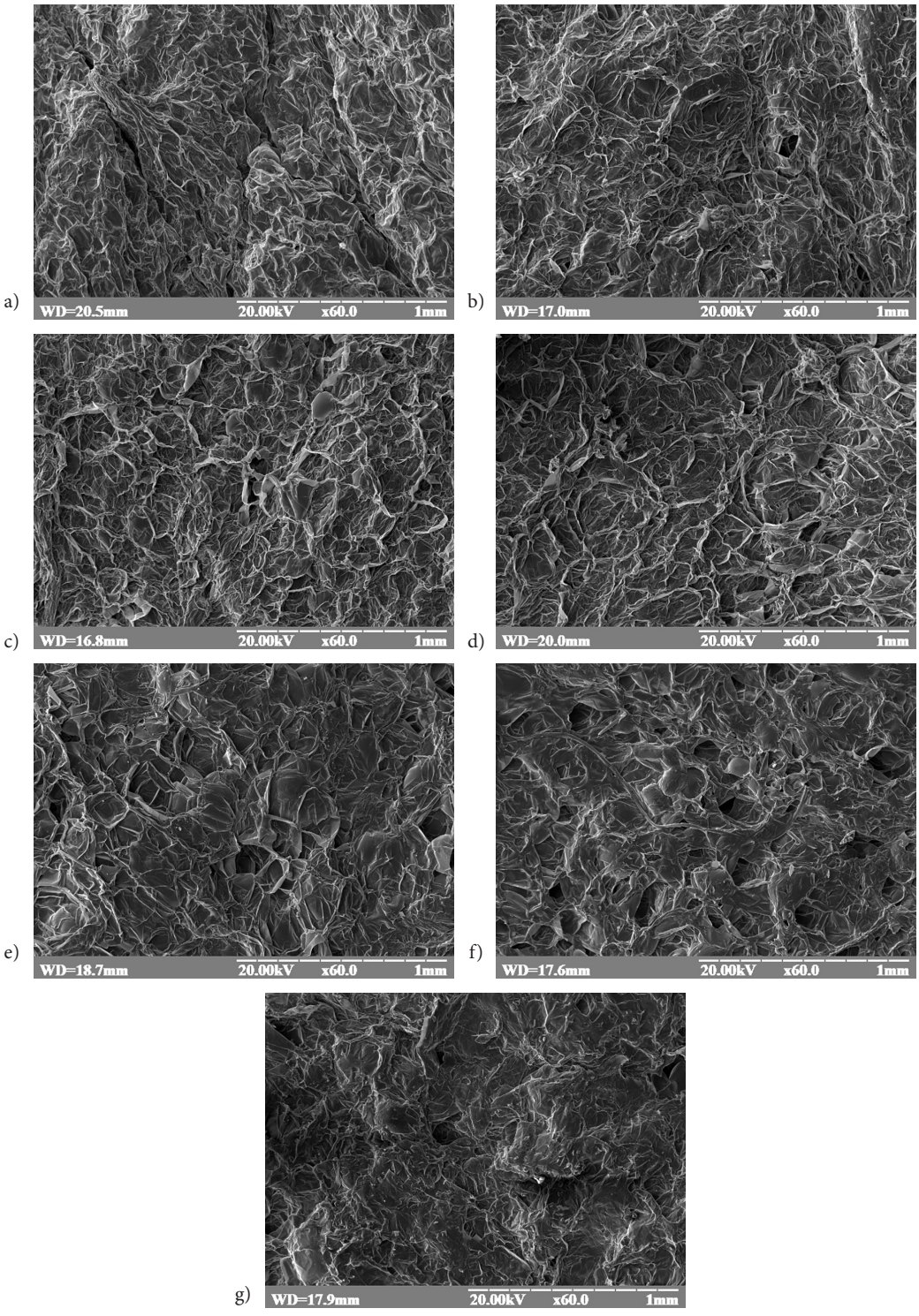

Figure 6. Images of dried fruit surfaces at different heat inputs and sonication duration
Note: a – CK; b – CK+US 5 m; c – CK+US 10 m; d – CK+US 20 m; e – CK+ED; f – CK+ED+US 5 m; g – CK+ED+US 20 m
Source: compiled by the authors

The use of ultrasonic treatment in the liquid before drying and direct electric heating during the dehydration process significantly reduces the final deformation of the finished product. The pieces produced in this way have a more regular shape and curl less during the drying process.

The sample, dried by the traditional convective method at a temperature of 55°C (Fig. 6a), has a rough surface with longitudinal cracks up to 1 mm long over the entire surface area, characteristic of this drying method. The roughness of the sample surface is created by the cell membranes deformed as a result of dehydration.

As a result of sonication before drying (Fig. 6b-Fig. 6d), the surface of convection-dried samples becomes rougher. This is due to the rupture and detachment of cell membranes (in the form of flakes in the photo) of the upper layers of the sample under the action of ultrasonic cavitation. With the increase of the ultrasonic treatment time from 5 (Fig. 6b) to 10 min (Fig. 6c), the surface roughness of the sample increases. However, the surface of the sample treated for 20 min (Fig. 6d) looks less rough compared to the one treated for 10 min. This is due to the significant destruction of the sample by ultrasonic cavitation, which leads to the removal of the top layer of destroyed cells from the surface. Consequently, the use of ultrasonic processing for more than 10 min can negatively affect the final weight of the finished product, resulting in significant losses of useful dry matter.

In addition to the change in surface roughness, the appearance of pores in the material is observed, which confirms the results obtained by M. Nowacka *et al.* (2022). The authors note that ultrasound has a significant effect on the structure of the dried raw material. As a result of ultrasonic vibrations, the shrinkage of the material during the drying process increased from 9 to 11%, the density of the product decreased by 6-20% and the porosity increased by 9-14% compared to untreated samples.

The use of direct electric heating during the convective drying process leads to an increase in the porosity of the sample (Fig. 6d). From the images obtained, it is possible to see the presence of micropores of a certain size throughout the surface. The surface roughness of the samples dried using direct electric heating does not visually differ from that of the conventionally dried sample.

The analysis of the surface structure of the samples shows that changes in apple raw materials caused by ultrasound differ from those caused by the use of direct electric heating in the process of combined drying. When apples are processed in an ultrasonic bath, almost no ruptures of tissue cell membranes are observed, or the damage is small and local. At the same time, the use of direct electric heating in the dehydration process has a more significant impact on the structure of the raw material. This is due to the destruction of the cell membranes of the samples as a result of electroplasmolysis.

The simultaneous use of ultrasonic treatment for 5 min and direct electric heating in the process of convective drying leads to both an increase in the porosity of the sample and an increase in the roughness of its surface (Fig. 6e). However, the structure of the samples during combined drying treated with ultrasound for 20 min (Fig. 6e) has a slightly lower roughness and porosity, which confirms the hypothesis of the possible closure of pores in the material under prolonged exposure to ultrasonic vibrations, as outlined in A.R. Jambrak *et al.* (2018). The increase in the roughness and porosity of the samples explains the intensification of the rate of moisture removal from the material. As the roughness of the samples increases, the useful area of their blowing increases, and as a result of the increase in the porosity of the material, additional channels for moisture removal appear, which facilitates its movement from the inner layers to the surface (Wiktor *et al.*, 2016; Fijalkowska *et al.*, 2017).

The decrease in the porosity of fruit raw materials as a result of prolonged sonication explains the decrease in the rate of moisture removal and the increase in the drying time during combined heating using direct electric heating and confirms the results of the study by O. Savoiskyi *et al.* (2023). Studies have shown that when samples are treated in an ultrasonic bath for 10 min, the time to reach the final moisture content increases by 17.2%, and when the treatment duration is increased to 20 min, it increases by 23.4% compared to control samples.

One of the simplest methods to intensify the dehydration process and reduce energy consumption is to pretreat the raw material immediately before drying. Pretreatment can be carried out by chemical and physical methods. All physical pretreatment methods can be divided into two types: thermal and non-thermal.

X. Cheng *et al*. (2015) found that in the food industry, ultrasonic waves of the low frequency of 20-100 kHz are commonly used, as the effect of ultrasonic cavitation in this wave range is the most optimal.

The studies conducted by O. Savoiskyi & V. Sirenko (2023) show that the use of pretreatment in an ultrasonic bath for 10 min at a frequency of 44 kHz can reduce the duration of convective dehydration by 27.8%. The obtained results are in line with the data reported by S. Tüfekçi & S.G. Özkal (2020), who found that sonication reduces the duration of dehydration by 25-40% and reduces energy consumption by 35-70%.

The use of ultrasonic treatment in combined drying with direct electric heating is ambiguous. Processing of raw materials in an ultrasonic bath before drying with a combined heating method for 5 min practically does not intensify the dehydration process, and for 10 and 20 min, on the contrary, reduces the efficiency of moisture removal, as established in the work of O. Savoiskyi & V. Sirenko (2023). This is caused by changes in the electrophysical parameters and structure of the raw material during sonication.

It should also be noted that as a result of the use of ultrasonic treatment and direct electric heating in the drying process, there is no cracking of the material, which is typical for convective heating. Thus, experimental studies confirm that the use of preliminary sonication of raw

materials in the combined drying process with direct electric heating reduces the current strength of electric heating, which can avoid overheating of raw materials, improve the quality of finished products and contribute to an increase in biomethane yield.

CONCLUSIONS

Experimental studies show the feasibility of using preliminary ultrasonic treatment of raw materials in the technological process of combined drying using direct electric heating.

An increase in the duration of the pretreatment reduces the maximum values of the direct electric heating current in the process of convective drying. Processing of apple raw materials for 20 min reduced the peak current values by 27% compared to untreated samples. Reducing the current intensity during the drying process will exclude possible overheating of apple raw materials during dehydration, which can positively affect the quality of finished products.

It has been determined that the longer the duration of sonication, the lower the value of the initial resistivity of the raw material. After sonication in an ultrasonic bath for 5 min, the initial resistivity values decreased by 7.8%, and further increasing the duration of sonication to 10 and 20 min reduced the initial resistivity values by 9.4 and 13.4% compared to the control samples. The duration of pretreatment does not affect the time of electro-plasmolysis of raw materials, and the destruction of the shells occurs at slightly higher values of resistivity.

The analysis of the obtained images of the sample surface structure shows that the ultrasonic treatment for 5 and 10 min during convective drying increases the roughness of the dried samples and increasing the treatment to 20 min can lead to the destruction of the sample surface and the loss of useful dry residue in the finished product. The simultaneous use of ultrasonic processing and direct electric heating in the process of convective drying significantly increases the roughness and porosity of apple raw materials, which can lead to easier release of moisture from the inner layers and intensification of the dehydration process.

Further research should focus on the development of technical means and methods for drying fruit and vegetable raw materials using efficient methods of heat supply and pretreatment, which will simultaneously reduce the energy intensity of the dehydration process and improve the quality of finished products.

ACKNOWLEDGEMENTS

None.

CONFLICT OF INTEREST

The authors declare no conflict of interest.

REFERENCES

[1] Bhatta, S., Janezic, T.S., & Ratti, C. (2020). Freeze-drying of plant-based foods. *Foods*, 9(1), article number 87. doi: 10.3390/foods9010087.

[2] Carmeliet, J., & Verboven, P. (2017). Convective drying of fruit: Role and impact of moisture transport properties in modelling. *Journal of Food Engineering*, 193, 95-107. doi: 10.1016/j.jfoodeng.2016.08.013.

[3] Chandramohan, V. (2020). Convective drying of food materials: An overview with fundamental aspect, recent developments, and summary. *Heat Transfer*, 49(3), 1281-1313. doi: doi: 10.1002/htj.21662.

[4] Cheng, X., Zhang, M., Xu, B., Adhikari, B., & Sun, J. (2015). The principles of ultrasound and its application in freezing related processes of food materials: A review. *Ultrasonics Sonochemistry*, 27, 576-585. doi: 10.1016/j.ultsonch.2015.04.015.

[5] Doymaz, İ., Demir, H., & Yildirim, A.D. (2015). Drying of quince slices: Effect of pretreatments on drying and rehydration characteristics. *Chemical Engineering Communications*, 202(10), 1271-1279. doi: 10.1080/00986445.2014.921619.

[6] Fan, K., Zhang, M., & Mujumdar, A.S. (2017). Application of airborne ultrasound in the convective drying of fruits and vegetables: A review. *Ultrasonics Sonochemistry*, 39, 47-57. doi: 10.1016/j.ultsonch.2017.04.001.

[7] Fijalkowska, A., Nowacka, M., & Witrowa-Rajchert, D. (2017). The physical, optical and reconstitution properties of apples subjected to ultrasound before drying. *Italian Journal of Food Science*, 29(2), 343-356. doi: 10.14674/1120-1770/ijfs.v642.

[8] Garcia-Noguera, J., Oliveira, F.D.C., Weller, C.L., & Rodrigues, S. (2012). Effect of ultrasonic and osmotic dehydration pre-treatments on the colour of freeze dried strawberries. *Journal of Food Science and Technology*, 51(9), 2222-2227. doi: 10.1007/s13197-012-0724-x.

[9] Groza, A., & Siddelev, N. (2022). Nonlinear surface polaritons near the interface between a magneto-optical substance and a nonlinear metamaterial with a permittivity close to zero. *Scientific Herald of Uzhhorod University. Series "Physics"*, 51, 24-29.

[10] Guida, V., Ferrari, G., Pataro, G., Chambery, A., Di Maro, A., & Parente, A. (2013). The effects of ohmic and conventional blanching on the nutritional, bioactive compounds and quality parameters of artichoke heads. *LWT – Food Science and Technology*, 53(2), 569-579. doi: 10.1016/j.lwt.2013.04.006.

[11] Huang, D., Yang, P., Tang, X., Luo, L., & Sundén, B. (2021). Application of infrared radiation in the drying of food products. *Trends in Food Science and Technology*, 110, 765-777. doi: 10.1016/j.tifs.2021.02.039.

[12] Isci, A., Kutlu, N., Yilmaz, M.S., Arslan, H., & Sakiyan, O. (2018). The effect of ohmic heating pretreatment on drying of apple. In *Proceedings of 21th International Drying Symposium* (pp. 1487-1494). Valencia: Polytechnic University of Valencia. doi: doi: 10.4995/ids2018.2018.7375.

[13] Jambrak, A.R., Mason, T.J., Paniwnyk, L., & Lelas, V. (2018). Ultrasonic effect on pH, electric conductivity, and tissue surface of button mushrooms, Brussels sprouts and cauliflower. *Czech Journal of Food Sciences*, 25(2), 90-99. doi: 10.17221/757-cjfs.

[14] Moreno, J., Simpson, R., Pizarro, N., Pavez, C., Dorvil, F., Petzold, G., & Bugueño, G. (2013). Influence of ohmic heating/osmotic dehydration treatments on polyphenoloxidase inactivation, physical properties and microbial stability of apples (cv. Granny Smith). *Innovative Food Science & Emerging Technologies*, 20, 198-207. doi: 10.1016/j.ifset.2013.06.006.

[15] Nowacka, M., Wiktor, A., Śledź, M., Jurek, N., & Witrowa-Rajchert, D. (2012). Drying of ultrasound pretreated apple and its selected physical properties. *Journal of Food Engineering*, 113(3), 427-433. doi: 10.1016/j.jfoodeng.2012.06.013.

[16] Ren, Z., & Bai, Y. (2018). Ultrasound pretreatment of apple slice prior to vacuum freeze drying. *Advances in Engineering Research*, 169, 112-117. doi: 10.2991/mseee-18.2018.20.

[17] Savoiskyi, O., & Sirenko, V. (2023). Revealing the influence of ultrasonic processing on the kinetic parameters of convective and combined drying of raw apple materials. *Eastern-European Journal of Enterprise Technologies*, 2(11(122)), 91-98. doi: 10.15587/1729-4061.2023.276748.

[18] Savoiskyi, O., Yakovliev, V., & Sirenko, V. (2021). Determining the kinetic and energy parameters for a combined technique of drying apple raw materials using direct electric heating. *Eastern-European Journal of Enterprise Technologies*, 1(11(109)), 33-41. doi: 10.15587/1729-4061.2021.224993.

[19] Tüfekçi, S., & Özkal, S.G. (2020). Investigation of effect of ultrasound pretreatment on drying and rehydration characteristics and microstructure of apple slices. *Yuzuncu Yıl University Journal of Agricultural Sciences*, 30, 950-962 . doi: 10.29133/yyutbd.698826.

[20] Wiktor, A., Sledz, M., Nowacka, M., Rybak, K., & Witrowa-Rajchert, D. (2016). The influence of immersion and contact ultrasound treatment on selected properties of the apple tissue. *Applied Acoustics*, 103, 136-142. doi: 10.1016/j.apacoust.2015.05.001.

[21] Xiao, H., Pan, Z., Deng, L., El-Mashad, H.M., Yang, X., Mujumdar, A.S., Gao, Z., & Zhang, Q. (2017). Recent developments and trends in thermal blanching – A comprehensive review. *Information Processing in Agriculture*, 4(2), 101-127. doi: 10.1016/j.inpa.2017.02.001.

[22] Zhou, X., & Wang, S. (2019). Recent developments in radio frequency drying of food and agricultural products: A review. *Drying Technology*, 37(3), 271-286. doi: 10.1080/07373937.2018.1452255.

[23] Zubernik, J., Dadan, M., Cichowska, J., & Witrowa-Rajchert, D. (2019). The impact of the pre-treatment in ethanol solution on the drying kinetics and selected properties of convective dried apples. *International Journal of Food Engineering*, 16(1-2), article number 20180338. doi: 10.1515/ijfe-2018-0338.

Леонід Степанович Червінський
Доктор технічних наук, професор
Національний університет біоресурсів і природокористування України
03041, вул. Героїв Оборони, 15, м. Київ, Україна
https://orcid.org/0000-0001-7215-2474
Олександр Юрійович Савойський
Старший викладач
Сумський національний аграрний університет
40021, вул Герасима Кондратьєва, 160, м. Суми, Україна
https://orcid.org/0000-0002-6459-4931
Віктор Федорович Сіренко
Кандидат технічних наук, доцент
Сумський національний аграрний університет
40021, вул Герасима Кондратьєва, 160, м. Суми, Україна
https://orcid.org/0000-0003-0831-6563

Аналіз впливу ультразвукової обробки на структуру та електрофізичні властивості фруктів при комбінованому сушінні

Анотація. Використання ультразвукових коливань для інтенсифікації технологічних процесів переробки сільськогосподарської продукції набуває актуальності в харчовій промисловості, оскільки може призвести до зниження енерговитрат на здійснення процесу зневоднення сировини. Метою роботи було дослідження впливу ультразвукової обробки на зміну електрофізичних параметрів та структуру яблучної сировини в процесі комбінованого сушіння з використанням прямого електричного нагріву. Ультразвукову обробку яблук перед сушінням проводили в ультразвуковій ванні, заповненій водою, протягом 5, 10 та 20 хв. За допомогою методів растрової електронної мікроскопії отримано знімки структури поверхонь висушених зразків яблук при різних комбінаціях тривалості обробки ультразвуком та способів підводу тепла до сировини в процесі сушіння. На основі проведених експериментальних досліджень отримано залежності величини сили струму, що перетікає через зразок в процесі комбінованого сушіння з використанням прямого електронагріву від тривалості обробки сировини в ультразвуковій ванні. Встановлено вплив попередньої ультразвукової обробки на максимальні значення сили струму при прямому електронагріві. Досліджено залежності зміни питомого електричного опору зразків яблук в процесі зневоднення при різній тривалості попередньої обробки. Визначено вплив ультразвуку на початковий питомий електричний опір яблук, тривалість електроплазмолізу та значення питомого електричного опору, при яких спостерігаються максимальні значення струму прямого електронагріву. Результати проведених експериментів показують, що попередня обробка сировини в ультразвуковій ванні дозволяє зменшити пікові значення струму до 27 %. Початкові значення питомого електричного опору сировини після обробки ультразвуком зменшуються на 7,8–13,8 % в порівнянні з контрольними зразками. Отримані знімки поверхонь висушених фруктів показали збільшення пористості та шорсткості зразків. Отримані результати експериментальних досліджень можуть стати передумовою для розробки енергоефективного технічного засобу ультразвукової обробки плодоовочевої сировини перед сушінням та вибору оптимальних режимів роботи

Ключові слова: яблучна сировина; конвективне зневоднення; прямий електронагрів; питомий електричний опір; растрова електронна мікроскопія; шорсткість

Machinery & Energetics
Vol. 14, No. 2. 2023

Journal homepage:
https://technicalscience.com.ua/en

UDC 535.372, 628.9.037
DOI: 10.31548/machinery/2.2023.80

Volodymyr Boyko
PhD in Physical and Mathematical Sciences, Associate Professor
National University of Life and Environmental Sciences of Ukraine
03041, Heroiv Oborony st., 15, Kyiv, Ukraine
https://orcid.org/0000-0003-2926-2752

Vitalii Chornii*
PhD in Physical and Mathematical Sciences
National University of Life and Environmental Sciences of Ukraine
03041, Heroiv Oborony st., 15, Kyiv, Ukraine
https://orcid.org/0000-0003-3727-5617

Serhii Nedilko
Doctor of Physical and Mathematical Sciences, Senior Researcher
Taras Shevchenko National University of Kyiv
01601, Volodymyrska st., 64/13, Kyiv, Ukraine
https://orcid.org/0000-0001-5196-6807

Kateryna Terebilenko
Doctor of Chemistry, Associate Professor
Taras Shevchenko National University of Kyiv
01601, 64/13 Volodymyrska Str., Kyiv, Ukraine
https://orcid.org/0000-0003-2403-4347

Luminescent converters based on "nanocellulose + $K_3Tb(PO_4)_2$:Eu" composite films

Abstract. The advantages of cellulose and its derivatives as the latest materials for devices that generate, store, and convert electricity are their low cost, environmental friendliness, ease of recycling and the ability to be manufactured in various ways and from various raw materials, including agricultural waste. This predetermines the relevance of their study as materials for modern technology and electronics. The research aims to determine the luminescent characteristics of composite films made based on nanocellulose and polycrystalline oxide $K_3Tb_{0.9}Eu_{0.1}(PO_4)_2$. Optical microscopy and the spectral-luminescence method were used to characterise the films and their initial components. It was found that crystallites with an average size of about 50 μm are distributed quite evenly in the film "nanocellulose +$K_3Tb_{0.9}Eu_{0.1}(PO_4)_2$". A Raman scattering band with a maximum of 564 nm under laser excitation at 473 nm was observed for the investigated samples in the form of suspensions. The intensity of photoluminescence of nanocellulose in suspension and films is low compared to the luminescence of oxide as a filler. The luminescence of Eu^{3+} ions is intense in the red region of the spectrum. The calculated values of the degree of asymmetry indicate low symmetry of the positions occupied by europium ions in the oxide and the contribution of Tb^{3+} ion emission to the overall spectrum of the composite film. The study results show that the luminescence of Eu^{3+} ions is sensitised by Tb^{3+} ions, which absorb the excitation light and then transfer energy to europium ions. The position of the absorption bands of Eu^{3+} and Tb^{3+} ions in the ultraviolet region of the spectrum and

Article's History: Received: 13/01/2023; Revised: 07/04/2023; Accepted: 26/04/2023.

Suggested Citation:
Boyko, V., Chornii V., Nedilko, S., & Terebilenko, K. (2023). Luminescent converters based on "nanocellulose + $K_3Tb(PO_4)_2$:Eu" composite films. *Machinery & Energetics,* 14(2), 80-89. doi: 10.31548/machinery/1.2023.80.

*Corresponding author

the intense emission of Eu^{3+} in the red region indicates the prospects of using nanocellulose + $K_3Tb_{0.9}Eu_{0.1}(PO_4)_2$ films to improve the efficiency of solar panels. Testing of the films under the excitation of luminescence by ultraviolet radiation of an LED (λ_{ex} = 375 nm) showed the possibility of developing white LEDs on their basis. In particular, the chromaticity coordinates of the uncoated LED were (x = 0.214; y = 0.079), and the use of a film composite as a coating causes a shift in the coordinates to the red region: x = 0.304, y = 0.196. The obtained results on the morphology and luminescent properties can be used to optimise the composition and manufacturing conditions of composite films of the following types "nanocellulose +$K_3Tb_{0.9}Eu_{0.1}(PO_4)_2$" for use as fluorescent converters in LEDs or solar panels

Keywords: ion; sensitisation; LED; solar panel; photoluminescence; coating

INTRODUCTION

At the current stage of equipment and technology development, in particular, those related to the production, storage and conversion of electricity, a significant need for low-cost materials exists. One of the challenges is also the significant increase in waste associated with electronic devices. According to analysts V. Forti *et al*. (2020), the rate of electronics waste generation will be around 74.7 million tonnes per year by 2030. Only a small part of this waste is recycled, and the rest pollutes the environment (Ahirwar & Tripathi, 2021). Thus, the latest materials need to be cheap and easy to dispose of. There is a growing focus on cellulose as a material for modern technologies (Fang *et al.*, 2021; Zhao *et al.*, 2021). Cellulose is a fairly cheap natural polymer due to the abundance of its sources (from wood raw materials to agricultural waste) and well-developed manufacturing technologies. Nanocellulose (NC) is also being actively researched, in particular, the kind that is produced by an environmentally friendly bacterial method with minimal use of chemicals (Urbina *et al.*, 2021; Choi *et al.*, 2022). In addition to being cheap, cellulose and its derivatives are environmentally friendly, biocompatible, and naturally biodegradable. N.C. Raut & K. Al-Shamery (2018) and P. Wang *et al.* (2018) found that 3D printing technology has given an additional impetus to the development of cellulose-based materials for technology and the creation of a whole area of "paper" electronics. The study by D. Choe *et al.* (2018) and I. Indriyati *et al.* (2019) have shown that the physical and chemical properties of cellulose significantly depend on the method of manufacture and further processing. Therefore, to improve the properties of this natural polymer, impurities of a certain nature are added to it, depending on the intended use. For example, the addition of zinc, nickel, and carbon oxide nanoparticles to cellulose is proposed as a way to obtain a lightweight, flexible, and low-cost material for solar panels, as reported by G.F. Gemeda *et al.* (2022) and X. Liu *et al.* (2020). Composites based on cellulose and inorganic polymers or carbon nanostructures have been investigated as promising materials for dielectric capacitors and supercapacitors (Pal *et al.*, 2022; Wang *et al.*, 2023; Zhu *et al.*, 2023). M. Nedielko *et al.* (2018) and J. Gan *et al.* (2022) noted that microcrystalline cellulose incorporated with luminescent particles is a promising material for luminescent light converters and LEDs. For such systems, the interaction between the elements of the cellulose matrix and the filler is important. It is the presence of such interaction between the components that allows us to assert the presence of a composite material whose properties are not the "sum" of the properties of its components. Despite a significant number of scientific studies of cellulose-based composites, there is almost no understanding of the processes and ways of this interaction due to the overall complexity of the material structure, which makes this study relevant.

The research aimed to fabricate and determine the luminescent characteristics of composite films based on NC and $K_3Tb_{0.9}Eu_{0.1}(PO_4)_2$ oxide, which have prospects for use as luminescent coatings for LEDs or solar cell components. The morphology and optical properties of films of this composition have not been studied before. The optical properties of composites with luminescent oxides have been the subject of a rather limited number of scientific papers. The main research objectives were to fabricate the films, measure the photoluminescence (PL) and PL excitation spectra, and analyse the spectral characteristics from the perspective of the practical application of these luminescent materials.

MATERIALS AND METHODS

The production of the films (NC and "NC+ $K_3Tb_{0.9}Eu_{0.1}(PO_4)_2$") and the study of their morphology using optical microscopy were carried out at the Department of Physics of the National University of Life and Environmental Sciences of Ukraine in February 2023. The study of the spectral and luminescent properties of the films was carried out at the Faculty of Physics of Taras Shevchenko National University of Kyiv in March and April 2023. The choice of the composite film components was based on the following considerations: it is known that pure cellulose exhibits visible photoluminescence, the characteristics of which depend on the excitation wavelength (Nedielko *et al.*, 2017; Zou *et al.*, 2019). Thus, such a polymer matrix should play an active role in the processes of light absorption and emission in the composite. The NC consists of nanoscale structures (crystals, whiskers, fibrils) that can be easily arranged near the surface of the filler particle. In this case, the effective contact area between the oxide and the cellulose should be larger than in the case of composites based on microcrystalline cellulose, in which the filler occupies only a part of the space between the fibres. As for the choice of the oxide filler, $K_3Tb(PO_4)_2$:Eu, this material

is characterised by intense photoluminescence in the red spectral region when excited by ultraviolet (UV) radiation (Mikhailik *et al.*, 2009). Accordingly, it was expected that the manufactured nanocomposites would be capable of converting UV radiation into visible light.

Production of nanocellulose films and composites samples "NC+$K_3Tb_{0,9}Eu_{0,1}(PO_4)_2$" was carried out using a nanocellulose suspension in water (dry matter content: 0.6 wt%). The conditions for obtaining this suspension and its characteristics have been described in detail previously (Barbash *et al.*, 2019). Synthesis of oxide $K_3Tb_{0,9}Eu_{0,1}(PO_4)_2$ was made from fluoride melts using a method similar to that described in the study (Terebilenko *et al.*, 2017). The procedure for making the films was as follows: thoroughly ground oxide powder $K_3Tb_{0,9}Eu_{0,1}(PO_4)_2$ in the amount of 30 mg was mixed with 2 ml of distilled water and sonicated (f = 4.2 kHz) for 10 min. To the resulting mixture was added 3 ml of nanocellulose suspension. The resulting liquid, after "NC+$K_3Tb_{0,9}Eu_{0,1}(PO_4)_2$" ultrasound treatment for 1 hour, evaporated at 56°C for 4 hours, and then at room temperature in an open space for 2 days. The resulting gel was poured onto a glass substrate, where it was kept for another day until it dried completely to form a film. An identical procedure (except for the addition of oxide) was used to obtain a film of "pure" (without oxide) NC as a comparison sample. The film of "pure" NC was transparent, while the film with oxide was less transparent and matte.

The film samples were examined using an optical microscope and a spectral-luminescence complex consisting of a DFS-12 spectrometer (USSR) with an FEU-100 photomultiplier (USSR), a DMR-4 prism monochromator (USSR), a powerful xenon lamp DKsEL-1000 (USSR), and diode-pumped lasers (λ_{rad} = 405 and 473 nm).

RESULTS AND DISCUSSION

Figure 1 shows micrographs of samples of NC suspension, powder $K_3Tb_{0,9}Eu_{0,1}(PO_4)_2$, NC film and "NC+$K_3Tb_{0,9}Eu_{0,1}(PO_4)_2$" film obtained using an optical microscope in the light transmitted through the sample. For the initial NC suspension, a certain number of thin, long microstructures are observed, which are cellulose microfibrils (Fig. 1a). Rectangular formations, such as cellulose microcrystals, can also be seen. Figure 1b shows the area with the largest $K_3Tb_{0,9}Eu_{0,1}(PO_4)_2$ particles with a size of ~300 μm. However, the vast majority of oxide powder particles are several μm and even smaller. These small particles form small dark-coloured agglomerates, which are destroyed by ultrasound. For the thin NC film (Fig. 1c), a significant number of microcrystals is observed. In contrast to the case of the nanocellulose suspension, no microfibrils are observed here, which may be due to the destruction of the latter under the action of ultrasound. In the case of the film "NC+$K_3Tb_{0,9}Eu_{0,1}(PO_4)_2$" A fairly uniform distribution of oxide crystals without significant particle agglomerates can be observed (Fig. 1d).

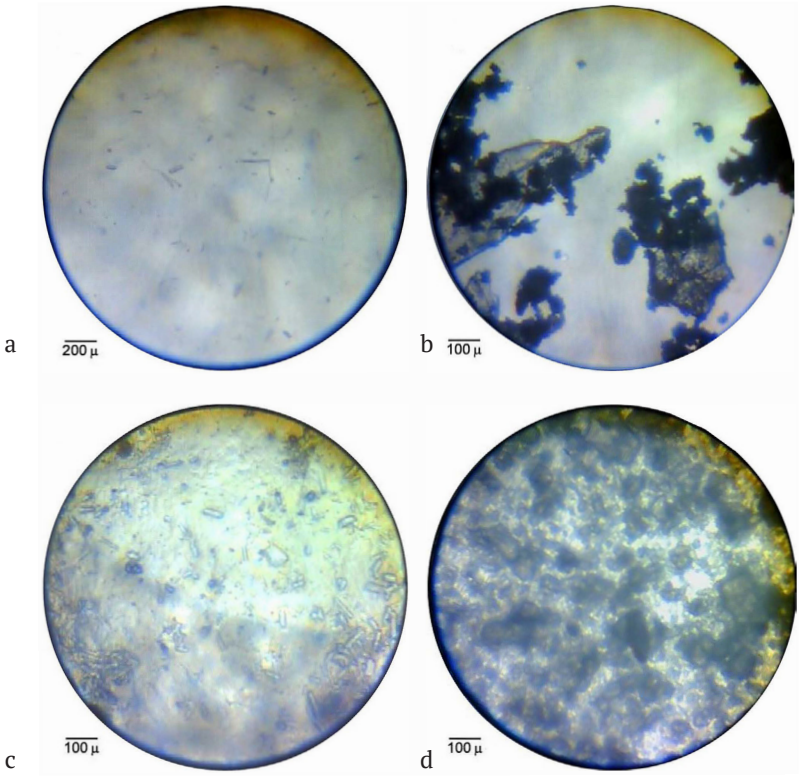

Figure 1. Microphotos
Note: a) NC suspension drop, b) powder $K_3Tb_{0.9}Eu_{0.1}(PO_4)_2$, c) NC film, d) film "NC+$K_3Tb_{0.9}Eu_{0.1}(PO_4)_2$"
Source: compiled by the authors

Figure 2 shows the photoluminescence spectra of the powder $K_3Tb_{0.9}Eu_{0.1}(PO_4)_2$, NC and "NC+$K_3Tb_{0.9}Eu_{0.1}(PO_4)_2$" suspensions. In the PL spectrum of oxide under laser excitation, (473 nm), rather narrow bands associated with the emission of Tb^{3+} (electronic transition $^5D_4 \rightarrow {}^7F_6$, λ_{max} = 543 nm) and Eu^{3+} ions (transition $^5D_0 \rightarrow {}^7F_{0\text{-}4}$: remaining lines on spectrum 1, Fig. 2) are observed. The peculiarity of the Tb^{3+} and Eu^{3+} ions is their $4f^N$ shielded electron shells, within which the above electronic transitions occur (Dorenbos, 2000). As a result of the shielding, the position of the maxima of the corresponding bands weakly depends on the immediate environment of the ions and the PL excitation conditions. Therefore, the data obtained in the present study on the luminescent properties of $K_3Tb_{0.9}Eu_{0.1}(PO_4)_2$ are consistent with the results of V.B. Mikhailik *et al*. (2009), despite the different PL excitation conditions.

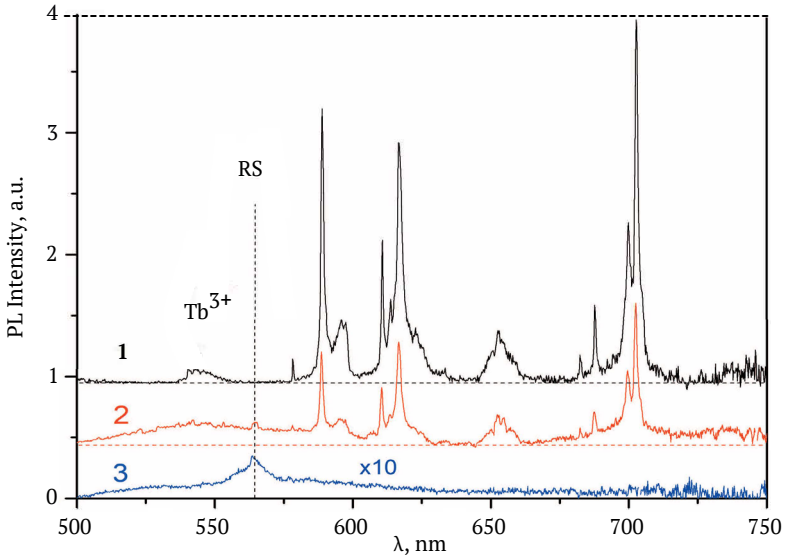

Figure 2. Photoluminescence spectra

Note: 1) powder $K_3Tb_{0.9}Eu_{0.1}(PO_4)_2$, 2) suspension "NC+ $K_3Tb_{0.9}Eu_{0.1}(PO_4)_2$", 3) initial NC suspension, λ_{enr}=473 nm, T=295 K. The zero-signal level for spectra 1 and 2 is shown by horizontal dashed lines

Source: compiled by the authors

The initial nanocellulose suspension at 473 nm excitation is characterised by a low-intensity PL (spectrum 3 in Fig. 2), which is due to the low polymer content (0.6 wt%) and the PL attenuation by water molecules. The band of this PL is very broad, and complex, and extends from 500 to 730 nm. It is quite similar to the PL of microcrystalline cellulose (Nedielko *et al.*, 2017) and is associated with a set of PL centres arising from carbonyl, carboxyl, and methyl molecular groups. Against the background of the PL band of nanocellulose, a rather narrow band with a maximum of 564 nm is observed (the position is shown by a vertical dashed line and denoted RS). This band is a manifestation of Raman scattering of laser radiation on water molecules. Indeed, taking the difference in the frequency of the band maximum position (ν≈17730 cm^{-1}) and the laser frequency (ν≈21140 cm^{-1}), a frequency of Δν≈3410 cm^{-1}, which corresponds to the stretching/compressing vibrations of OH groups in water, was obtained (Beran *et al.*, 2001).

The photoluminescence spectrum of the suspension "NC+$K_3Tb_{0.9}Eu_{0.1}(PO_4)_2$" contains both bands associated with the NCs and those related to the luminescence centres in the oxide. It is worth noting that in this experiment, a suspension was used from which 4 ml of water was evaporated. This results in a significant weakening of the Raman scattering band in the spectrum 2 Figure 2, as well as a certain increase in the intensity of the PL band of nanocellulose. Such a suspension can be used as the basis for luminescent inks for 3D printing of paper electronics elements (Zhuravlov *et al.*, 2021).

The presence of a narrow weak PL band with a maximum at 579 nm, which is associated with the transition $^5D_0 \rightarrow {}^7F_0$ in the ion of Eu^{3+}, for oxide powder $K_3Tb_{0.9}Eu_{0.1}(PO_4)_2$ and suspension "NC+$K_3Tb_{0.9}Eu_{0.1}(PO_4)_2$" (spectra 1 and 2, Fig. 2) indicates a rather low symmetry of the surroundings of this ion both in the original oxide and in the case when the oxide particles are in the NC suspension. This result is consistent with the crystallographic data (Farmer *et al.*, 2016), according to which the trivalent cation in $M_3RE(PO_4)_2$ systems, where M is an alkali metal and RE is a rare earth ion, occupies a position with the symmetry of the surroundings – C_{2v}. In the 585-600 nm region, bands of $^5D_0 \rightarrow {}^7F_1$ magneto-dipole transitions in Eu^{3+} ions are observed. A detailed examination of spectra 1 and 2 (Fig. 2) reveals 3 components in this region, which, according to K. Binnemans (2009), is evidence of low symmetry of the Eu^{3+} ion environment or the presence of two different types of emission centres.

R. Reisfeld *et al.* (2004) demonstrated that the ratio of the integrated PL intensities for the transitions $^5D_0 \rightarrow {}^7F_2$

(600-635 nm) and $^5D_0 \rightarrow {}^7F_1$ (580-600 nm) calculated by formula (1), depends on the symmetry of the Eu^{3+} environment. This value is called the degree of asymmetry of the Eu^{3+} ion environment. It is known that the higher the value of *R*, the more attractive the material is as a red phosphor:

$$R = \frac{I(^5D_0 \rightarrow {}^7F_2)}{I(^5D_0 \rightarrow {}^7F_1)}. \quad (1)$$

The *R* values calculated from spectra 1 and 2 in Figure 2 are 1.63 and 1.77, respectively. They are significantly lower than the value of $R \approx 2.7$ for Eu^{3+} ions at the C_{2v} symmetry position (Bettinelli *et al.*, 1996). This difference between the data obtained can be explained by the presence of emission bands of Tb^{3+} ions ($^5D_4 \rightarrow {}^7F_4$ transitions) in the 580-600 nm region, which increases the value of the denominator in formula (1).

The photoluminescence intensity of the suspensions under xenon lamp excitation was insufficient to record the PL excitation spectra. Therefore, the excitation spectra were recorded only for the powder $K_3Tb_{0.9}Eu_{0.1}(PO_4)_2$ and NC films and composites "NC+$K_3Tb_{0.9}Eu_{0.1}(PO_4)_2$" (Fig. 3).

The red photoluminescence of the oxide, which is associated with the emission of Eu^{3+} ions, is effectively excited in the UV region of the spectrum (spectrum 1 in Fig. 3). Spectrum 2 excitation of the green PL of the powder $K_3Tb_{0.9}Eu_{0.1}(PO_4)_2$, associated with the emission of ions Tb^{3+}, is similar to spectrum 1, except for the band at 395 nm. It can be argued that in this oxide, an effective transfer of excitation energy from terbium to europium is realised, i.e., the sensitisation of the PL of Eu^{3+} ions by Tb^{3+} ions. The excitation energy transfer has been previously observed for other oxide materials containing this pair of ions (Xie *et al.*, 2015; Silveira *et al.*, 2020; Bu *et al.*, 2022). It should be noted that the excitation of red PL through the absorption of light by Tb^{3+} ions is more efficient than the direct excitation through the absorption of Eu^{3+} ions. Excitation of red luminescence of a composite film "NC+$K_3Tb_{0.9}Eu_{0.1}(PO_4)_2$" also occurs in the UV region due to the absorption of terbium and europium ions. The low-intensity luminescence of the nanocellulose film is excited in a multicomponent band lying in the spectral range of $\lambda < 480$ nm (spectrum 4 in Fig. 3).

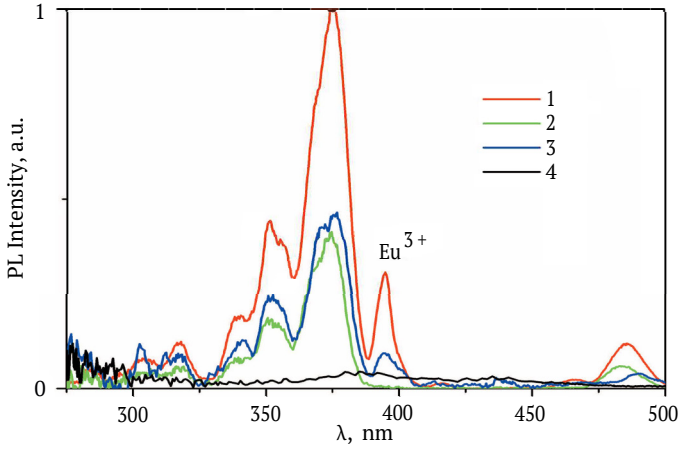

Figure 3. Photoluminescence excitation spectra
Note: powder $K_3Tb_{0.9}Eu_{0.1}(PO_4)_2$ (1, 2), film "NC+$K_3Tb_{0.9}Eu_{0.1}(PO_4)_2$" (3), NC film (4); registration at λ_{em}=618 (1, 3), 543 (2) and 570 nm (4), T=295 K
Source: compiled by the authors

Comparing the excitation spectra of the red PL (λ_{em}=618 nm) with the data obtained in the study by S. Kim *et al.* (2019) on the solar spectrum on the Earth's surface and the spectral efficiency of modern solar panels of various types, it is worth noting the following: at wavelengths shorter than 450 nm, silicon solar panels demonstrate less than 50% of their maximum efficiency, and at $\lambda < 380$ nm – less than 10%. At the same time, on the Earth's surface, the spectrum of solar radiation has a maximum in the 500 nm region but extends down to 300 nm. Accordingly, the shortwave part of solar radiation is used extremely inefficiently in the operation of solar panels. At the same time, such panels demonstrate the highest efficiency when illuminated in the 580-730 nm range, i.e., exactly where Eu^{3+} ions emit. Accordingly, the use of oxide $K_3Tb_{0.9}Eu_{0.1}(PO_4)_2$, in particular as components of a composite film "NC+$K_3Tb_{0.9}Eu_{0.1}(PO_4)_2$" as a fluorescent converter of UV radiation from the 330-400 nm range into red light, can increase the efficiency of solar panels (Bondar *et al.*, 2021).

Films "NC+$K_3Tb_{0,9}Eu_{0,1}(PO_4)_2$" can also be used as a coating to improve the efficiency of electricity-to-light converters – in LEDs. Among the cheapest LEDs are those that emit in the blue and UV spectral ranges. Figure 4 shows the UV spectra of composite films under laser excitation at 405 and 475 nm. The spectra differ both in the number and intensity of narrow europium emission lines and in the characteristics of the wide luminescence band of the cellulose matrix. That is, by changing the excitation wavelength, the colour of the coating can be controlled.

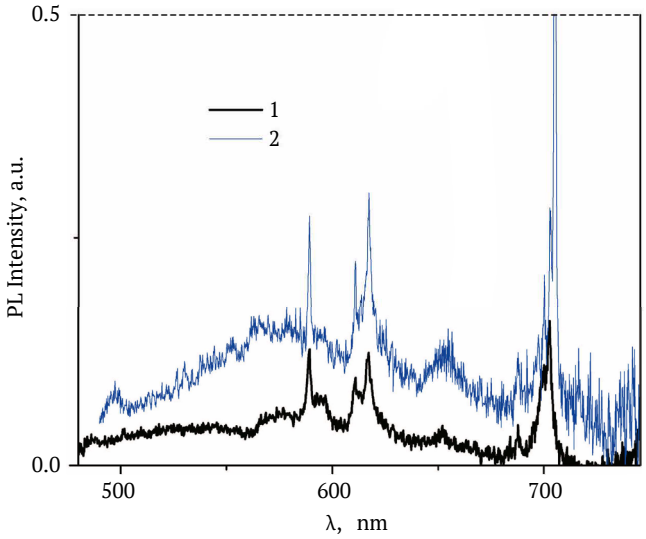

Figure 4. PL spectra of the "NC+$K_3Tb_{0.9}Eu_{0.1}(PO_4)_2$" films
Note: PL excitation at λ_{exc}=405 (1) and 473 nm (2), T=295 K
Source: compiled by the authors

Calculated *R*-values for PL of "NC+$K_3Tb_{0.9}Eu_{0.1}(PO_4)_2$" film under excitation at 405 and 473 nm are 1.95 and 3.25, respectively. A significant increase in *R* can be explained by the fact that the contribution of terbium luminescence in the 580-600 nm region decreases compared to europium luminescence. According to the results of C. Zuo *et al*. (2015), the PL excitation spectra of Tb^{3+} ions in the visible region show that at λ_{ex} = 405 nm these ions do not emit, and at λ_{exc} = 473 nm their low-intensity luminescence is possible. Thus, the results on the PL of the NC+$K_3Tb_{0.9}Eu_{0.1}(PO_4)_2$ films can be explained based on the literature data mentioned in this section on the peculiarities of the crystal structure of $M_3RE(PO_4)_2$ compounds and the luminescence of Eu^{3+} and Tb^{3+} ions in oxides.

To check the efficiency of UV light absorption and its conversion into visible radiation, the visible radiation spectra of an LED with λ_{max} = 375 nm and a test system based on the same LED with a "NC+$K_3Tb_{0.9}Eu_{0.1}(PO_4)_2$" film were recorded. The film was placed directly after the LED. V. Veleschuk *et al.* (2019) found that high-power UV LEDs have parasitic emission in the blue and yellow regions due to electroluminescence. Similar parasitic blue and yellow emission is observed for the used UV LED (spectrum 1 in Fig. 5).

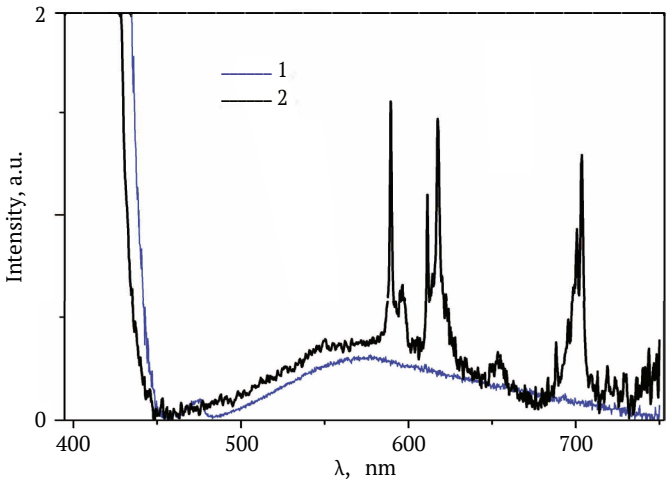

Figure 5. Radiation spectra
Note: 1 – UV LED (λ_{max}=375 nm); 2 – "UV LED + film "NC+$K_3Tb_{0,9}Eu_{0,1}(PO_4)_2$"; T=295 K
Source: compiled by the authors

In the case of the LED + film system, stray radiation is attenuated due to the low transparency of the film. At the same time, narrow emission lines of europium ions are observed. It can also be assumed that the broadband

with a maximum at 580 nm is a superposition of the diode electroluminescence band and the nanocellulose photoluminescence band. Colour coordinates are often used to assess the colour characteristics of radiation. The colour coordinates according to CIE 1931 (Schanda, 2007) for white are (x = 0.333; y = 0.333). The presence of luminescence in the blue and yellow spectral regions of the UV LED leads to colour coordinates corresponding to blue light (x = 0.214; y = 0.079). Adding a film "NC+$K_3Tb_{0.9}Eu_{0.1}(PO_4)_2$" leads to a shift in the coordinates to the red region (x = 0.304; y = 0.196). The coordinate offset on the chromaticity diagram for the CIE 1931 standard is shown in Figure 6.

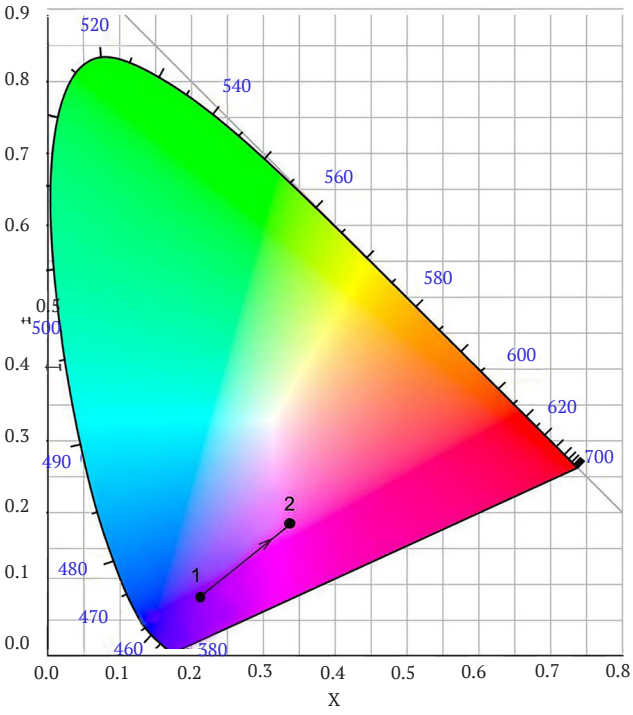

Figure 6. Position of the radiation colour coordinates on the chromaticity diagram

Note: 1 – UV LED (λ_{max}=375 нм); 2 – "UV LED + film "NC+$K_3Tb_{0.9}Eu_{0.1}(PO_4)_2$"; T=295 K

Source: compiled by the authors

Thus, the investigated composite films are promising luminescent LED coatings. The "red" shift of colour coordinates is insufficient, partially due to the small film thickness, which is only 90 ± 10μ m. It can be assumed that an increase in film thickness will lead to enhanced absorption of the blue radiation of the LED and better conversion of the absorbed energy into yellow and red radiation and, accordingly, to improvement of the colour characteristics of the radiation.

CONCLUSIONS

Samples of thin films based on nanocellulose and oxide were prepared by a simple evaporation method from aqueous suspensions. According to the results of optical microscopy, the films contained micro/nanoscale cellulose formations, such as crystals and fibrils. The largest oxide crystals $K_3Tb_{0.9}Eu_{0.1}(PO_4)_2$ had a size of about 300 μm. A fairly uniform distribution of oxide crystals with an average size of about 50 μm was observed in the composite films within the areas of ≈ 0.5 × 0.5 mm². The presence of water molecules, which is manifested in their Raman scattering lines, probably causes the low luminescence intensity of the studied suspensions.

Intense red photoluminescence of the powder $K_3Tb_{0.9}Eu_{0.1}(PO_4)_2$ and thin film "nanocellulose+$K_3Tb_{0.9}Eu_{0.1}(PO_4)_2$", associated with the emission of Eu^{3+} ions, is effectively excited by absorption by terbium ions in the region of 330-400 nm. This is evidence of the efficient transfer of excitation energy from Tb^{3+} ions to Eu^{3+} ions. The presence of red luminescence excitation in the region of 330-400 nm is important from the point of view of developing luminescent converters for solar panels based on the studied films.

Values of the degree of asymmetry calculated from the emission spectra of the powder $K_3Tb_{0.9}Eu_{0.1}(PO_4)_2$, suspensions, and films "nanocellulose+$K_3Tb_{0.9}Eu_{0.1}(PO_4)_2$", is in the range of 1.63-3.25, indicating a low symmetry of the Eu^{3+} ion environment. The significant change in the degree of asymmetry with the excitation wavelength is attributed to the change in the contribution of Tb^{3+} ions to the overall photoluminescence spectrum in the 580-600 nm range.

Films "nanocellulose+$K_3Tb_{0.9}Eu_{0.1}(PO_4)_2$" are capable of absorbing ultraviolet LED radiation and transforming the absorbed energy into yellow and red light. Chromaticity coordinates of the ultraviolet LED with λ_{max}=375 nm equipped with a composite film shift towards the standard for white light.

The investigated materials have the potential to be used as luminescent converters in power generation and conversion devices such as solar panels and LEDs. Further research in this area will be aimed at optimising the concentration of europium ions in the oxide $K_3Tb_{1-x}Eu_x(PO_4)_2$, the ratio between the amount of oxide and nanocellulose, and the film thickness.

ACKNOWLEDGEMENTS

This research was funded by the Ministry of Education and Science of Ukraine. The authors are sincerely grateful to Professor V. A. Barbash (National Technical University of Ukraine "Igor Sikorsky Kyiv Polytechnic Institute") for providing nanocellulose suspensions for the study.

CONFLICT OF INTEREST

None.

REFERENCES

[1] Ahirwar, R., & Tripathi, A.K. (2021). E-waste management: A review of recycling process, environmental and occupational health hazards, and potential solutions. *Environmental Nanotechnology, Monitoring & Management*, 15, article number 100409. doi: 10.1016/j.enmm.2020.100409.

[2] Barbash, V.A., Yashchenko, O.V., & Vasylieva, O.A. (2019). Preparation and properties of nanocellulose from miscanthus x giganteus. *Journal of Nanomaterials*, *2019*, article number 3241968. doi: 10.1155/2019/3241968.
[3] Beran, A., Voll, D., & Schneider, H. (2001). Dehydration and structural development of mullite precursors: An FTIR spectroscopic study. *Journal of the European Ceramic Society*, 21(14), 2479-2485. doi: 10.1016/S0955-2219(01)00265-5.
[4] Bettinelli, M., Speghini, A., Ferrari, M., & Montagna, M. (1996). Spectroscopic investigation of zinc borate glasses doped with trivalent europium ions. *Journal of Non-Crystalline Solids*, 201(3), 211-221. doi: 10.1016/0022-3093(96)00134-2.
[5] Binnemans, K. (2009). Lanthanide-based luminescent hybrid materials. *Chemical Reviews*, 109(9), 4283-4374. doi: 10.1021/cr8003983.
[6] Bondar, I.I., Suran, V.V., Mynya, O.Y., Shuaibov, O.K., Shevera, I.V., & Krasilinets, V.M. (2021). Formation of structured films upon irradiation of an aqueous solution of copper sulphate with high-power laser radiatio. *Scientific Herald of Uzhhorod University. Series "Physics"*, 49, 43-47.
[7] Bu, X., Liu, Y.G., & Chen, J. (2022). Band structure, photoluminescent properties, and energy transfer behavior of a multicolor tunable phosphor $K_3Lu(PO_4)_2$: Tb^{3+},Eu^{3+} for warm white light-emitting diodes. *Journal of Luminescence*, 251, article number 119133. doi: 10.1016/j.jlumin.2022.119133.
[8] Choe, D., Kim, Y.M., Nam, J.E., Nam, K., Shin, C.S., & Roh, Y.H. (2018). Synthesis of high-strength microcrystalline cellulose hydrogel by viscosity adjustment. *Carbohydrate polymers*, 180, 231-237. doi: 10.1016/j.carbpol.2017.10.017.
[9] Choi, S.M., Rao, K.M., Zo, S.M., Shin, E.J., & Han, S.S. (2022). Bacterial cellulose and its applications. *Polymers*, 14(6), article number 1080. doi: 10.3390/polym14061080.
[10] Dorenbos, P. (2000). The $4f^n \leftrightarrow 4f^{n-1}5d$ transitions of the trivalent lanthanides in halogenides and chalcogenides. *Journal of Luminescence*, 91(1-2), 91-106. doi: 10.1016/S0022-2313(00)00197-6.
[11] Fang, Z., Zhang, H., Qiu, S., Kuang, Y., Zhou, J., Lan, Y., Sun, C., Li, G., Gong, S., & Ma, Z. (2021). Versatile wood cellulose for biodegradable electronics. *Advanced Materials Technologies*, 6(2), article number 2000928. doi: 10.1002/admt.202000928.
[12] Farmer, J.M., Boatner, L.A., Chakoumakos, B.C., Rawn, C.J., & Richardson, J. (2016). Structural and crystal chemical properties of alkali rare-earth double phosphates. *Journal of Alloys and Compounds*, 655, 253-265. doi: 10.1016/j.jallcom.2015.09.124.
[13] Forti, V., Baldé, C.P., Kuehr, R., & Bel, G. (2020). The global e-waste monitor 2020. Retrieved from https://ewastemonitor.info/wp-content/uploads/2020/11/GEM_2020_def_july1_low.pdf.
[14] Gan, J., Wu, Y., Yang, F., Zhang, H., Wu, X., Wang, Y., & Xu, R. (2022). Wood-cellulose photoluminescence material based on carbon quantum dot for light conversion. *Carbohydrate Polymers*, 290, article number 119429. doi: 10.1016/j.carbpol.2022.119429.
[15] Gemeda, G.F., Etefa, H.F., Hsieh, C.C., Kebede, M.A., Imae, T., & Yen, Y.W. (2022). Preparation of ZnO/NiO-loaded flexible cellulose nanofiber film electrodes and their application to dye-sensitized solar cells. *Carbohydrate Polymer Technologies and Applications*, 3, article number 100213. doi: 10.1016/j.carpta.2022.100213.
[16] Indriyati, I., Irmawati, Y., & Puspitasari, T. (2019). Comparative study of bacterial cellulose film dried using microwave and air convection heating. *Journal of Engineering and Technological Sciences*, 51(1), 121-132. doi: 10.5614/j.eng.technol.sci.2019.51.1.8.
[17] Kim, S., Jahandar, M., Jeong, J.H., & Lim, D.C. (2019). Recent progress in solar cell technology for low-light indoor applications. *Current Alternative Energy*, 3(1), 3-17. doi: 10.2174/1570180816666190112141857.
[18] Liu, X., Huang, K., Lin, X., Li, H., Tao, T., Wu, Q., Zheng, Q., Huang, L., Ni, Y., Chen, L., Ouyang, X., & Li, J. (2020). Transparent and conductive cellulose film by controllably growing aluminum doped zinc oxide on regenerated cellulose film. *Cellulose*, 27, 4847-4855. doi: 10.1007/s10570-020-03147-0.
[19] Mikhailik, V.B., Kraus, H., & Dorenbos, P. (2009). Efficient VUV sensitization of Eu^{3+} emission by Tb^{3+} in potassium rare-earth double phosphate. *Physica Status Solidi (RRL)–Rapid Research Letters*, 3(1), 13-15. doi: 10.1002/pssr.200802211.
[20] Nedielko, M., Hamamda, S., Alekseev, O., Chornii, V., Dashevskii, M., Lazarenko, M., Kovalov, K., Nedilko, S.G., Tkachov, S., Revo, S., & Scherbatskyi, V. (2017). Mechanical, dielectric, and spectroscopic characteristics of "micro/nanocellulose+ oxide" composites. *Nanoscale Research Letters*, 12(1), article number 98. doi: 10.1186%2Fs11671-017-1862-x.
[21] Nedielko, M., Alekseev, O., Chornii, V., Kovalov, K., Lazarenko, M., Nedilko, S., Scherbatskyi, V., Boyko, V., & Sheludko, V. (2018). Structure and properties of microcrystalline cellulose "Ceramics-Like" composites incorporated with $LaVO_4$:Sm oxide compound. *Acta Physica Polonica A*, 133(4), 838-842. doi: 10.12693/APhysPolA.133.838.
[22] Pal, B., Matsoso, J.B., Parameswaran, A.K., Roy, P.K., Lukas, D., Luxa, J., Marvan, P., Azadmanjiri, J., Hrdlicka, Z., Jose, R., & Sofer, Z. (2022). Flexible, ultralight, and high-energy density electrochemical capacitors using sustainable materials. *Electrochimica Acta*, 415, article number 140239. doi: 10.1016/j.electacta.2022.140239.
[23] Raut, N.C., & Al-Shamery, K. (2018). Inkjet printing metals on flexible materials for plastic and paper electronics. *Journal of Materials Chemistry C*, 6, 1618-1641. doi: 10.1039/C7TC04804A.

[24] Reisfeld, R., Zigansky, E., & Gaft, M. (2004). Europium probe for estimation of site symmetry in glass films, glasses and crystals. *Molecular Physics*, 102(11-12), 1319-1330. doi: 10.1080/00268970410001728609.
[25] Schanda, J. (Ed.). (2007). *Colorimetry: Understanding the CIE system*. New Jersey: John Wiley & Sons.
[26] Silveira, W.S., Nascimento, P.A., Silva, A.J., & Rezende, M.V.D.S. (2020). Luminescent properties and energy transfer mechanism from Tb^{3+} to Eu^{3+} doped in $Y_3Al_5O_{12}$ phosphors. *Journal of Alloys and Compounds*, 822, article number 153651. doi: 10.1016/j.jallcom.2020.153651.
[27] Terebilenko, K.V., Bychkov, K.L., Klymyshyna, K.E., Baumer, V.N., Slobodyanik, M.S., Khomenko, E.V., & Dotsenko, V.P. (2017). Single crystals of $KRE(MoO_4)_2$, (RE-Ce, Pr) obtained from fluorides: scheelite-related structure and luminescence. *Crystal Research and Technology*, 52(12), article number 1700222. doi: 10.1002/crat.201700222.
[28] Urbina, L., Corcuera, M.Á., Gabilondo, N., Eceiza, A., & Retegi, A. (2021). A review of bacterial cellulose: sustainable production from agricultural waste and applications in various fields. *Cellulose*, 28(13), 8229-8253. doi: 10.1007/s10570-021-04020-4.
[29] Veleschuk, V., Vlasenko, A., Vlasenko, Z., Petrenko, I., Malyi, Y., Borshch, V., Borshch, O., & Shefer, A. (2019). Current-voltage characteristic and electroluminescence of UV LEDs 365 nm at liquid nitrogen temperature. *Optica Applicata*, 49(1), 125-133. doi: 10.5277/oa190111.
[30] Wang, Q., Sun, J., Yao, Q., Ji, C., Liu, J., & Zhu, Q. (2018). 3D printing with cellulose materials. *Cellulose*, 25, 4275-4301. doi: 10.1007/s10570-018-1888-y.
[31] Wang, P., Yin, Y., Fang, L., He, J., Wang, Y., Cai, H., Yang, Q., Shi, Z., & Xiong, C. (2023). Flexible cellulose/PVDF composite films with improved breakdown strength and energy density for dielectric capacitors. *Composites Part A: Applied Science and Manufacturing*, 164, article number 107325. doi: 10.1016/j.compositesa.2022.107325.
[32] Xie, F., Li, J., Dong, Z., Wen, D., Shi, J., Yan, J., & Wu, M. (2015). Energy transfer and luminescent properties of $Ca_8MgLu(PO_4)_7$: Tb^{3+}/Eu^{3+} as a green-to-red color tunable phosphor under NUV excitation. *RSC Advances*, 5(74), 59830-59836. doi: 10.1039/C5RA08680A.
[33] Zhao, D., Zhu, Y., Cheng, W., Chen, W., Wu, Y., & Yu, H. (2021). Cellulose-based flexible functional materials for emerging intelligent electronics. *Advanced materials*, 33(28), article number 2000619. doi: 10.1002/adma.202000619.
[34] Zhu, X., Jiang, G., Wang, G., Zhu, Y., Cheng, W., Zeng, S., Zhou, J., Xu, G., & Zhao, D. (2023). Cellulose-based functional gels and applications in flexible supercapacitors. *Resources Chemicals and Materials*, 2(2), 177-188. doi: 10.1016/j.recm.2023.03.004.
[35] Zhuravlov, O.Yu., Shyian, O.V., Shirokov, B.M., Kolodiy, I.V., & Sholohov, S.M. (2021). Sublimation process for obtaining silicon films from molybdenum and tungsten disilicide. *Scientific Herald of Uzhhorod University. Series "Physics"*, 49, 48-53.
[36] Zou, C., Qu, D., Jiang, H., Lu, D., Ma, X., Zhao, Z., & Xu, Y. (2019). Bacterial cellulose: A versatile chiral host for circularly polarized luminescence. *Molecules*, 24(6), article number 1008. doi: 10.3390/molecules24061008.
[37] Zuo, C., Zhou, Z., Zhu, L., Xiao, A., Chen, Y., Zhang, X., Zhuang, Y., Li, X., & Ge, Q. (2015). Luminescence properties of Tb^{3+}-doped borosilicate scintillating glass under UV excitation. *Spectrochimica Acta Part A: Molecular and Biomolecular Spectroscopy*, 147, 324-327. doi: 10.1016/j.saa.2015.03.097.

Володимир Васильович Бойко
Кандидат фізико-математичних наук, доцент
Національний університет біоресурсів і природокористування України
03041, вул. Героїв Оборони, 15, м. Київ, Україна
https://orcid.org/0000-0003-2926-2752
Віталій Петрович Чорній
Кандидат фізико-математичних наук
Національний університет біоресурсів і природокористування України
03041, вул. Героїв Оборони, 15, м. Київ, Україна
https://orcid.org/0000-0003-3727-5617
Сергій Герасимович Неділько
Доктор фізико-математичних наук, старший науковий співробітник
Київський національний університет імені Тараса Шевченка
01601, вул. Володимирська, 64/13, м. Київ, Україна
https://orcid.org/0000-0001-5196-6807
Катерина Володимирівна Теребіленко
Доктор хімічних наук, доцент
Київський національний університет імені Тараса Шевченка
01601, вул. Володимирська, 64/13, м. Київ, Україна
https://orcid.org/0000-0003-2403-4347

Люмінесцентні конвертери на основі композитних плівок «наноцелюлоза + $K_3Tb(PO_4)_2$:Eu»

Анотація. Перевагами целюлози та її похідних, як новітніх матеріалів для пристроїв, що виробляють, накопичують та перетворюють електроенергію є їх дешивизна, екологічність, легкість утилізації та можливість виготовлення різними способами і з різної сировини, в тому числі, і з відходів агропромисловості. Саме тому їх дослідження як матеріалів для сучасної техніки та електроніки є актуальним. Метою цієї роботи було з'ясування люмінесцентних характеристик композиційних плівок, виготовлених на основі наноцелюлози та полікристалічного оксиду $K_3Tb_{0,9}Eu_{0,1}(PO_4)_2$. Оптична мікроскопія та спектрально-люмінесцентний метод були застосовані для характеризації виготовлених плівок та їх вихідних компонент. З'ясовано, що кристаліти з середнім розміром близько 50 μм розподілені досить рівномірно у плівці «наноцелюлоза+$K_3Tb_{0,9}Eu_{0,1}(PO_4)_2$». Для досліджених зразків у формі суспензій спостерігалась смуга Раманівського розсіяння світла з максимумом на 564 нм при лазерному збудженні на 473 нм. Інтенсивність фотолюмінесценції наноцелюлози у вигляді суспензії та в плівках є низькою в порівнянні зі свіченням оксиду як наповнювача. Свічення іонів Eu^{3+} є інтенсивним в червоній області спектра. Обчислені значення ступеня асиметричності вказують на низьку симетрію позицій, які займають іони європію в оксиді та на внесок випромінювання іонів Tb^{3+} в загальний спектр композитної плівки. За результатами досліджень з'ясовано, що люмінесценцію іонів Eu^{3+} сенсибілізовано іонами Tb^{3+}, які поглинають збуджуюче світло з подальшою передачею енергії до іонів європію. Положення смуг поглинання іонів Eu^{3+} та Tb^{3+} в ультрафіолетовій ділянці спектра та інтенсивне випромінювання Eu^{3+} в червоній області вказують на перспективність використання плівок «наноцелюлоза+ $K_3Tb_{0,9}Eu_{0,1}(PO_4)_2$» для підвищення ефективності сонячних панелей. Тестування плівок при збудженні люмінесценції ультрафіолетовим випромінюванням світлодіоду ($\lambda_{зб}$ = 375 нм) показало можливість розробки на їх основі білих світлодіодів. Зокрема, координати колірності світлодіода без покриття становили (x = 0,214; y = 0,079), а використання плівки – композиту, як покриття, призводить до зміщення координат до червоної області: x = 0,304, y = 0,196. Одержані результати щодо морфології та люмінесцентних властивостей можуть бути використані для оптимізації складу та умов виготовлення композитних плівок типу «наноцелюлоза+$K_3Tb_{0,9}Eu_{0,1}(PO_4)_2$» для їх застосування як люмінесцентних конвертерів у світлодіодах або сонячних панелях

Ключові слова: іон; сенсибілізація; світлодіод; сонячна панель; фотолюмінесценція; покриття

ТЕХНІКА ТА ЕНЕРГЕТИКА

Науковий журнал

Том 14, № 2. 2023

Заснований у 2010 р. Виходить чотири рази на рік

Оригінал-макет видання виготовлено у відділі науково-технічної інформації
Національного університету біоресурсів і природокористування України

Відповідальний редактор:
Г. Івченко

Редагування англомовних текстів:
С. Воровський, К. Касьянов

Комп'ютерна верстка:
О. Глінченко

Підписано до друку 26 квітня 2023 р. Формат 60*84/8
Умов. друк. арк. 10,6
Наклад 50 прим.

Адреса видавництва:
Національний університет біоресурсів і природокористування України
03041, вул. Героїв Оборони, 15, м. Київ, Україна
E-mail: info@technicalscience.com.ua
www: https://technicalscience.com.ua/uk

MACHINERY & ENERGETICS

Scientific Journal

Volume 14, No. 2. 2023

Founded in 2010. Published four times per year

The original layout of the publication is made in the Department of Scientific and Technical Information of National University of Life and Environmental Sciences of Ukraine

Managing editor:
H. Ivchenko

Editing English-language texts:
S. Vorovsky, K. Kasianov

Desktop publishing:
O. Glinchenko

Signed for print of April 26, 2023. Format 60*84/8
Conventional printed pages 10.6
Circulation 50 copies

Editors Office Address:
National University of Life and Environmental Sciences of Ukraine
03041, 15 Heroiv Oborony, Kyiv, Ukraine
E-mail: info@technicalscience.com.ua
www: https://technicalscience.com.ua/en